

Current flow in $\text{YBa}_2\text{Cu}_3\text{O}_{7-x}$ Deformation Textured Coated Conductors

by

D. Matthew Feldmann

A dissertation submitted in partial fulfillment
of the requirements for the degree of

Doctor of Philosophy
(Physics)

at the
University of Wisconsin – Madison

2001

Acknowledgements

I am indebted to a large number of people, both at the UW and elsewhere, who helped make this work possible. First I would like to thank my advisor, David C. Larbalestier, for his encouragement, for the many opportunities he granted me, and especially for providing me with an environment in which I could excel. George Daniels, who has been a good friend and constant sounding board, trained me on most of the equipment I used to complete this work. George also “corrected” many of my sample handling practices, though I will still go into my drybox without gloves. Anatolii Polyanskii did an excellent job of training me in the art of magneto-optical imaging, a technique relied upon very heavily in this thesis. Xeu Yu Cai introduced me to the laser cutter and taught me how to use chopsticks. Nina Heinig taught me to use the scanning electron microscope and showed me how to make photolithographic masks. Alex Squiteri assisted me with transport measurements. Jodi Reeves, Bill Starch, Professor Susan Babcock, Professor Grace Wahba, and Professor Eric Hellstrom are also thanked for their assistance.

None of the work in this thesis would have been possible without external collaborations. I would like to thank Tim Peterson, Paul Barnes, Charles Oberly, and everyone at Air Force Research Laboratories (AFRL). The results of our initial collaboration with AFRL laid the foundation for the rest of this thesis work. Ron Feenstra, at Oak Ridge National Laboratory (ORNL), provided me with many great discussions and a very generous supply of samples. Samples from ron appear in each of Chapters Two, Three and Four. Darren Verebelyi [first at ORNL and then at American

Superconductor (AMSC)] provided me with great discussions, pogo pins, and a very generous supply of samples while at AMSC. Without the samples from Darren, Chapter Four wouldn't exist.

Table of Contents

1. Introduction	1
1.1 Why $\text{YBa}_2\text{Cu}_3\text{O}_{7-x}$ deformation textured coated conductors?	2
1.2 The $\text{YBa}_2\text{Cu}_3\text{O}_{7-x}$ deformation textured coated conductor	5
1.3 Significance of grain boundaries in $\text{YBa}_2\text{Cu}_3\text{O}_{7-x}$	8
1.4 Motivation and structure of this thesis	10
2. Influence of substrate grain structure on YBCO connectivity	13
2.1 Magneto-optical imaging evidence	13
2.2 The source of the granularity	19
2.3 Texture development	43
2.4 Summary	32
3. Visualization of the self-field of deformation textured coated conductors	34
3.1 Comparing and contrasting magnetization and transport MO imaging	34
3.2 Experimental	38
3.3 Results and Discussion	40
3.3.1 <i>Magneto-optical imaging of transport current in F159CN2</i>	40
3.3.2 <i>Transport currents in F197CN1</i>	48
3.3.3 <i>Transport currents in TFA1455</i>	61
3.4 Conclusions	66
4. Inter and intra-grain transport measurements	69
4.1 Experimental	69
4.2 Results and discussion	74

4.3 Summary and conclusions	86
5. Summary	87
5.1 Summary of results	87
5.2 Implications for the technology and conclusions	89
A. Magneto-optical imaging	91
A.1 The indicator film	91
A.2 Equipment and imaging geometry	94
A.3 Imaging modes	96
A.4 Interpretation of magneto-optical images	97
B. Orientation mapping	101
B.1 Electron back-scatter diffraction equipment	101
B.2 Orientation mapping	102
C. Current Reconstruction.....	106
C.1 Introduction	106
C.2 Resolution of the magnetic inverse problem	108
References	113

1

Introduction

The discovery of high-temperature superconducting (HTS) materials in the late 1980s [1-3] generated visions of a countryside littered with high capacity power lines and magnetically levitated trains. Today, more than 10 years later, there are no magnetically levitated trains using HTS materials and, while the first HTS power line went into operation in June of this year [4], it is only slightly greater than a football field in length. This is not to paint a picture of gloom for HTS materials, but rather to impress that the road to commercial applications and production has been arduous. The driving forces, however, remain strong. Many potential applications for HTS materials exist across many different industries, including magnetically levitated trains, Magnetic Resonance Imaging (MRI) devices, power transformers, and transmission lines. Some of these applications exist today using low-temperature superconducting (LTS) materials. However, LTS materials require expensive liquid helium (LHe) as a cryogen, and applications using LTS materials could enjoy decreased operating costs and increased efficiency with HTS materials. Other applications (e.g. fault current limiters) simply aren't practical without HTS materials.

This chapter will discuss the motivation behind the efforts to produce a $\text{YBa}_2\text{Cu}_3\text{O}_{7-x}$ coated conductor form, the standard construction of the deformation textured coated conductor, the consequence of grain boundaries in $\text{YBa}_2\text{Cu}_3\text{O}_{7-x}$, and the layout of this thesis.

1.1 Why $\text{YBa}_2\text{Cu}_3\text{O}_{7-x}$ deformation textured Coated Conductors?

Table 1.1 lists properties of several of the high-temperature superconductors. For commercial applications, it is desirable to have good magnetic field properties and a high critical current density (J_c) at the temperature of liquid nitrogen, 77 K. $\text{YBa}_2\text{Cu}_3\text{O}_7$ (YBCO) has among the highest J_c values and the best performance in a magnetic field. The Bi-Sr-Ca-Cu-O (BSCCO) compounds have relatively low J_c values and poor field performance, and while some of the thallium and mercury compounds have J_c values that can compete with YBCO, their in-field performance is not as good. However, commercial applications also require that the material be manufactured in long lengths (>1 km), and that those long lengths retain much of the quality of laboratory length samples. This requirement has been one of the greatest obstacles to HTS commercial products.

All of the HTS materials are inevitably polycrystalline in long lengths, and the effects of this polycrystalline nature on electromagnetic properties must be considered. YBCO exhibits reduced electromagnetic coupling across grain boundaries (GBs), detrimentally affecting both J_c and field performance [7,21-22]. Some work has been done on the thallium compounds suggesting that low angle GBs may not be a problem in this system, but these studies suffer from low intra-grain J_c values [23,24]. A systematic study of GBs in the mercury compounds has not yet been done, but magneto-optical (MO) imaging has shown granular behavior not unlike YBCO [25]. Grain boundaries in

BSCCO appear to have a weaker influence on superconducting properties, and the BSCCO compounds have been successfully made in long lengths with useful J_c values at 77 K. This is despite the fact that the typical J_c of BSCCO tapes is roughly two orders of magnitude less than YBCO (see Table 1.1), which is a testament to the detrimental nature of granularity in YBCO. While long lengths of BSCCO can be manufactured, its superconducting properties make it unsuitable for high J_c and high field applications at 77 K. For such applications the properties of YBCO are very attractive and the production of high-quality YBCO wires is the focus of much research.

High-Temperature Superconductors

Material	T_c (K)	J_c (A cm ⁻²)	H^* (T)	Comments	Reference
YBa ₂ Cu ₃ O ₇	92	2-5 × 10 ⁶	5-9	thin films	Daniels, 2000 [5]
	-	4.5 × 10 ⁶	9	thin films	Verebelyi, 2000 [6]
Bi ₂ Sr ₂ CaCu ₂ O ₈	85	40 × 10 ³	-	thin film - electrolytic deposition	Villard, 2000 [7]
	92	25 × 10 ³	-	PAIR processed tape	Miao, 1998 [8]
Bi ₂ Sr ₂ Ca ₂ Cu ₃ O ₁₀	89	-	0.2	bulk single crystal	Pradhan, 1994 [9]
	-	12-63 × 10 ³	0.16-0.34	compilation of various tapes from different sources	Schwartzkopf, 1999 [10]
	-	180 × 10 ³	-	local value from current reconstruction	Feldmann, 2001 [11]
HgBa ₂ Ca ₂ Cu ₃ O ₁₀	130	3.5 × 10 ⁶	-	thin film	Yun, 1996 [12]
	132	< 10 ⁴	< 5	polycrystalline bulk sample	Fujinami, 1998 [13]
HgBa ₂ CaCu ₂ O ₈	124	3.2 × 10 ⁶	~ 0.6	thin film	Yan, 1998 [14]
	102	-	1.2	polycrystalline bulk sample - Ca doped	Akao, 2000 [15]
	110	< 10 ⁶	-	thin film	Yu, 1997 [16]
	124	2.2 × 10 ⁶	~2.4	thin film on RABiTS™	Xie, 2000 [17]
Tl ₂ Ba ₂ CaCu ₂ O ₁₀	99-102	4-15 × 10 ⁵	-	laser ablation and annealing	Cardona, 1993 [18]

$Tl_2Ba_2Ca_2Cu_3O_{10}$	> 110	> 10^6	-	thin film	Juang, 1995 [19]
$TlBa_2CaCu_2O_7$	90-93	2×10^4	< 0.8	thin film	Gapud, 1999 [20]

Table 1.1. Properties of selected HTS materials compiled from various sources. All H^* values are at 77 K, and all J_c values are at 77 K and 0 T. H^* , the irreversibility field, is the field above which J_c is zero. For comparison, conventional copper cables are operated at 100-400 A cm⁻².

In order to manufacture YBCO in long lengths with useful J_c values it is necessary to minimize the number of high angle GBs in the conductor. This has been done most successfully by growing YBCO films on oxide-buffered metal tapes, a conductor form referred to as a coated conductor (CC). The number of high angle GBs in the YBCO is reduced through bi-axial alignment of either the buffer layers or the substrate. Bi-axial alignment means that the *a*-axes and *c*-axes of the YBCO grains are aligned near a common reference axis, in this case the rolling and normal directions of the tape respectively. There are several methods to induce bi-axial texture, but the two most successful are Ion Beam Assisted Deposition (IBAD) [26,27] and deformation texturing [28]. In the IBAD technique, the texture is introduced in the buffer layer, generally yttria-stabilized zirconia (YSZ). The deposition of the YSZ layer occurs under an ion beam assist, giving rise to bi-axial texture. While this process allows for the use of strong, non-magnetic substrates, and can result in a very high degree of texture, it is extremely slow and not considered practical for commercial applications at present. The use of MgO instead of YSZ in IBAD tapes has proven to be a much faster process and there have been some encouraging results [29]. However, the degree of texture of texture attainable with IBAD MgO tapes is limited [30]. In deformation texturing, texture is introduced into the metal substrate, generally pure Ni, by mechanical deformation and re-

crystallization. This can be done in long lengths much more readily, but the degree of texturing is not as good as can be obtained with IBAD [31]. Also, the scale of the granularity is larger with deformation texturing (50-100 μm versus 1-5 μm), and modeling has shown that there is a positive correlation between increased critical current density (J_c) and decreased grain size (at a fixed tape width) [32]. Despite this, deformation textured CCs can produce J_c values exceeding 2×10^6 A/cm² in short lengths, and are considered by many to be the most promising means of creating a YBCO commercial product.

1.2 The $\text{YBa}_2\text{Cu}_3\text{O}_{7-x}$ deformation textured coated conductor

The deformation textured coated conductor consists of a metal substrate, generally pure Ni, on top of which buffer layers and YBCO are deposited. The buffer layer structure is part seed, part diffusion barrier, and part cap layer suitable for YBCO growth. Variations exist in the buffer layer materials, the number of buffer layers, and the deposition methods for the buffer layers and the YBCO, but the general architecture is similar from one sample to the next.

The substrate provides the textured template for subsequent oxide film growth. Nickel is often chosen as a substrate material because of its lattice parameter match with YBCO, and because it oxidizes less readily than other metal compounds at the temperatures required for buffer layer and YBCO deposition. Ni is weak and magnetic and alloys exist with more desirable properties, but these alloys generally produce poorer

quality films. Recently, there have been some promising results with a weakly magnetic Ni-W alloy [33]. The substrates are inherently polycrystalline regardless of the alloy used, but deformation texturing can result in a high degree of bi-axial alignment [34]. This is diagrammed in Figure 1.1. In a well-textured Ni tape, most grain to grain misorientation angles will be less than 10° , with out of plane (*c-axis*) alignment superior to in-plane (*ab-axis*) alignment. The average grain size of the Ni will be roughly equal to the thickness of the Ni (usually 50-100 μm).

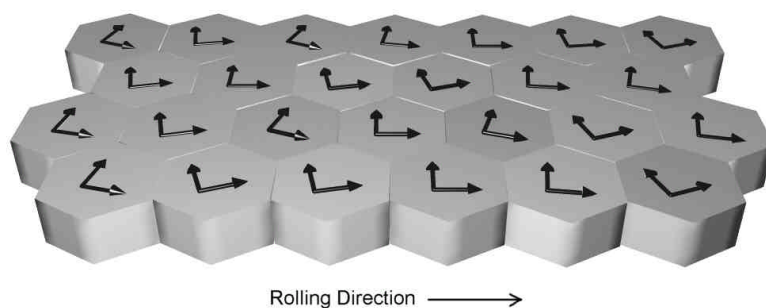


Figure 1.1. Schematic of the orientation of Ni grains in a deformation textured Ni substrate. The Ni grains are approximated as a hexagonal lattice. The black arrows in each grain represent the directions of the *a* and *b*-axes. The *c*-axis orientation of each grain is omitted for clarity, but is generally within a few degrees of normal.

Buffer layer structures can vary, but a very common architecture is shown in Figure 1.2. On top of the Ni a seed layer of CeO_2 or Y_2O_3 is grown. During growth of the seed layer, care must be taken to avoid the formation of nickel oxide. Often growth of the seed layer starts in a reducing environment. Next, a layer of yttrium stabilized zirconia (YSZ) acts as a diffusion barrier to prevent nickel from reaching the YBCO.

YSZ is ZrO_2 with 8-15 mol% Y_2O_3 . The lattice parameter match between YSZ and YBCO is poor [35], requiring a cap layer of CeO_2 to provide a suitable template for YBCO growth. Deposition methods for the buffer layers vary but include electron-beam evaporation, sputtering, pulsed laser deposition (PLD), and solution based methods [36].

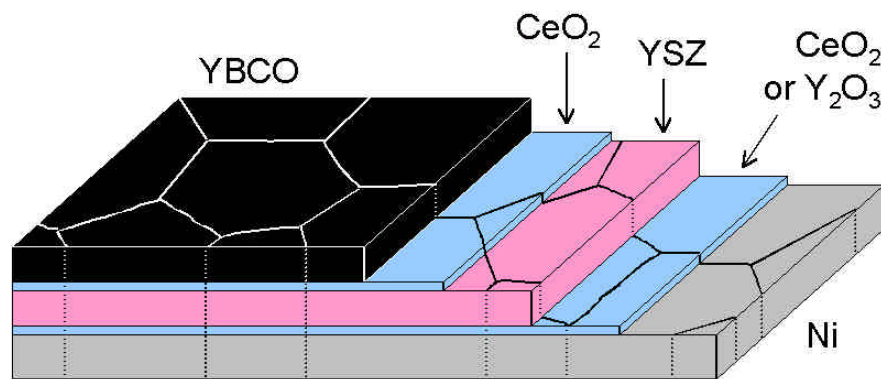


Figure 1.2. The layered structure of a typical coated conductor. Thickness of the layers are: Ni, 50-100 μm ; seed layer, 100-200 \AA ; YSZ, 300-500 nm; cap layer, 100-200 \AA ; YBCO, > 100 nm.

Common deposition methods for the YBCO layer are PLD [37], the BaF_2 [38] method, or the trifluoroacetate (TFA) [39] method. The thickness of the YBCO may vary from 100 nm to several microns, but the YBCO layer of nearly all the samples in this thesis was 300-400 nm thick. The final size of most laboratory grown samples is 3-5 mm wide, 50-100 μm thick, and 1-2 cm long.

1.3 Significance of grain boundaries in $\text{YBa}_2\text{Cu}_3\text{O}_{7-x}$

It is well known that GBs in YBCO can exhibit greatly reduced J_c and field performance. Much of our knowledge of GBs in YBCO comes from studies of thin film ($< 1 \mu\text{m}$) [001] tilt GBs [5,6,21,22]. While these studies may not agree quantitatively, they do agree on the qualitative form of the $J_c(\mathbf{q})$ dependence. Out to a given critical angle \mathbf{q}_c , the J_c of a GB is not reduced with respect to the intra-grain. Beyond \mathbf{q}_c the J_c of a GB decreases exponentially with increasing \mathbf{q} . The magnitude of \mathbf{q}_c varies from 2-7° depending on the study, but recent studies [5,6] based on an intra-grain critical current density (J_c) of $\sim 4.0 \text{ MA/cm}^2$ have found \mathbf{q}_c to be 2-3° reproducibly. Figure 1.3 plots J_c versus \mathbf{q} for YBCO thin films grown by pulsed laser deposition (PLD) on [001] tilt SrTiO (STO) substrates. Here, \mathbf{q}_c is 2-3° followed by a steep exponential fall off. At 3°, a GB may already have a J_c less than half that of the intra-grain, and by 5° J_c has fallen to $\sim 20\%$ of intra-grain values. 10° is generally considered the upper limit of ‘low angle’ grain boundaries (LAGBs) and typical J_c values are $\sim 0.1 \text{ MA/cm}^2$. It will be shown in later Chapters that even the best CC samples have plenty of GBs greater than 5°, and as the plot of Figure 1.3 suggests, obtaining single-crystal-like J_c values on a polycrystalline substrate is certainly challenging.

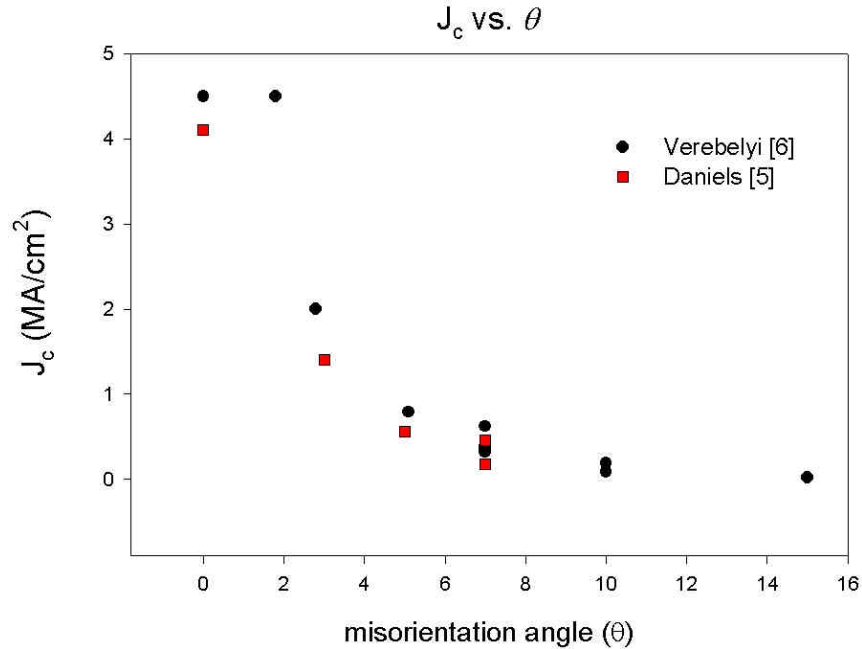


Figure 1.3. Critical current density versus misorientation angle for [001] tilt YBCO (PLD) bicrystals. A misorientation angle of 0° refers to an intra-grain value. Thanks to G. Daniels at the University of Wisconsin - Madison and Ron Feenstra at Oak Ridge National Laboratory (ORNL) for providing data.

The voltage-current (V-I) and $J_c(H)$ behavior of typical intra and inter-grain links are shown Figures 1.4. The plot of Figure 1.4(a) shows intra-grain V-I traces, which are rather straight and evenly spaced on a log-log scale. Figure 1.4(b) plots corresponding data for a 7° GB. Below H^* , there is a steeper rise to the V-I traces, and a ‘knee’ at higher voltages, though less pronounced in the zero field trace. The in-field traces below H^* are clustered together, and above H^* the dissipation of the intra-grain dominates. The clustering and ‘knee’ features are misorientation angle dependent, and there is a smooth transition between the V-I behavior of Figure 1.4(b) and (a) as the GB angle decreases.

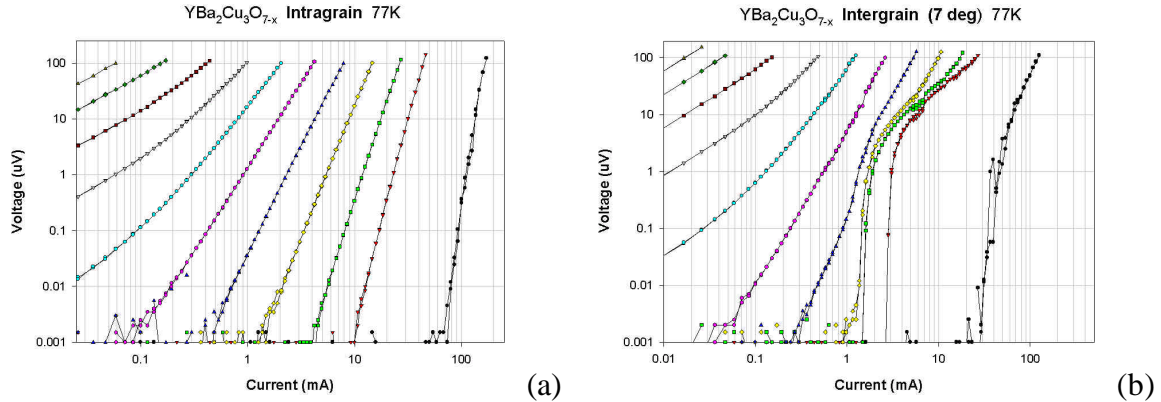


Figure 1.4. V-I plots of inter and intra-grain links showing typical in-field behavior. These traces were taken from YBCO grown on a 7° [001] tilt STO bicrystal substrate. The traces of both plots are from 0 to 10 T in increments of 1 T. Data provided by G. Daniels [5]. (a). V-I traces of an intra-grain link. Intra-grain traces are generally rather straight on a log-log plot. (b) V-I traces of a 7° GB. Typical GB V-I behavior in lower fields (<5 T) includes a steeper rise of the V-I traces and a ‘knee’ at higher voltages. At and above H^* (~ 5 T here), the intra-grain behavior dominates.

This is but a short introduction to LAGB behavior, and does not cover various micro-structural or theoretical aspects of GBs [40,41]. Such investigations are beyond the scope of this discussion, as it is not the purpose of this thesis to provide a detailed understanding of individual GB properties. The $J_c(\mathbf{q})$ dependence of GBs and the typical inter and intra-grain V-I behavior presented here is meant to aid in the interpretation and understanding of data presented in the following Chapters. In deformation textured CCs, the YBCO above each substrate grain is its own intra-grain region and each intra-grain region is surrounded by GBs. In considering magneto-optical (MO) images or V-I measurements taken over hundreds or thousands of such grains, it may be helpful to refer to the properties of low angle GBs mentioned here.

1.4 Motivation and structure of this thesis

Previous to this work the granular nature of the CC was not appreciated, and the idea that current percolated through CCs was generally not accepted. Most characterizations of these conductors had consisted of x-ray or transport measurements over thousands of substrate grains, and what was going on at the grain-to-grain level was not understood. These types of characterizations promoted a single-crystal-like view of deformation textured CCs, when the reality was quite different. Bicrystal studies [5,6] have shown the detrimental effect GBs have on J_c and in-field properties of YBCO, but the nature and impact of GBs in CCs was unknown. These issues motivated an investigation on a smaller scale, commensurate with the substrate grain size. The purpose of this thesis is to provide a detailed understanding of the current flow in deformation textured CCs from the micro to the macro scale, with the hope that such knowledge will aid in the improvement of the technology.

The work in this thesis is presented roughly in the order that it was performed. In this way the historical and logical progression of the work is conveyed, from the identification of the granular nature of YBCO on deformation textured substrates to more detailed analyses. Chapter two provides the first direct evidence of the granularity of CCs and the percolative nature of current flow. Chapter three studies the behavior of transport currents in the conductor, and Chapter four quantifies individual inter and intra-granular regions. Chapter five summarizes the work and discusses the implications for the technology.

Two techniques used heavily in this thesis are magneto-optical (MO) imaging and orientation mapping [a.k.a. electron back-scatter diffraction (EBSD), electron back-scatter Kikuchi pattern (EBKP) analysis, Orientation Imaging Mapping (OIMTM), and likely a few others]. MO imaging is a method of visualization of magnetic fields, and is discussed in Appendix A. Orientation mapping is a method of mapping grain orientations by analyzing a series of Kikuchi patterns, and is discussed in Appendix B. The unfamiliar reader may wish to read the appendices before proceeding.

2

Influence of substrate grain structure on YBCO connectivity

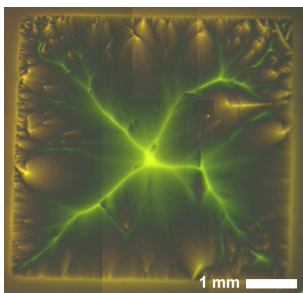
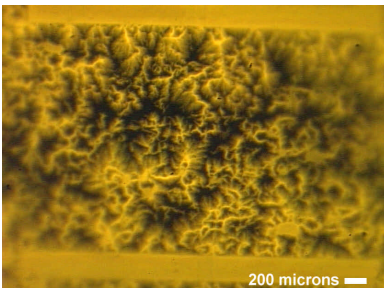
Before the present work, it was generally believed that the substrate grain structure in deformation textured CCs did not have a significant impact on the current flow in the overlying YBCO. It was thought that the buffer layers were providing a defense against the influence of substrate GBs and the idea that current percolated through the YBCO was not accepted. Some of the first evidence to the contrary was obtained by magneto-optical (MO) imaging (see Appendix A). The MO images themselves did not convert many, but MO imaging combined with light microscopy (LM) proved conclusively that the GBs in the substrate were propagating through the buffer layers to the YBCO.

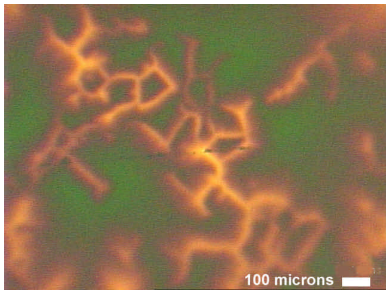
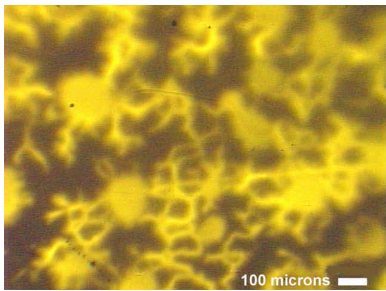
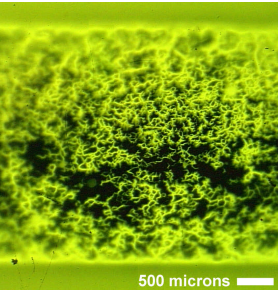
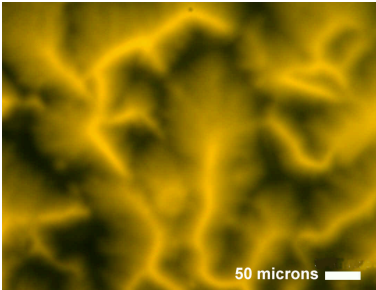
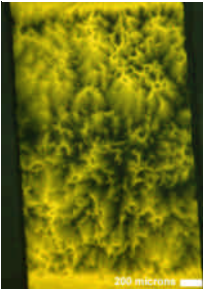
2.1 Magneto-optical imaging evidence

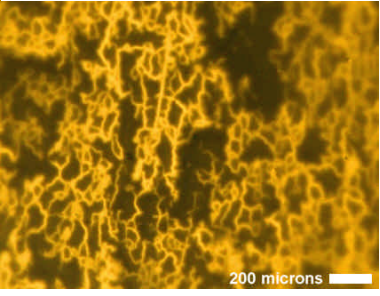
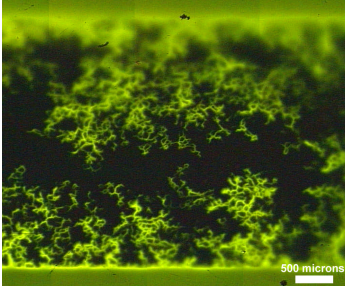
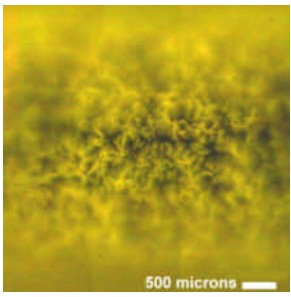
The first evidence that current flow in deformation textured CCs was percolative came from MO imaging. MO images of CCs from several sources showed a granular

flux pattern quite unlike that of single crystals. A selection of MO images demonstrating this granular flux pattern is given in Table 2.1. The images span various magnifications, so the effect of the granularity can be seen on several length scales. At higher magnifications, such as the third and sixth images in Table 2.1, the scale of the granularity is seen to be 50-100 μm , immediately suggestive of the underlying Ni grains. In contrast, the YBCO grain size is sub-micron. The first entry in the table, a MO image of YBCO grown on a single crystal substrate, is included for comparison to the CC images. Aside from the influence of a few chips and scratches at the edges, current flow is uniform and a characteristic ‘rooftop’ pattern can be seen. There is no granularity visible on any scale.

Examples of granular flux penetration in deformation textured coated conductors

Magneto-optical image	Image details	Sample details
	FC^\dagger $H_a = 60 \text{ mT}$ $T = 15 \text{ K}$	Y904Ya University of Wisconsin YSZ/YBCO YBCO: PLD $J_c = 2.0 \text{ MA cm}^{-2}$ (Single crystal substrate)
	ZFC^\ddagger $H_a = 60 \text{ mT}$ $T = 12 \text{ K}$	TFA0726 American Superconductor Corporation Ni/CeO ₂ /YSZ/CeO ₂ /YBCO YBCO: trifluoroacetate method $J_c \text{ N/A}$

	<p>FC[‡] $H_a = 60$ mT $T = 50$ K</p>	<p>34.1390 Air Force Research Laboratory Ni/CeO₂/YSZ/CeO₂/YBCO YBCO: PLD J_c N/A</p>
	<p>FC[‡] $H_a = 60$ mT $T = 8$ K</p>	<p>36.1397 Air Force Research Laboratory Ni/CeO₂/YSZ/CeO₂/YBCO YBCO: PLD J_c N/A</p>
	<p>ZFC[‡] $H_a = 80$ mT $T = 9$ K</p>	<p>B Oak Ridge National Laboratory Ni/CeO₂/YSZ/CeO₂/YBCO YBCO: BaF₂ Method $J_c(77$ K, 0 T) = 0.8 MA cm⁻²</p>
	<p>ZFC[‡] $H_a = 60$ mT $T = 77$ K</p>	<p>TFA1461 American Superconductor Corporation Ni/CeO₂/YSZ/CeO₂/YBCO YBCO: trifluoroacetate method $J_c(77$ K, 0 T) = 0.9 MA cm⁻²</p>
	<p>ZFC[‡] $H_a = ??$ mT $T = 77$ K</p>	<p>TFA1462 American Superconductor Corporation Ni/CeO₂/YSZ/CeO₂/YBCO YBCO: trifluoroacetate method $J_c(77$ K, 0 T) = 0.8 MA cm⁻²</p>

	ZFC [‡] $H_a = ??$ mT $T = ??$ K	CMDM2 Oak Ridge National Laboratory Eu ₂ O ₃ buffer layer YBCO: PLD $J_c(77$ K, 0 T) = ?? MA cm ⁻² Buffer layers were chemically deposited
	ZFC [‡] $H_a = 40$ mT $T = 9$ K	A Oak Ridge National Laboratory Ni/CeO ₂ /YSZ/CeO ₂ /YBCO YBCO: BaF ₂ Method $J_c(77$ K, 0 T) = 0.8 MA cm ⁻²
	ZFC [‡] $H_a = 80$ mT $T = 77$ K	F159CN2 Oak Ridge National Laboratory Ni/Y ₂ O ₃ /YSZ/CeO ₂ /YBCO YBCO: BaF ₂ Method $J_c(77$ K, 0 T) = 2.3 MA cm ⁻²

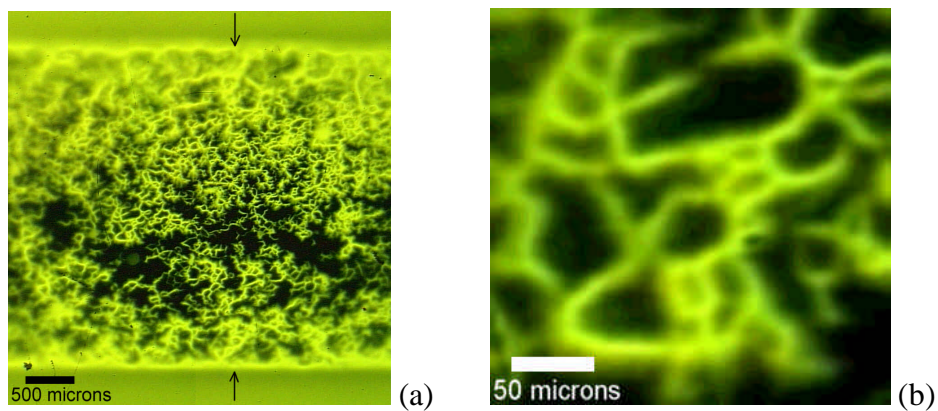
[†] Field cooled (FC). Sample was cooled from above T_c in an applied field of H_a and then the field was removed.

[‡] Zero field cooled (ZFC). Sample was cooled in the absence of a field, and then a field (H_a) was applied.

Table 2.1. Examples of granular flux penetration in deformation textured CCs. The first image is of a single crystal for comparison. All exhibit qualitatively similar magnetic granularity on the scale of the underlying Ni grains, ~50-100 μ m.

Figure 2.1 takes a closer look at the granularity of one of the CC samples. Figure 2.1(a) is the 5th entry in Table 2.1. The MO image is taken over the entire width of the sample, ~3.3 mm. For this image, the sample was cooled in the absence of a field to 9 K, and then a field of 80 mT was applied. The granular structure can be seen throughout the sample, and is shown at higher magnification in Figure 2.1(b). This magnetic granularity is the result of many small current loops. Some current loops are as small as 50 μ m in size, and exist in regions completely surrounded by flux penetration. Figure

2.1(c) is a profile of the magnetic flux taken across Figure 2.1(a) at the location of the arrows. The profile shows that the magnetic field is greatest at the sample edges, and decreases toward the center. The overall “V” shape of the profile is due to macroscopic currents circulating over the whole sample. If macroscopic currents were not flowing, then there would be no global flux gradient across the sample. This observation provides us with a very important piece of information - the bright features in the MO images are carrying current. The smaller oscillations in the flux profile of Figure 2.1(c) are due to local magnetic granularity associated with the smaller current loops. Therefore, the overall magnetic field distribution seen in Figure 2.1(a) is the result of macroscopic currents flowing over the whole sample, convoluted with smaller, local current loops. The net result is that currents are percolate through the sample and are spatially very non-uniform.



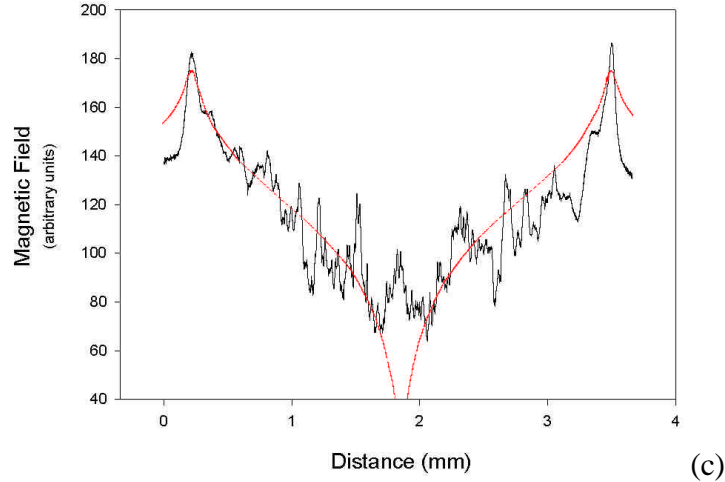


Figure 2.1. MO images and flux profile of a CC. (a) MO image of a CC. For this image the sample was zero field cooled to 9K, and then a field of 80 mT was applied. (b) A close-up view of the granularity seen in (a). (c) A flux profile across the image in (a) at the location of the arrows. The profile is a result of macroscopic currents convoluted with local smaller current loops. The red profile is the theoretical profile produced by a uniform single-crystal.

The examples of granular flux penetration shown in Table 2.1 are a small subset of all the CC samples that have been imaged throughout this thesis work. More than three dozen deformation textured CCs exhibited qualitatively similar electromagnetic granularity, despite significant variations in construction. These variations include substrates from three different sources and varying buffer layer combinations, including CeO_2 , yttria-stabilized zirconia (YSZ), Y_2O_3 [42] and Eu_2O_3 [36], deposited by e-beam, sputtering, PLD, and sol-gel [34] techniques. YBCO deposition methods include PLD, BaF_2 [38] and trifluoroacetate (TFA) [39]. Critical current densities, when available, ranged from 0.1 to 2.4 MA/cm^2 . The one factor all these samples had in common was a deformation textured Ni substrate.

In considering the reason for the granularity of the MO images, the obvious culprit is the polycrystalline substrate. The average grain size of the substrate is

approximately the same as the scale of the magnetic granularity, 50-100 μm . If the substrate were producing a network of GBs in the YBCO, this could account for the observations made in Figure 2.1. GBs can carry a non-zero super current, allowing for macroscopic current flow. From Figure 1.3, the intra-grain regions (above single substrate grains) have J_c values greater than most GBs, forcing some current to flow in smaller loops and giving rise to magnetic granularity. A network of GBs in the YBCO would explain the MO images in Table 2.1 and the flux profile of Figure 2.1(c).

2.2 The source of the granularity

With such similar magnetic granularity across many deformation textured CCs with different buffer layer materials and deposition methods it is easy to suspect the substrate grain structure as the source of the granularity, but the MO images themselves do not constitute proof of this. In order to demonstrate conclusively the influence of the substrate GBs, it is necessary to obtain a one-to-one correlation with the MO images. This was done by first investigating the YBCO layer, and then removing the buffer layers to expose the directly underlying substrate.

Magneto-optical imaging, light microscopy (LM) and scanning electron microscopy (SEM) was performed on a CC sample from Air Force Research Laboratory. This substrate was well textured with in and out of plane full-width half maxima of 6.6° and 5.8° , respectively, as measured by x-ray pole figures. The YBCO and all buffer layers were deposited by PLD, with architecture Ni/CeO₂/YSZ/CeO₂/YBCO and

thickness of 100/500/100/600 nm for the respective oxide layers. The substrate thickness was ~ 100 μm , as was the average grain size. The LM was done using a NIKON polarizing light microscope with a yellow-green light source (giving rise to the green hue in some of the images) and MO imaging was performed as described in Appendix A. After MO imaging the YBCO layer was removed with a weak (0.05%) nitric acid etch, and then the buffer layers were removed with a 2:3 solution of NH_4F (40%) and HF (48%).

A portion of the granular flux network of this sample is shown in Figure 2.2(a). The J_c of the sample was not measured, but a similarly processed sample had a J_c value of 1.2 MA/cm^2 . Light microscopy of the surface of the YBCO [Fig. 2.2(b)] shows a grain structure that correlates well with the MO image. Some, but not all, of the GBs of Fig. 2.2(b) can be immediately matched up to the flux-penetration network of Fig. 2.2(a). A light micrograph of the Ni surface is presented in Fig. 2.2(c). The chemical etch roughened the surface of the Ni, but the location of the GBs was unchanged. Figure 2.2(d) overlays the MO and Ni images making it clear that flux penetration in the YBCO does occur preferentially along Ni GBs, but that not all Ni GBs provoke flux entry. The montage of Fig. 2 shows conclusively that the underlying Ni grain structure is producing a network of GBs in the YBCO layer.

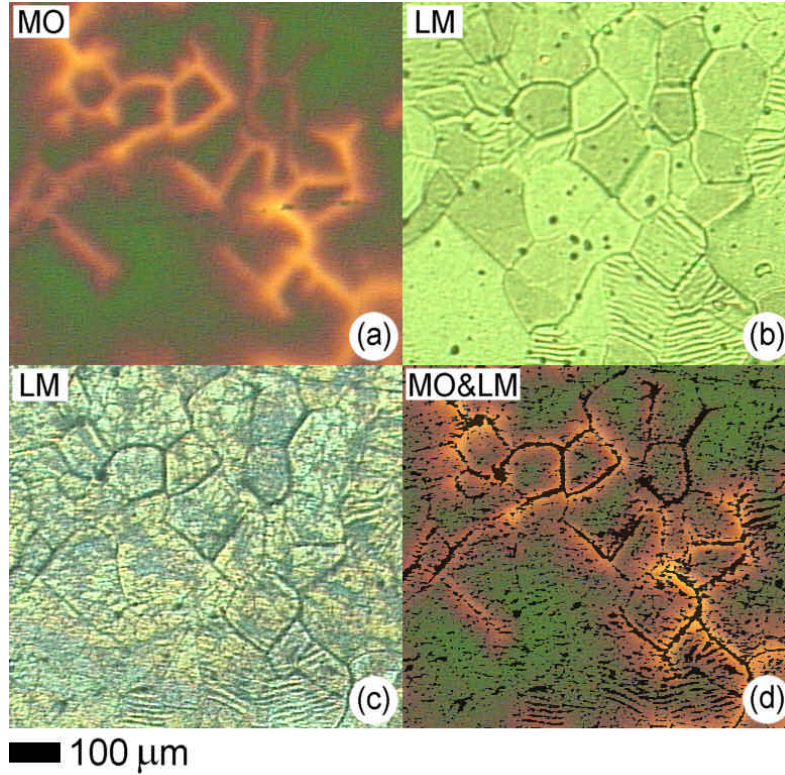


Figure 2.2. MO and light microscopy images of the same location, demonstrating the influence of the grain boundaries in the Ni substrate on the flux penetration pattern and on the visible YBCO GB structure. (a) MO image. The sample was cooled in a field of 60 mT from above T_c to 50K, and then the field was removed. Darker (green) areas are electromagnetically well connected regions, while the lighter (orange) flux network indicates where the local current density is reduced. (b) Light micrograph of the surface of the YBCO, showing a visible GB structure similar to the MO image. (c) Light micrograph of the underling Ni substrate after removal of the buffer layers. (d) Overlay of (a) and (c) showing that flux penetration occurs almost exclusively over along Ni GBs and also that not all Ni GBs admit flux.

One question Figure 2.2 raises is, why are some GBs appearing in the MO image while others are not? An earlier study of flux penetration in YBCO grown on of [001] tilt STO bicrystals [43] has shown that GBs become visible in MO images when the intergranular critical current density (J_{cb}) is smaller than the intra-granular critical current density (J_{cg}). Stated differently, GBs are visible in MO images when J_{cb}/J_{cg} is less than unity. Figure 2.3 shows MO images of a 3° , 5° , and 7° GB illustrating this point. This study also found that the flux penetration at a GB *increases* as J_{cb}/J_{cg} *decreases*. This fact

makes qualitative comparisons of the current carrying capabilities of the GBs in Figure 2.2 possible.

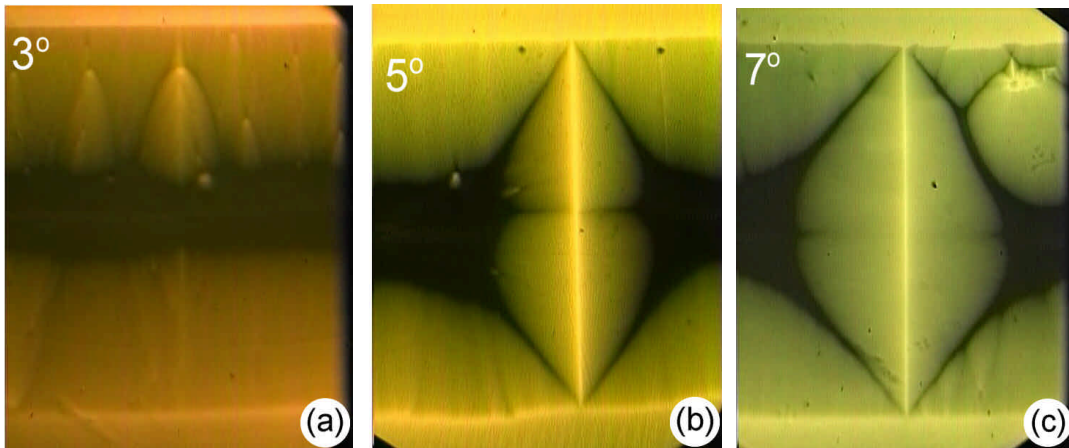


Figure 2.3. MO images of YBCO on [001] tilt STO GBs from reference [x]. The 3 degree GB, (a), is nearly invisible meaning that $J_{cb} = J_{cg}$. The 5° (b) and 7° (c) GBs are clearly visible, and have $J_{cb} < J_{cg}$. While it is not apparent from the MO images above, the magnitude of the flux penetration at the 7° GB is greater than at the 5° GB. The fact that the 3° GB does not admit flux and the 5° and 7° GB do fits well with the $J_c(\mathbf{q})$ dependence show in Figure 1.3. MO images were taken by Anatolii Polyanskii (UW).

In order to make the comparisons, the relative magnitude of the flux penetration at more than 60 GBs in Figure 2.2 was measured. This was done by averaging the pixel intensity along (not transverse) the GBs in the MO image of Figure 2.2(a) using an image analysis software. The pixel intensity of the digital image scales linearly with magnetic field strength. As only qualitative comparisons are possible, the absolute value of the magnetic field at each GB is not important. The intensities at the GBs were then correlated to the GB misorientation angle (\mathbf{q}) measured in the Ni substrate. Orientation mapping (see Appendix B) was used to determine the \mathbf{q} of each GB. The resulting data is plotted in Figure 2.4. There is a sharp threshold at 4°; flux does not penetrate above Ni

GBs with $q < 4^\circ$, while GBs with $q > 4^\circ$ do admit flux. It can also be seen that the magnitude of flux penetration for $q > 4^\circ$ varies considerably and not very systematically with q , suggesting that variables other than q are having an influence on GB properties.

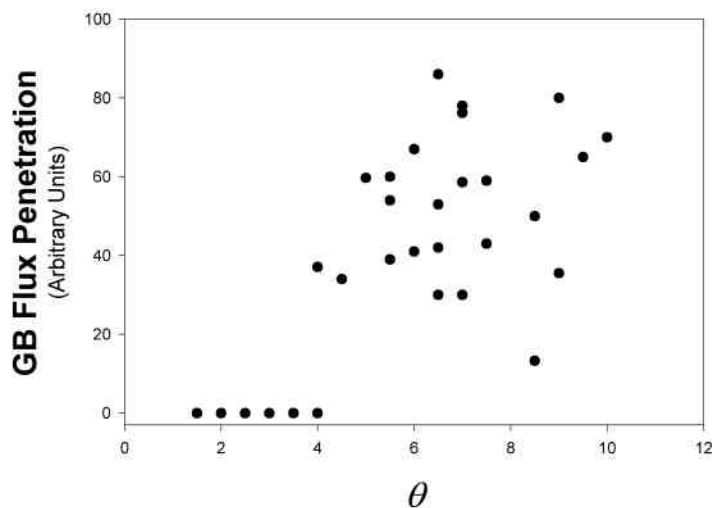


Figure 2.4. Intensity of flux penetration vs. GB misorientation angle as determined by EBSD analysis for more than 60 GBs in Figure 2.2. The flux intensity was determined by averaging the pixel intensity along the GB. The pixel intensity varies directly with magnetic field. EBSD data was collected by Rama Nekkenti of Air Force Research Laboratory and analyzed by Jodi Reeves (UW).

Figure 2.5 shows a series of *grain boundary maps* for a subset of the MO image of Figure 2.2(a). These grain boundary maps were created from orientation mapping data taken on the Ni substrate. Figures 2.5(a), (b) and (c) show all GBs with $q \geq 1^\circ$, 4° , and 7° respectively. There are only a few GBs in the Ni greater than 7° . Comparison of the $q \geq 4^\circ$ GB map [Figure 2.5(b)] with the visible GBs in the MO image of the same region

[Figure 2.5(d)] yields a nearly one-to-one correlation. This is consistent with the plot of Figure 2.4, and yields a q_c of 4° , as defined in Chapter One.

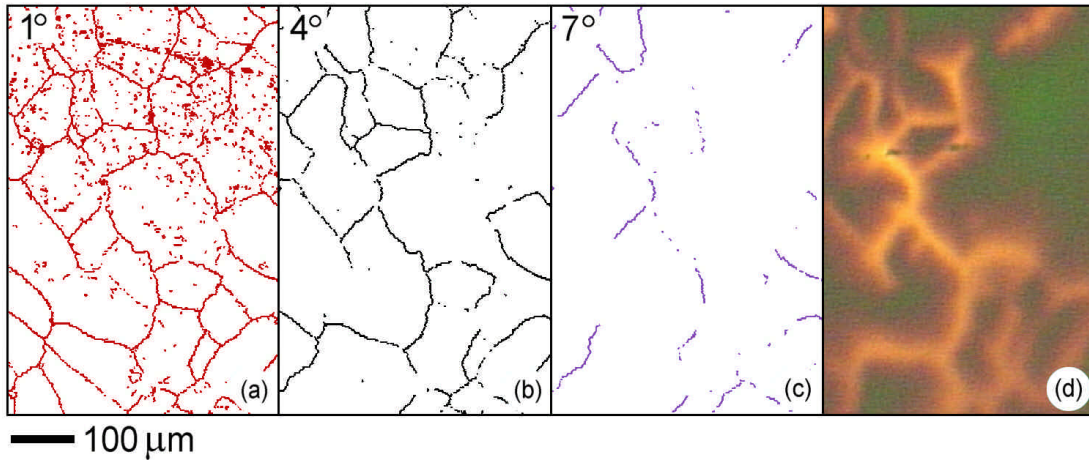


Figure 2.5. MO images and corresponding GB maps. The data was taken on a $3 \mu\text{m}$ grid over a roughly $300 \times 500 \mu\text{m}$ area. (a)-(c) Grain boundary maps of the location of all GBs with $q \geq 1^\circ$, 4° , and 7° respectively. (d) MO image of the same region as the maps of (a)-(c).

The montage of Figure 2.2 nicely demonstrates the influence of the Ni substrate on the YBCO layer. The fact that some, but not all, of the GBs in the YBCO are visible in the MO image focuses attention on the factors that control when J_{cb} becomes less than J_{cg} for a given GB. Certainly q is one strong factor, but comparing the plot of Figure 2.4 to the $J_c(q)$ dependence of Figure 1.3 suggests the influence of other factors as well. The q_c of 4° found here is a bit higher than that shown in Figure 1.3, and also of concern is the variability in flux penetration in Figure 2.4 for $q \geq 4^\circ$. Since J_{cb} decreases with increasing q , a steady increase of the relative flux penetration with increasing q might

have been expected in Figure 2.4. However, the flux penetration at a GB increases as J_{cb}/J_{cg} decreases, variations of the intra-grain J_c could also account for the scatter above 4° . In Chapter Four it will be shown that the variations in the intra-grain J_c that do exist are not sufficient to account for the degree of scatter in Figure 2.4, which points again to factors other than \mathbf{q} having an influence on J_{cb} . One possibility is that none of the CC GBs are pure [001] tilt. The misorientation axes of the GBs in the Ni are randomly distributed near the [001], [011] and [111] directions, and in general the GBs have varying amounts of tilt and twist components. Grooving of the GBs in the Ni may also play a role in determining J_c . A third point to consider is that the GB angles were measured in the Ni, but it is the GB angles in the YBCO that determine J_{cb} . If the YBCO and the buffer layers are truly growing epitaxially on the Ni, than this angle should be the same. However, x-ray diffraction data taken on tapes before and after YBCO deposition has suggested that there is an improvement in the *c-axis* alignment of the YBCO grains relative to the Ni [44]. A change in the orientation of the grains would lead to a change in \mathbf{q} . This x-ray diffraction data is not conclusive, as it is averaged over thousands of grains and cannot examine the oxide layers individually. To investigate this possible explanation further a detailed analysis was done with orientation mapping.

2.3 Texture development

In order to investigate a possible change in \mathbf{q} from the Ni to the YBCO layer, a series of orientation maps were taken on a fresh sample. This sample was grown on a

commercial Ni substrate, and had significantly poorer texture than the sample shown in Figure 2.2. The structure of the sample was Ni/Y₂O₃/YSZ/CeO₂/YBCO with the YBCO layer grown by the BaF₂ process. The sample had a $J_c(77\text{ K}, 0\text{ T})$ value of 0.7 MA/cm². Orientation mapping was performed on the YBCO layer, the YSZ layer, and the Ni substrate all in the same location. Orientation mapping is sensitive to only the top ~50 nm of the film, so the orientation of each layer can be accurately determined without concern for the influence of underlying layers (unlike x-ray diffraction). After all data collection on the YBCO layer, the YBCO and CeO₂ layers were removed with a weak nitric acid etch. The YSZ and Y₂O₃ layers were removed by ion milling to expose the Ni substrate. A schematic of the experiment is shown in Figure 2.6.

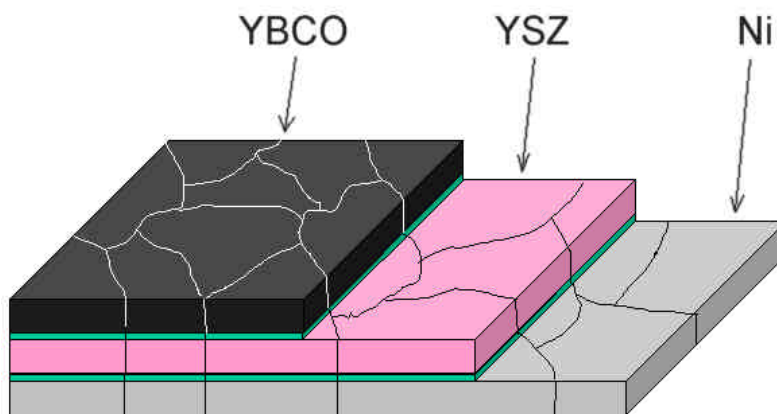


Figure 2.6. Diagram showing the layers of the CC on which orientation mapping was performed. The structure of the sample was Ni/Y₂O₃/YSZ/CeO₂/YBCO. The orientation maps of all three layers (YBCO, YSZ and Ni) were performed in the same location in order to track changes in \mathbf{q} from the Ni to the YBCO layer.

Data from the orientation mapping is shown in Table 2.2. The measurement region was ~275 x 500 μm , and the density of the orientation maps was 200 x 300 points

or greater. The data on the YSZ and Ni layers was obtained at the University of Wisconsin using a LEO-1530 field emission SEM (FESEM). The data on the YBCO was obtained at NORAN Instruments. Getting good orientation data off of YBCO is usually very difficult, due to low signal to noise ratios. The reasons for the low ratio are unclear, and do not correlate with J_c or other obvious factors. To improve the signal-to-noise ratio for the YBCO, the sample was taken to NORAN Instruments and orientation mapping was performed in a regular (tungsten filament) SEM. This SEM can produce much higher beam currents than are possible in an FESEM, and this improves the signal to noise ratio. However, the orientation data on the YBCO remained noisier than the data from the YSZ or the Ni. At 4° , all three GB maps look very similar. At 7° there is a reduced number of GBs in the YBCO relative to the YSZ and Ni, and there are far fewer GBs $> 10^\circ$ in the YBCO than in the Ni or the YSZ. Table 2.2 suggests that the orientation of the YSZ and the Ni is roughly the same, while there is a change in orientation between the YSZ and the YBCO that leads to an improvement in q . Figure 2.7(a) and (b) shows c -axis alignment maps of the YBCO and YSZ layers. From the legend, it is clear that the improvement in q seen in Table 2.2 is due to an improvement of the c -axis alignment of the YBCO relative to the YSZ. The improvement in c -axis alignment is likely due to the fact that the Ni and the YSZ are cubic, while the YBCO is orthorhombic with $a = b = 0.38$ and $c = 1.17$ nm.

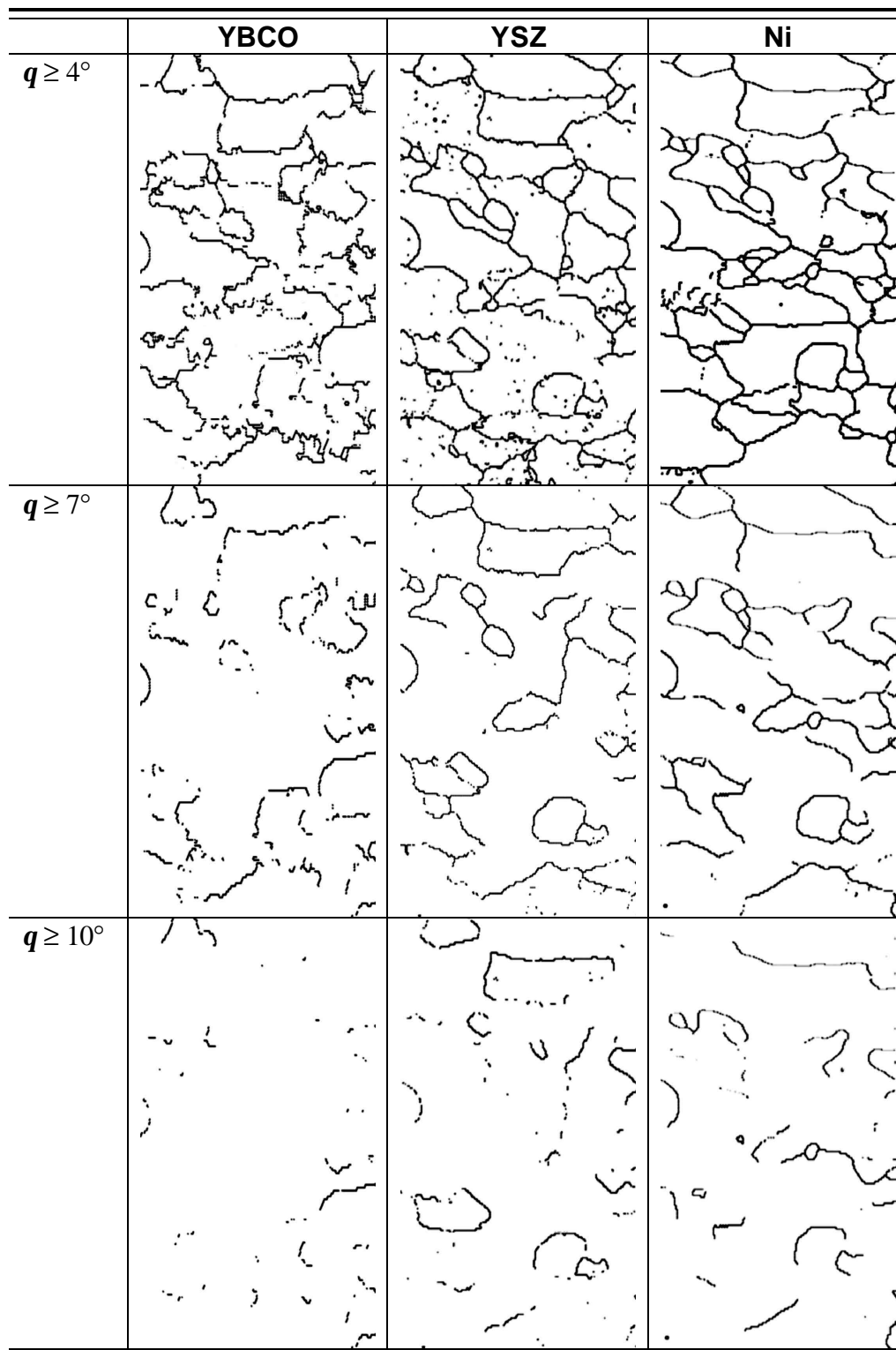


Table 2.2. GB maps from the YBCO, YSZ, and Ni in the same location. Due to a poorer signal to noise ratio, the YBCO data is noisier than the YSZ or Ni data. The YBCO data was collected at NORAN instruments.

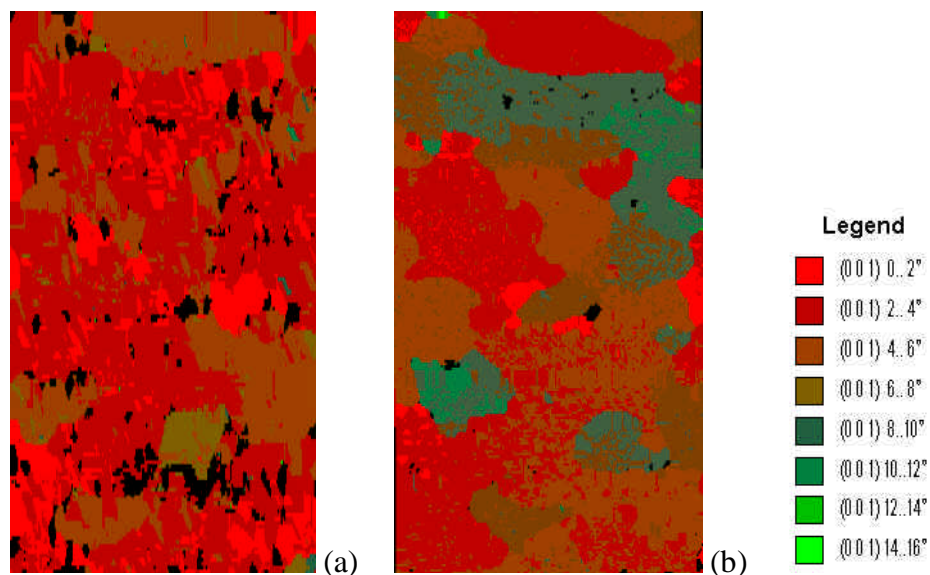


Figure 2.7. Maps showing the c -axis alignment of the (a) YBCO and (b) YSZ layers. The images are colored according to how closely the c -axis of the grains aligns with the sample's normal. Black regions are areas where no data was obtainable. The legend applies to both figures.

Next, the misorientation angles of more than 50 individual GBs from Table 2.2 were tracked from the Ni to the YBCO layer. Table 2.3 summarizes the results. The average improvement in \mathbf{q} between the Ni and YSZ is negligible while the average improvement from the Ni to the YBCO is substantial, 2.86° . However, the GB maps of Table 2.2 suggest that the degree of improvement depends on the original \mathbf{q} in the Ni. Figure 2.8(a) plots the improvement in \mathbf{q} from the Ni to the YBCO against the \mathbf{q} in the Ni. From the plot, larger improvements in \mathbf{q} are more likely for higher angle GBs in the Ni. This is not surprising, as larger c -axis misalignments are likely to result in larger \mathbf{q} values, and would have more room for improvement. The scatter in the data occurs because the degree of improvement in \mathbf{q} is a complex function of the magnitude and direction of the c -axis alignment of the two grains that form the GB. Plotting the improvement in \mathbf{q} against \mathbf{q} in the Ni is a simplification. For example, consider two

adjacent Ni grains both with their c -axis perfectly aligned but which have a large in-plane misalignment. In this case q will be large, but since the c -axes of the grains are already aligned there is no mechanism for improvement of q between the Ni and the YBCO. Figure 2.8(b) plots the change in q from the Ni to the YSZ against the q in the Ni. There is a slight improvement in q at higher angles, but generally q in the YSZ and the Ni are very close.

	Average q improvement	Maximum q improvement	Minimum q improvement
Ni to YBCO	2.86°	7.3°	-2.0°
Ni to YSZ	0.38°	1.8°	-3.8°
YSZ to YBCO	2.49°	5.7°	-0.5°

Table 2.3. Results of tracking the q of individual GBs from the Ni to the YSZ to the YBCO. A negative number means q became worse (larger).

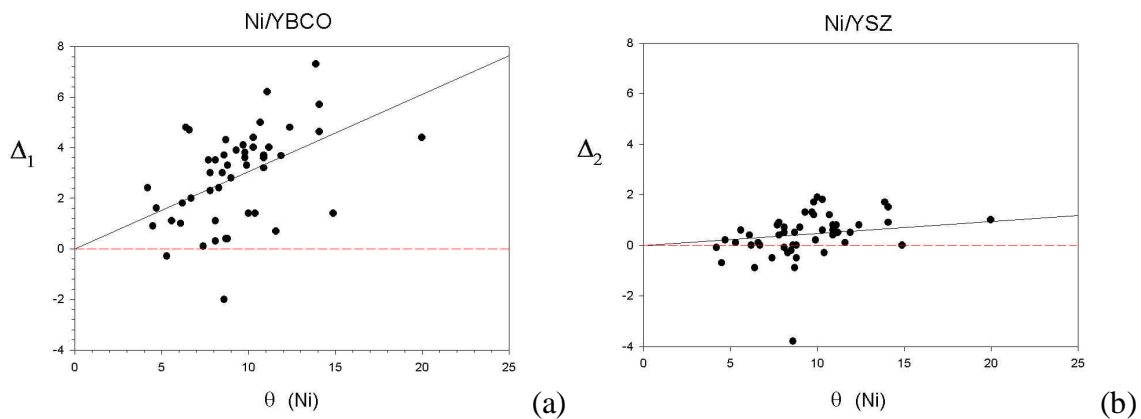


Figure 2.8. Plots of improvement in q as a function of q in the Ni substrate. The black lines are linear fits (through the origin) to the data. The red lines separate positive from negative improvements. (a) Plot of $\Delta_1 = q(\text{Ni}) - q(\text{YBCO})$ vs. $q(\text{Ni})$. (b) Plot of $\Delta_2 = q(\text{Ni}) - q(\text{YSZ})$ vs. $q(\text{Ni})$.

Recall that the motivation to investigate the texture change from the Ni to the YBCO was a slightly high value of q_c and a lot of scatter in the plot of Figure 2.4. Judging from the scatter in the plot of Figure 2.8(a), the GBs in the Ni of Figure 2.2(c) would have propagated through to the YBCO with varying degrees of improvement in q . This would explain the variation in flux penetration in Figure 2.4, as the relative magnitude of the flux was plotted against q in the Ni and not the YBCO. Also, a q_c value of 4° as measured in the Ni would be $\sim 3^\circ$ in the YBCO, according to the linear fit in Figure 2.8(a). A q_c value of 3° fits better with the $J_c(q)$ dependence shown in Figure 1.3. However, the sample of Figure 2.2 was grown on a substrate with a better degree of texture than the one used for Figure 2.8(a). In fact, Figure 2.8(a) shows that there were no Ni GBs in the measurement region that had a q less than 4° . This analysis would benefit from additional data in Figure 2.8(a) below 4° .

2.4 Summary

It has been demonstrated that the polycrystalline substrates used in deformation textured CCs produce a network of GBs in the YBCO, a fact not previously accepted. The GB network in the YBCO is responsible for the electromagnetic granularity seen in dozens of MO images, and analysis of these images showed that current is percolating through the conductor. From the results of a previous bicrystal study [42] and the analysis of flux profiles [such as the one in Figure 2.1(c)] we know that these visible GBs

do carry current, but have a reduced J_c relative to the intra-grain. However, some GBs are not visible in the MO images, which means that $J_{cb} = J_{cg}$ for those boundaries. Understanding why some GBs have a J_c less than that of the intra-grain while others do not is of paramount importance to the improvement of the overall J_c of CCs. Figure 2.4 shows that whether J_{cb} is less than J_{cg} for a given GB depends strongly on \mathbf{q} . The fact that $J_{cb} = J_{cg}$ below 4° in the plot of Figure of 2.4 is qualitatively consistent with the idea of a critical angle (\mathbf{q}_c) as discussed in Chapter One, but a \mathbf{q}_c of 4° is perhaps a little high when compared to the $J_c(\mathbf{q})$ dependence shown in Figure 1.3. Analysis of the texture change from the Ni to the YBCO reveals that the \mathbf{q}_c of 4° found from measuring the GB angles in the Ni is likely an overestimate, and the true \mathbf{q}_c (in the YBCO) for the sample of Figure 2.2 is probably $\sim 3^\circ$.

In understanding and interpreting the data in following chapters, it is important to remember the results of the texture analysis presented here. As mentioned, obtaining good orientation data off of YBCO was always difficult, if possible at all. The odds of obtaining good data improve when the sample is very fresh (recently grown), but even then the data acquisition times are much longer than they are for Ni. For example, orientation data are presented in the next chapter that consisted of more than 400,000 points in a single map. This data was taken off a Ni substrate and took 58 hours to acquire. A map the same size on the YBCO would have taken two weeks to acquire, which is an unreasonable number of consecutive days of SEM time, especially on a multiple user system. Often there is little choice but to obtain orientation data from the Ni alone. This texture analysis provides the first conclusive demonstration of an improvement in the *c-axis* alignment of the YBCO relative to the Ni, and the first

demonstration that q is improving as well. A subsequent analysis done by J. Reeves [45] has found the same results in different samples. The fact that q is improving from the Ni to the YBCO and the plot of Figure 2.8(a) will aid in interpreting Ni GB maps in the next chapters.

3

Visualization of the self field of deformation textured coated conductors

In the previous chapter it was shown how the grain structure of the substrate influences the YBCO above it. This was done using MO imaging under an externally applied field, light microscopy, and orientation mapping. However, many counter arguments were proposed among the community to explain what was being seen in the MO images. Nearly all arguments centered on the fact that the MO imaging had been done under the presence of magnetization currents resulting from an externally applied magnetic field. It was suggested that the current percolation seen under magnetization currents was not representative of *transport* current flow. Because of these concerns and because of the potential for gaining new information, the next logical step was to magneto-optically image a CC under an applied transport current.

3.1 Comparing and contrasting magnetization and transport MO imaging

Magnetization MO imaging is relatively simple and is non-destructive to the sample. Currents are induced in a superconducting sample by the application or removal

of an externally applied magnetic field. The zero field cooled (ZFC) and field cooled (FC) states described in Appendix A are examples of magnetization MO imaging. Magnetization currents flow in loops, whose size and shape depend on the geometry of the sample. Many loops may be ‘superimposed’ on each other in a highly granular sample. There may be large macroscopic current loops superimposed on smaller loops flowing inside individual grains, as shown in Figures 2.1. With magnetization currents alone flowing in a sample, the z -component of the magnetic field (observed by MO imaging) has the same direction (either into or out of the page) at all sample edges. This is shown in Figure 3.1. By applying a sufficiently high field, the critical state can be induced in the sample; that is to say currents are flowing at the local value of J_c everywhere. In a granular film such as YBCO on a deformation textured substrate, inducing the critical state will identify which GBs have a J_c greater than or less than the intra-grain. This is possible because (as already discussed in Chapter Two) only GBs with a J_c less than that of the intra-grain will appear in MO imaging.

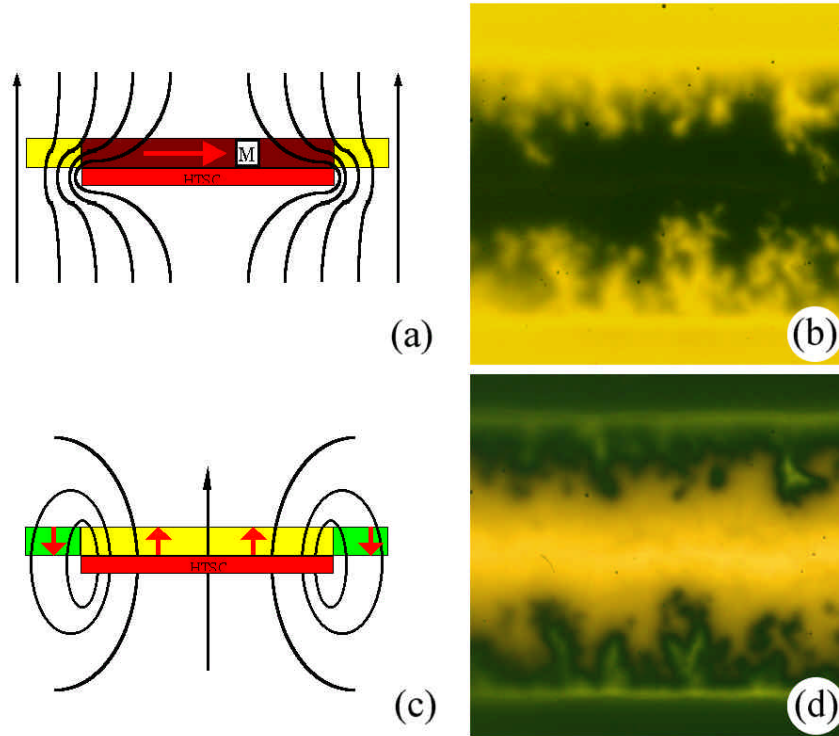


Figure 3.1. Field cooled (FC) and zero field cooled (ZFC) images in the presence of magnetization currents. The direction of the magnetic field is the same at all sample edges. (a) Schematic cross section of a ZFC sample showing the magnetic field lines and the response of the indicator film. (b) Corresponding MO image of a CC. The sample was ZFC to 77 K, and then a field of 40 mT was applied. (c) Schematic cross section of a FC sample showing the magnetic field lines and the response of the indicator film. (d) Corresponding MO image of the same CC as in (c). For this image, the sample was FC in a field of 60 mT to 77 K, and then the field was removed.

In transport MO imaging, no external magnetic field is applied, and the magnetic field imaged is produced from the transport current. Therefore, transport MO imaging visualizes the *self-field* of the sample. It is more destructive, as it requires the attachment of leads for current and voltage, and the current flow is usually restricted by a user-defined link. Since the net current flow is from one end of the link to the other, the z -component of the magnetic field has opposite directions on either side of the link (see Figure 3.2). This manifests itself as different colors at the sample edges in the MO image. Transport MO imaging seldom results in the critical state being established

everywhere in the sample (unless the sample is very uniform) since the dissipation is often localized. Because the critical state is not established, few conclusions can be drawn about the J_c of visible GBs relative to the intra-grain, but the GBs which do appear under an applied transport current often identify where J_c is being limited in a sample. The electric field under an applied transport current can also be very different from magnetization currents. With magnetization currents the electric field is nearly zero everywhere (neglecting thermal flux creep), while under transport current the electric field can be high if the sample is driven into the dissipative state. Of course, the magnitude of the field imaged under a transport current is generally much less than fields applied for magnetization imaging. Magnetization and transport MO imaging can provide complementary information, and both are valuable.

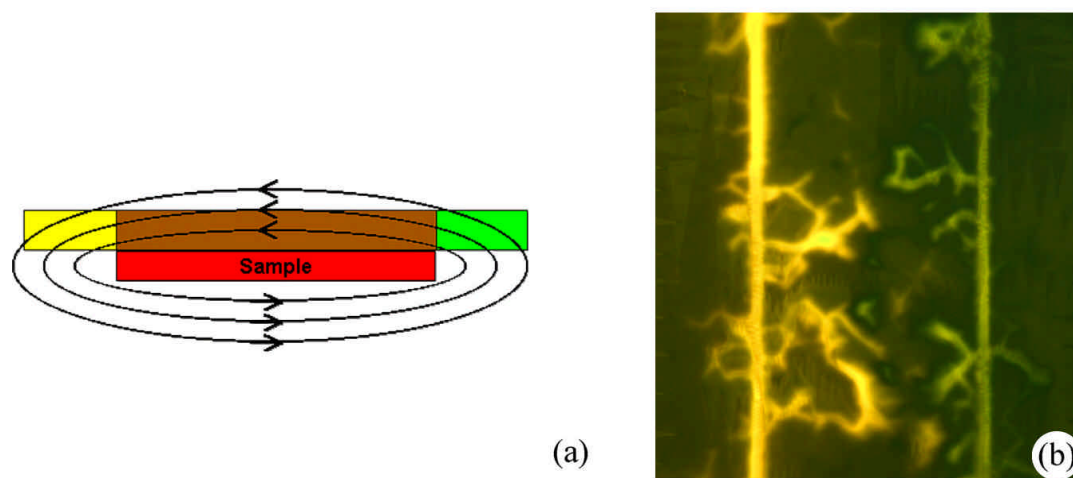


Figure 3.2. Schematic and MO image demonstrating the different directions of the magnetic field at the sample edges. (a) Schematic cross section of a sample under an applied transport current. With current flowing out of the page, the magnetic field wraps around the sample as shown. Since the indicator film is only sensitive to the component of the magnetic field perpendicular to the film, the greatest response occurs at the sample edges. (b) MO image of a link in a CC under an applied transport current. For this image, the sample was cooled to 77 K in the absence of an applied field, and then a *current* of 3A was applied.

3.2 Experimental

Three samples were included in this study, and their properties and names are listed in Table 3.1. Voltage and current pads were created when necessary by Ag sputtering. The samples were masked prior to Ag deposition in order to restrict the size of the pads, keep the link area free of Ag, and avoid shorting of the pads to the Ni substrate. The samples were 3-5 mm in width, and 5-15 mm long. Full width critical currents can exceed 25A, and are usually determined by pulse current measurements. For MO imaging it is necessary to apply a continuous current, and sample size did not permit continuous currents above 3A without excessive heating. Also, the sample consists of thousands of Ni grains, and it is desirable to reduce the number of grain boundaries of interest to a more manageable number for later orientation mapping. For these reasons, a laser was used to cut links, thereby restricting the current flow and defining the measurement region. Wires were attached to the Ag pads using Ag paste (Amicon 850-C). The paste is cured by heating the sample to 90°C for 10 minutes. This was done with a thermostatically controlled hot plate in flowing nitrogen to keep H₂O vapor off the sample. The sample is then mounted in the MO cryostat. An image of a mounted sample is shown in Figure 3.3. Transport (voltage-current) data was taken in-situ using LabVIEW programs, a Keithley 2420 current source, and a Hewlett Packard 34420A

nano-voltmeter. In most cases, it was not possible to obtain orientation data on the YBCO. Therefore, after measurement, the YBCO and buffer layers were removed as described in Chapter 2, and orientation mapping was then performed on the Ni substrate in the measurement region. For in-field measurements, the sample was placed in a 1 T electromagnet or a 13 T superconducting magnet. In either case the sample was immersed in LN₂ (77.25 K), and all reported J_c values are at 77 K and were determined using the 1 μ V/cm criterion.

Name	Full-width J_c	Width*	Link J_c	Source
F159CN2	2.4 MA/cm ²	3.3 mm	0.7 MA/cm ²	ORNL [†]
F197CN1	0.7 MA/cm ²	3.3 mm	0.6 MA/cm ²	ORNL [†]
TFA1455	0.8 MA/cm ²	5 mm	1.3 MA/cm ²	AMSC [‡]

* Full width of sample before link was cut

[†] Oak Ridge National Laboratory

[‡] American Superconductor Corporation

^{††} As measured on the Ni substrate before oxide film growth

Table 3.1. Properties of the three samples in this study. The sample names were inherited from their sources.

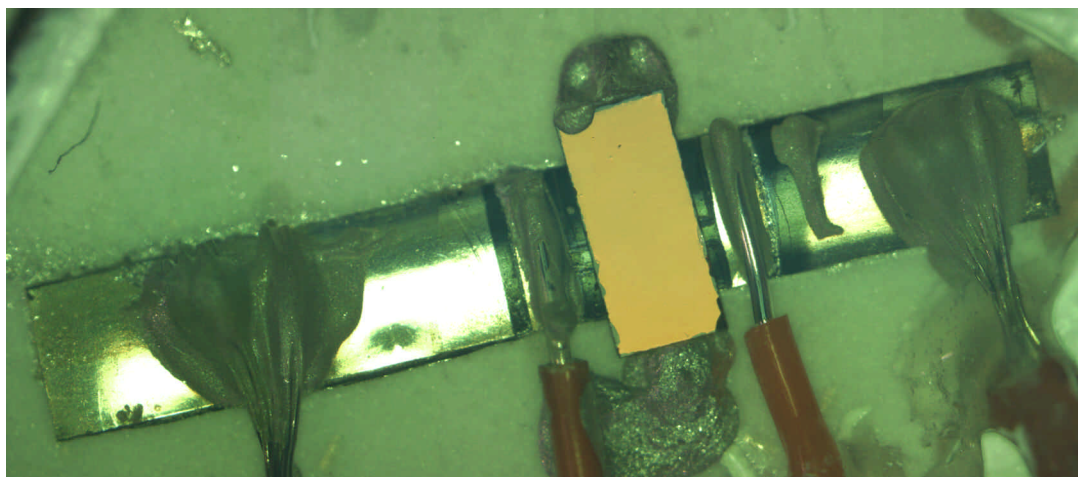
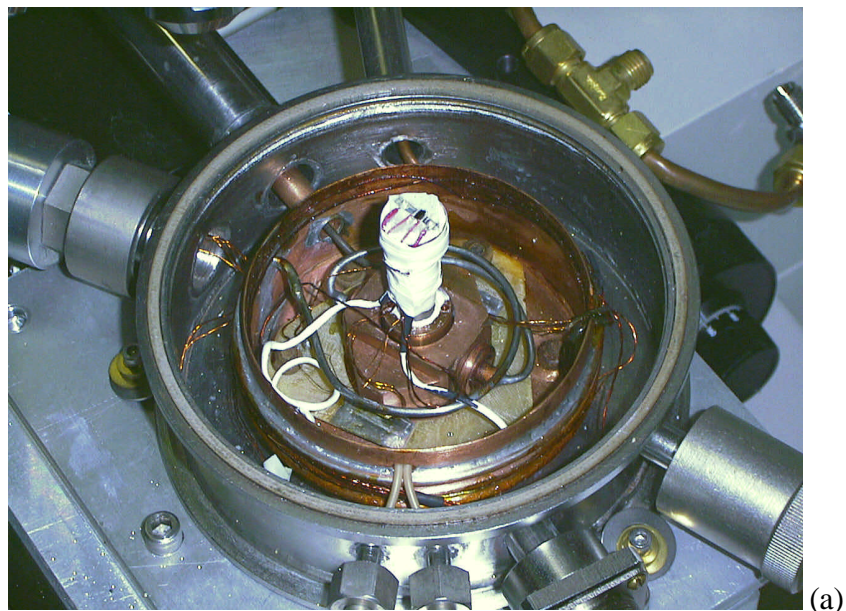


Figure 3.3. Images of the experimental setup for MO imaging under transport currents. The sample shown in the above images is F159CN2, but the same basic setup was used for all samples. (a) The MO imaging cryostat with sample mounted. The sample is placed diagonally across a piece of sapphire. Also visible are four red wires. The outer two are for application of current, the inner two are for measuring the voltage drop across the link. For more pictures of the cryostat please see Appendix A. (b) Surface image of the sample with indicator film in place. Ag paint was used to hold the indicator film in place.

3.3 Results and Discussion

3.3.1 Magneto-optical imaging of transport current in F159CN2

Figure 3.4(a) shows a MO image of F159CN2 before laser cutting. The sample was deposited on a well-textured laboratory grown Ni substrate, and had a very high full-width J_c value of 2.4 MA/cm^2 . The flux penetration is clearly granular, as described in Chapter Two. After characterization at full width, a track $1.8 \text{ mm} \times 265 \text{ }\mu\text{m}$ was cut using a laser. The average grain size of the Ni substrate was $\sim 60 \text{ }\mu\text{m}$; thus the track was $\sim 4\text{-}5$ grains wide and ~ 30 grains long. The relative size and spacing of this link on the sample is shown in Figure 3.4(b). This link had a $J_c(0\text{T}, 77\text{K})$ value of 0.7 MA/cm^2 , less than one-third of the full width measured value. Figure 3.5 shows voltage-current characteristics and $J_c(H)$ dependence up to 1T.

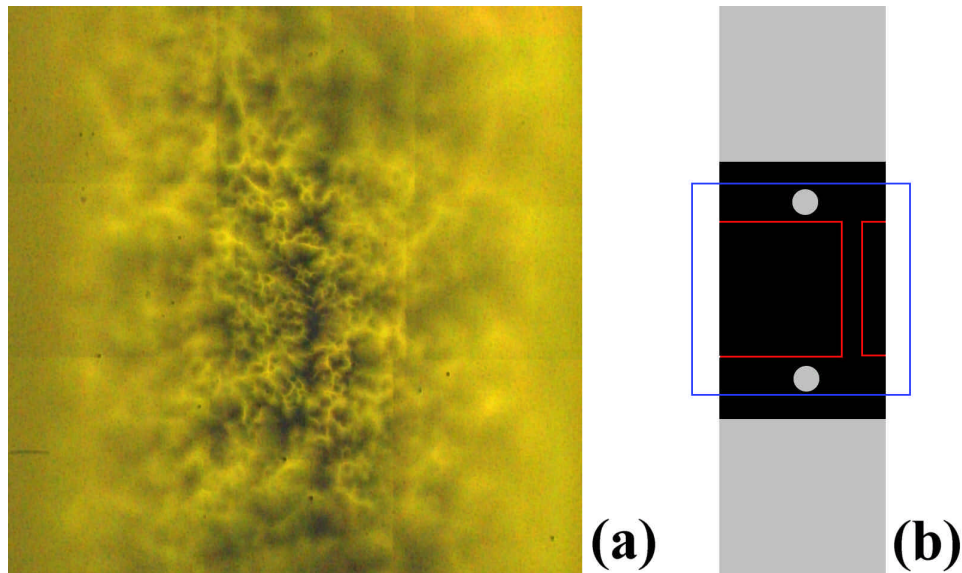


Figure 3.4. A MO image and geometry of the experiment. (a) Magneto-optical image across the whole width of the sample. For this image, the sample was ZFC to 77 K, and then a field of 80 mT was applied. (b) Geometry of the sample. Black is exposed YBCO, and gray is where Ag has been deposited on the YBCO. The blue box represents the area of the MO image in (a), and the red lines indicate the approximate location of laser cuts used to define the link.

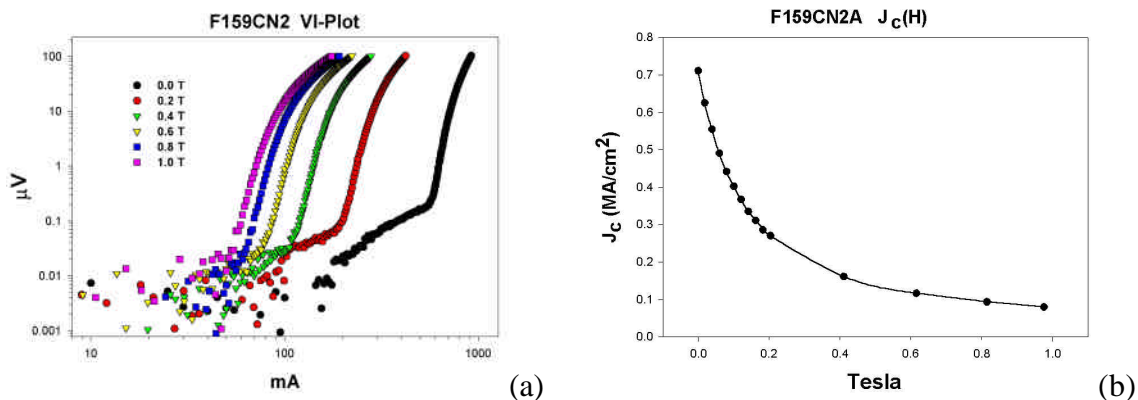


Figure 3.5. (a) Voltage-current data taken from the link cut in F159CN2. The plots have an ohmic “foot”, most pronounced at 0 T and almost absent at 1 T, due to shorting between the voltage taps and the Ni substrate. The electric field criterion of $1 \mu\text{V}/\text{cm}$ J_c criterion yields a voltage criterion of $0.2 \mu\text{V}$ for this link, and the ohmic foot did not affect determination of J_c . The plots are rather curved above $10 \mu\text{V}$ (much more so than would be expected for a single-crystal), indicative of the influence of GBs in the link. (b) A plot of $J_c(H)$.

Figures 3.6(a) and (c) are MO images of magnetization currents flowing in the track. For Figure 3.6(a), the sample was ZFC to 77 K, then a field of 4.0 mT was applied. As the applied field is increased flux penetrates into the bulk, but propagates preferentially along weaker-linked regions such as some GBs. At 77 K, 4.0 mT was insufficient to induce the critical state in the link. At lower applied fields the weaker-linked (lower J_c) GBs appear first.

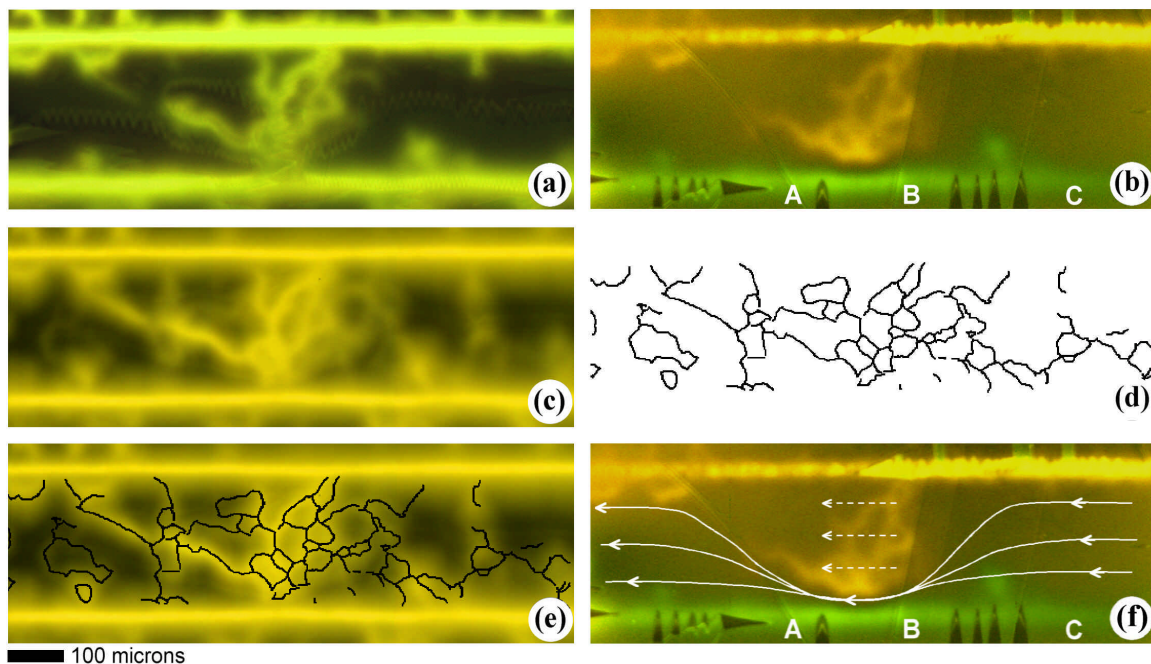


Figure 3.6. MO images and EBKP data of the link cut in F159CN1. EBKP data for this sample only was collected by Oxford Instruments and analyzed by Jodi Reeves. (a) MO image of magnetization currents. For this image, the sample was ZFC to 77 K and then a field of 4.0 mT was applied. (b) MO image of the self-field due to transport currents. The sample was ZFC to 77 K and then a current of 700 mA was applied. There was no externally applied magnetic field. (c) MO image of magnetization currents. For this image the sample was ZFC to 40 K, and then a field of 60 mT was applied. (d) GB map showing all GBs with misorientation angles $\geq 5^\circ$. This map matches well to the flux penetration seen in the MO image in (c). (e) Overlay of (c) and (d). Most of the GBs $\geq 5^\circ$ permit flux penetration, while those $< 5^\circ$ do not. (f) Same as (b), with arrows showing the general direction of current flow. An unknown fraction of the total applied current crosses the GB cluster (dashed arrows), while the remaining percolates around the cluster. On either side of the cluster, current flows more uniformly.

In Figure 3.6(c) the link has been cooled to 40 K, and then a field of 40 mT was applied. This was sufficient to induce the critical state in the link as was verified by a series of FC images. When the sample is in the critical state, GBs appear if the critical current density of the GB (J_{cb}) is less than the immediately surrounding intra-grain (J_{cg}). Therefore in a granular system MO imaging is sensitive to the ratio J_{cb}/J_{cg} , and variations in J_{cg} will also influence whether a GB is visible in MO imaging or not. In deformation textured CCs it is expected that J_{cg} will be more variable than in single crystal or bi-

crystal substrates as each substrate grain provides its own single crystal template for film growth. Variation in the vicinal angle and other factors may contribute to variations in J_{cg} , but in Chapter Four it will be shown that the variation of the intra-grain J_c is not too large. Visible GBs thus indicate where locally the ratio of J_{cb}/J_{cg} is less than unity, though in general no inference can be made regarding the absolute values of J_{cb} and J_{cg} .

Figure 3.6(b) is a MO image of the self-field produced by transport current in the link. The sample was ZFC to 77 K, and then a current of 700 mA was applied. V-I data was taken during MO imaging [the zero field trace shown in Figure 3.5(a)] and I_c was found to be 560 mA (0.7 MA/cm²). It is immediately apparent that the MO image of transport currents very closely resembles the image of magnetization currents, Figure 3.6(a). This reaffirms MO imaging under *magnetization* currents as a valid method of identifying *transport* current limiting defects even though there can be great differences in the electric field. The major current limiting obstacle in the link is the GB cluster in the center, between the markers **A** and **B** in Figure 3.6(b). Notice that under transport currents the flux penetration at the bottom of the GB cluster is increased relative to the rest of the cluster, unlike Figure 3.6(a). There is a clear gap in the magnetic flux between the GB cluster and the bottom edge of the link, and a change in sign in magnetic field. This means that a large fraction of the current in the track is being constricted and forced to flow between the grain boundary cluster and the bottom edge of the track in the region **A-B**. In the region **B-C** of the track, current flows mostly at the edges of the link, as predicted for a uniform superconducting thin strip [46,47]. This is diagrammed by in Figure 3.6(f). The dashed arrows represent the current that is crossing the GB cluster, while the remaining current percolates around the cluster at the bottom of the link.

Unfortunately, it is not possible to quantitatively determine the fraction of current crossing the cluster using the MO image alone.

Further understanding can be gained by quantifying the GB angles in the link. For this purpose, orientation mapping was done using Electron Backscatter Kikuchi Pattern (EBKP) analysis as described in Appendix B. It was not possible to obtain EBKP data off of the YBCO layer, so orientation mapping was done on the Ni substrate. Figure 3.6(d) is a map of all Ni GBs with angles $\geq 5^\circ$. The overlay of Figures 3.6(c) and (d), Figure 3.6(e), shows that the $\geq 5^\circ$ GB map correlates well with the MO image. This suggests a \mathbf{q}_c of $\sim 5^\circ$, rather high when compared to the $J_c(\mathbf{q})$ dependence shown in Figure 1.2. In fact, a \mathbf{q}_c of 5° would yield an intra-grain J_c value of $\sim 1 \text{ MA/cm}^2$, a rather nonsensical value when compared to the full-width J_c of the sample of 2.4 MA/cm^2 . However, the results of the texture analysis in Chapter Two suggest that \mathbf{q}_c is probably closer to 3° , a value that better fits the bicrystal studies [5,6]. This also raises issues about the absolute magnitude of the inter and intra-grain J_c values, a subject tackled in the next Chapter.

Returning to the link of Figure 3.6, it is clear that there are far fewer GBs appearing in the MO image of transport currents [Figure 3.6(b)] than there are in the MO image of magnetization currents [Figure 3.6(c)]. For the applied transport current of 700 mA in Figure 3.6(b), only GBs $\geq 7^\circ$ appear. Figures 3.7 show the MO image of transport currents next to a map of all GBs $\geq 7^\circ$. This is not inconsistent with the results of the MO image of magnetization currents. From the MO image of the critical state, we know that any GB not appearing has $J_{cb}/J_{cg} = 1$, and any GB that is visible has $J_{cb}/J_{cg} < 1$. It might be expected that all GBs with $J_{cb}/J_{cg} < 1$ should appear under transport currents as well.

However, at the applied current of 700 mA, the GBs $\geq 7^\circ$ had already driven the whole track to an average electric field of $40 \mu\text{V}/\text{cm}$ before GBs $< 7^\circ$ had begun to dissipate. Would it be possible to drive the link with a high enough current, lower angle GBs would become visible, but it is likely that the localized dissipation caused by the cluster of $\geq 7^\circ$ GBs would destroy the link long before other GBs were visible.

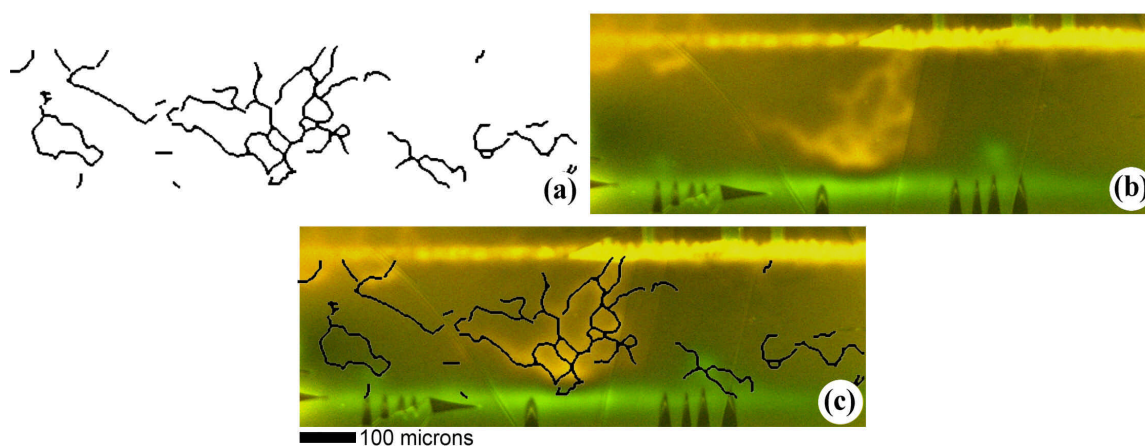


Figure 3.7. MO images of F159CN2 under an applied transport current, and EBKP data. (a) A map of all GBs in the link with misorientation angles $\geq 7^\circ$. (b) MO image of the self-field in the link. For this image, the sample was ZFC to 77 K and then a current of 700 mA was applied. (c) Overlay of (a) and (b). There is a good, though not perfect, correlation between the GBs that are $\geq 7^\circ$ and those GBs appearing in the MO image.

Figure 3.8 is a series of MO images showing the link at increasingly higher applied currents. All are images of self-field with no externally applied magnetic field. One very important observation from these images is that while the electric field [see Figure 3.5(a)] is changing dramatically from 3.8(a) to (h), the MO images show a very gradual change. In fact by considering only the MO images, it would be impossible to guess J_c . The “ohmic foot” in the V-I plots of Figure 3.5(a) makes the exact onset of

dissipation unclear, but correlation between the electric field and the MO images is illustrated further in the next section.

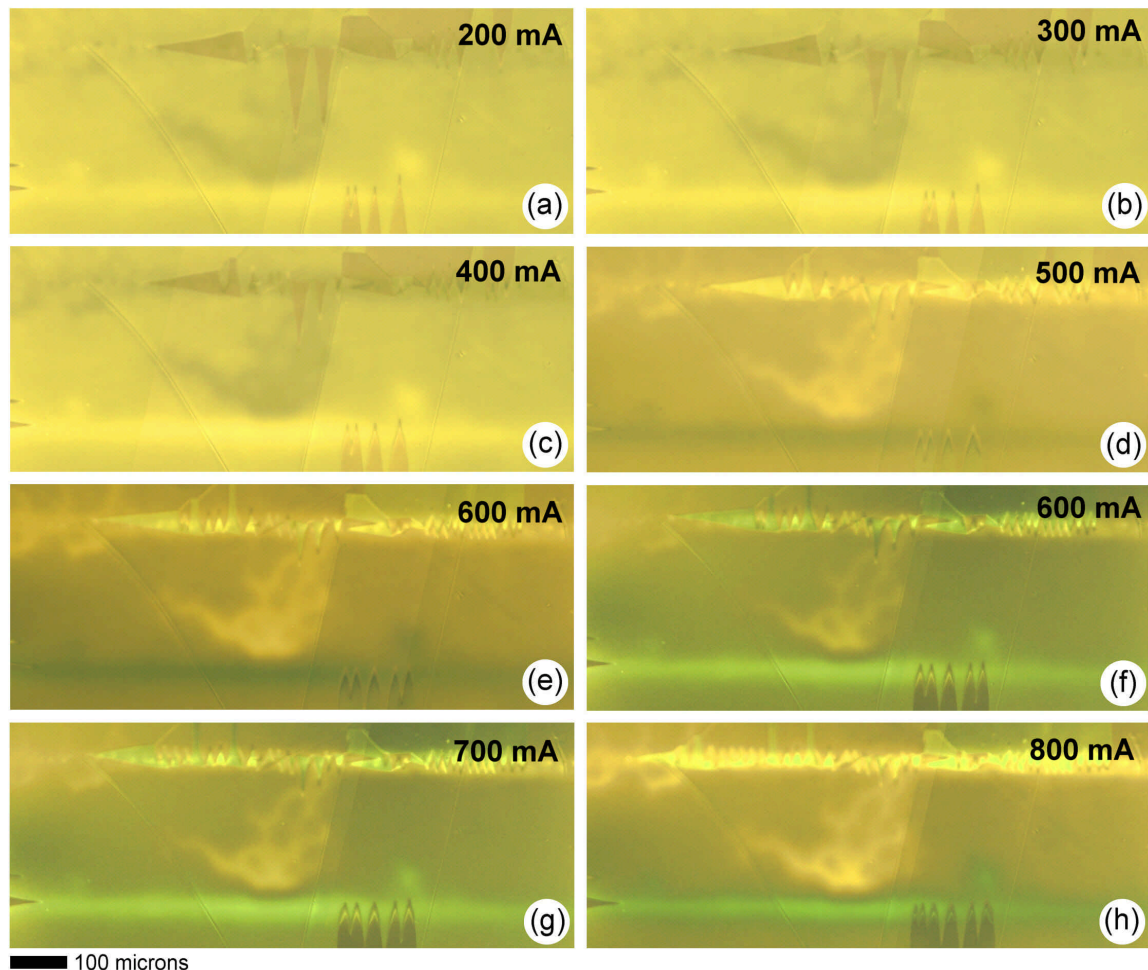


Figure 3.8. MO images of the link at increasingly higher applied currents. The I_c of the link was 560 mA. For these images, the sample was ZFC to 77 K, and was then subjected to increasing applied currents. The angle between the two polarizers (see A.4) of the microscope was changed for each image to ensure the best possible contrast. This had the result of changing the colors from one image to the next, a point that is demonstrated by the two images at 600 mA. (a) 200mA; (b) 300mA; (c) 400 mA; (d) 500 mA; (e)-(f) 600 mA. The only difference between these two images is the angle between the analyzer and the polarizer; (g) 700 mA; (h) 800 mA.

The MO images of the self-field of this link clearly demonstrate percolative current flow. This link was nearly 10% of the full-width of the sample, and had a J_c more

then one-third less (0.7 MA/cm^2). In order to obtain a full-width value of 2.3 MA/cm^2 , there must have been local regions with a J_c greater than 2.3 MA/cm^2 as well. Therefore the full-width J_c value was the result of current percolating through local regions of lower and higher J_c .

3.3.2 *Transport currents in F197CN1*

For sample F197CN1 it was desirable to define a link with a very different aspect ratio. A link $0.5 \text{ mm} \times 1 \text{ mm}$ long was cut using a laser. In terms of the grain size, the link was ~ 10 grains wide and ~ 16 grains long. Being shorter in length and many more grains wide than the link of F159CN2, there should be greater opportunity for current to find a high- J_c path across the link. Light microscope images of the surface of the sample after laser cutting are shown in Figures 3.9. The sample was grown on a commercial Ni substrate which had significantly worse texture than laboratory grown Ni used in F159CN2. The full-width J_c of the sample was commensurately less at 0.7 MA/cm^2 , and the link had a J_c value of 0.6 MA/cm^2 .

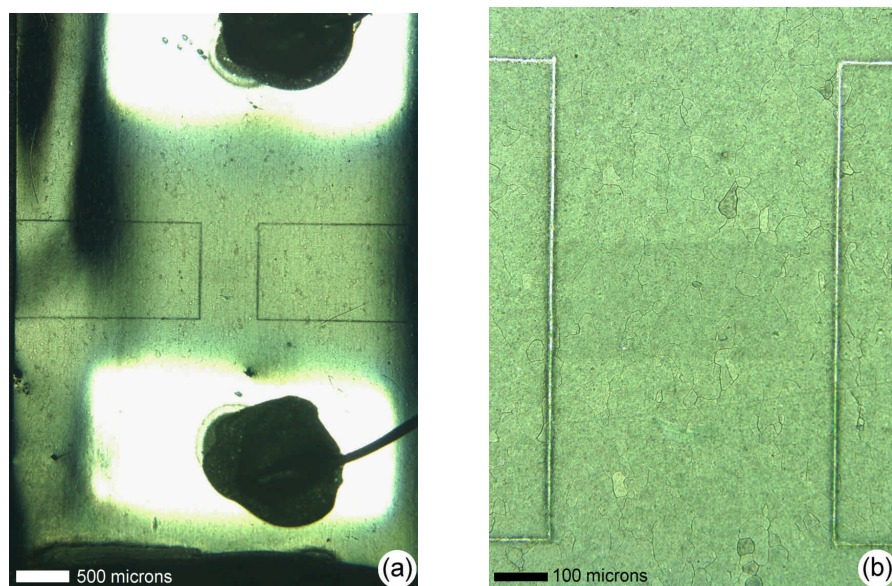


Figure 3.9. Surface images of F197CN1. (a) Surface image nearly across the 5 mm width of the sample. The YBCO appears green due to the reduced spectrum of the light source. Laser cuts defining the 0.5 mm x 1 mm track can be seen in the center of the image. Ag pads were sputtered for voltage contacts appear bright white. Voltage taps were attached with Ag paste, which can be seen in contrast against the Ag pads. Shadows occur on the surface due to the curvature of the sample. (b) A close-up of the link region. The darker rectangle across the center of the link is due to carbon deposition during a long EBKP scan in a SEM. It had no effect on the superconducting properties of the film. Data from this EBKP scan of the YBCO was discussed in Chapter Two.

Figure 3.10(b) shows a magnetization MO image of the link. For this image, the sample was ZFC to 40 K, and then a field of 20 mT was applied. In Figure 3.10(c), the sample was ZFC to 40 K and then a field of 60 mT was applied. This was sufficient to put the sample in the critical state. Figure 3.10(a) is a surface image of the same region. Nearly all the GBs in the sample are visible in the Figure 3.10(c). This is consistent with the poorer texture of the Ni substrate. Poorer texture means that there will be a greater number of higher angle GBs and therefore a greater number of GBs with a ratio J_{cb}/J_{cg} less than unity. Recall that all GBs with J_{cb}/J_{cg} less than unity will appear in the MO image. The relatively low J_c of the link (and the whole sample) and the magnetization

MO image already very strongly suggest that the transport J_c values are being limited by the GBs and not the intra-grain J_c .

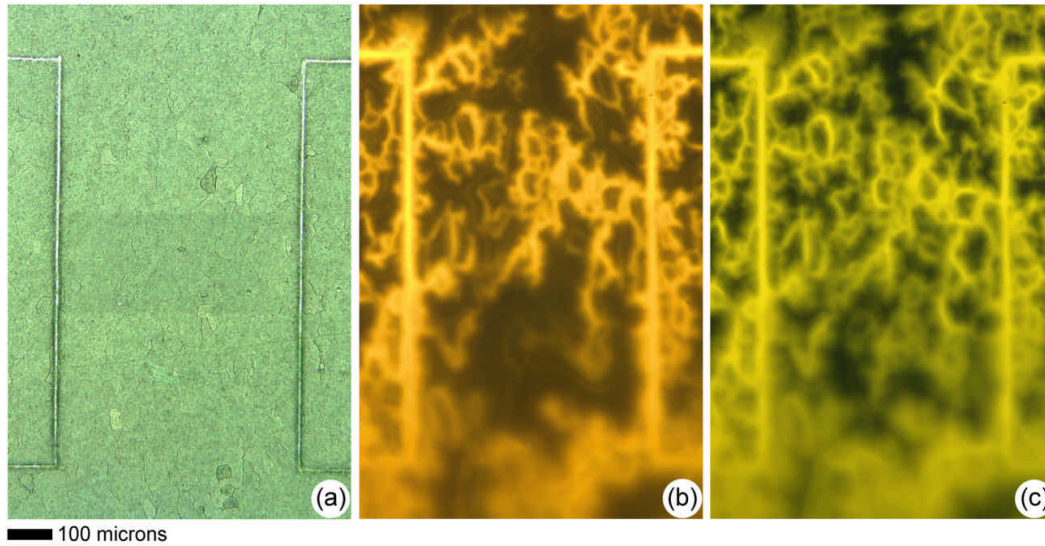


Figure 3.10. Surface and MO images of F197CN1. (a). Surface image of the link, same as Figure 3.9(b). (b). MO image under magnetization currents. For this image, the sample was ZFC to 40 K and then a field of 20 mT was applied. (c). MO image under magnetization currents. The sample was ZFC cooled to 40 K and then a field of 60 mT was applied.

An image of the self-field of the link at I_c is shown in Figure 3.11(a). Unlike the magnetization MO image, GBs are not visible throughout the link. Nearly all of the visible GBs are in the top half of the link. In the bottom half, current flows more uniformly, mostly near the edges of the link [46,47]. Figure 3.11(b) is the same as Figure 3.10(b). Comparison of these two images again shows the similarity between transport and magnetization MO imaging, and can also yield insight into why some GBs appear in the self-field image and others do not. As was discussed in Chapter Two, when magnetization currents are induced in the sample the flux penetration at a GB increases as the J_c of the GB decreases, at least for the simple geometry of a bicrystal. The

the J_c of the GB decreases, at least for the simple geometry of a bicrystal. The complicated geometry of GBs in a CC may have some influence as well, but in general we expect that the brightest GBs in Figure 3.11(b) should be the weakest linked. Looking at Figure 3.11(a), the visible GBs in the image are among the brightest GBs in the magnetization MO image, Figure 3.11(b). Also, all of the GBs visible in the self-field image are visible in the magnetization image, but the converse is not true. All GBs in the magnetization image have a J_c less than the intra-grain, yet as with the link of F159CN2 not all of these GBs are visible in the self-field image at I_c .

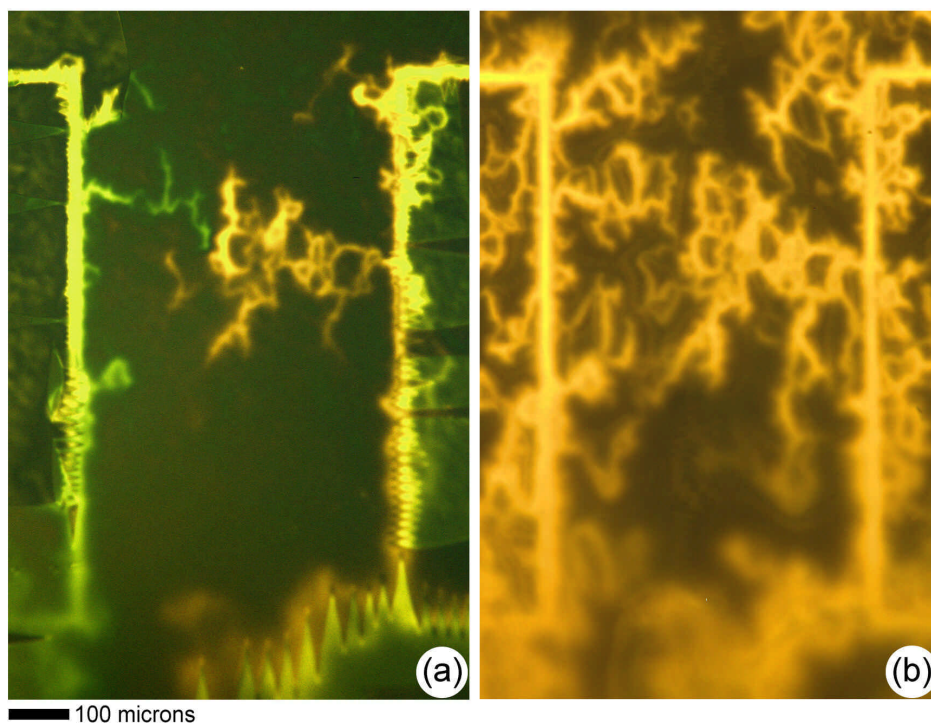


Figure 3.11. MO images of F197CN1. (a). MO image of the self-field of the link at an applied current of I_c . $I_c = 1.0$ A for the link and $J_c = 0.6$ MA/cm². (b). MO image under magnetization currents. For this image, the sample was ZFC to 40 K and then a field of 20 mT was applied. Same as Figure 3.10(b).

Figure 3.11(a) is also a clear demonstration of current percolation. If the direction of current flow is from the bottom to the top of image, then the ‘green flux’ is coming out of the page, and the ‘yellow flux’ is going into the page. The fact that the yellow flux extends from the right side of the link to more than half way across means that more current is flowing on the left-hand side of the link in the neighborhood of the large GB cluster. Also, the yellow and green flux start at their respective sides and extend slightly past each other. From this it can be deduced that at least a portion of the current follows the solid white line in Figure 3.12. A fraction of the current also crosses the visible GBs in the image (dashed white lines), but again it is not possible to quantitatively determine that fraction.

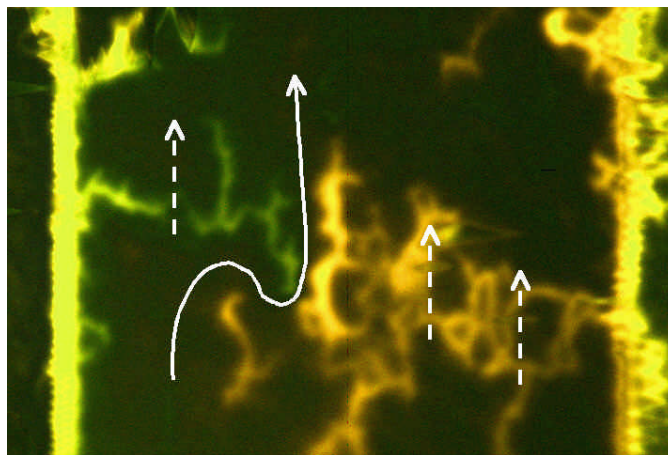
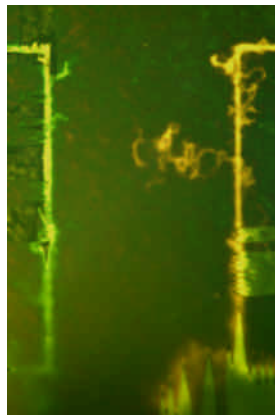
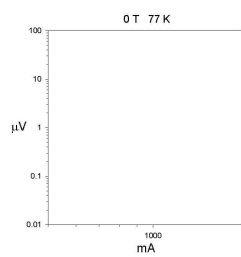


Figure 3.12. A subset of image 3.11(a) showing that at least a portion of the current “doubles back” on itself as it percolates through the visible GBs in the image.

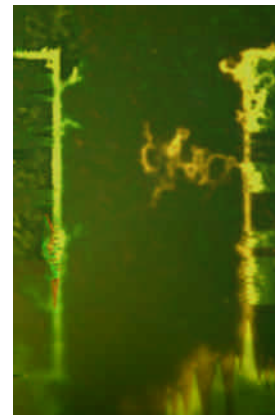
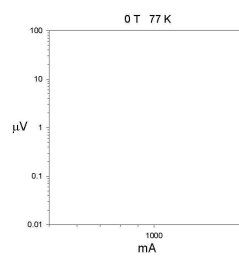
A series of MO images of the self-field of the link are shown in Figures 3.13. These images are coupled with voltage-current data, where the voltage has been

measured across the entire link as shown in Figure 3.9(a). For 3.13(a), the sample was cooled to 77 K in the absence of an applied field, and then a transport current of 600 mA was applied. For Figures 3.11(b)-(j), images were taken at increasingly higher applied currents. The coupled voltage-current (V-I) data was taken simultaneously with the MO images. This montage shows a gradual change in the self-field of the link as the applied current is increased. This is in contrast to the voltage drop across the link (and hence the electric field) which is changing dramatically. The gradual change in the MO images is especially noteworthy in moving from the non-dissipating to the dissipative regime [Figures 3.13(d)-(f)]. There is no way to judge I_c from looking at the MO images alone. There are no GBs suddenly becoming visible at the onset of dissipation, and there are a great many GBs visible at currents less than I_c . This means that current is percolating in the conductor from well before the onset of dissipation to well after. It is clear that the dissipation does not occur uniformly throughout the link, and that only a portion of the link is dissipating. The visible GBs in Figures 3.13 can provide insight into where the dissipation is occurring in the link, but just because a GB is visible does not mean there is dissipation occurring at that GB, so the location of the equipotential lines are not clear.

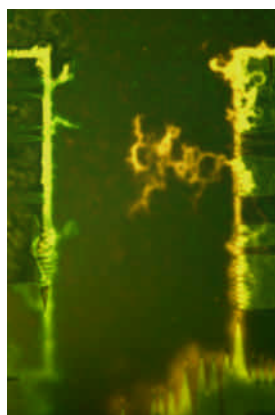
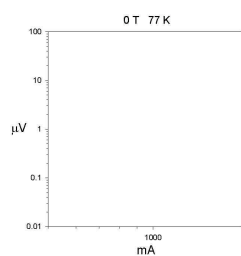
(a)

600 mA
 $0.6 J_c$ 

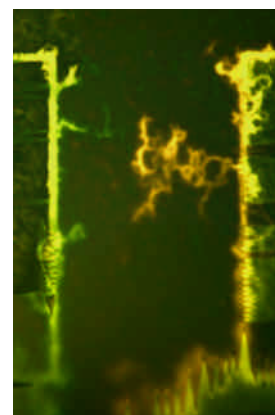
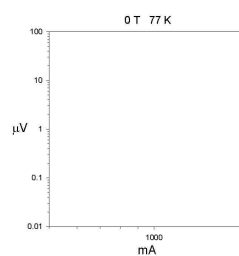
(b)

700 mA
 $0.7 J_c$ 

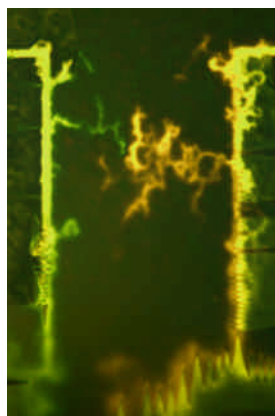
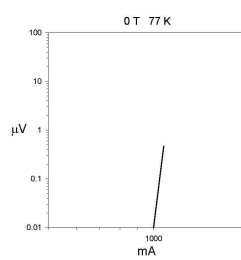
(c)

800 mA
 $0.8 J_c$ 

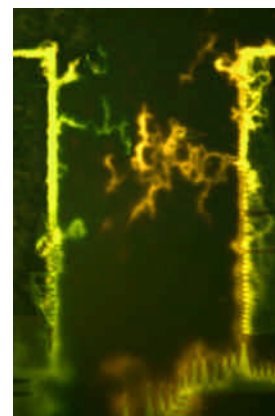
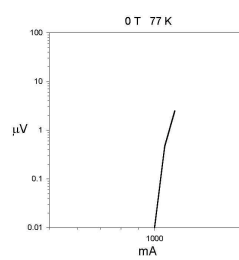
(d)

900 mA
 $0.9 J_c$ 

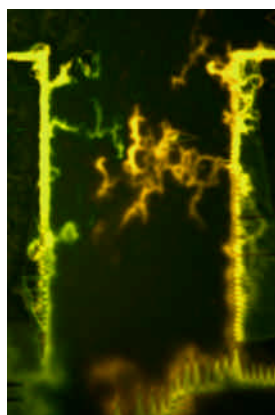
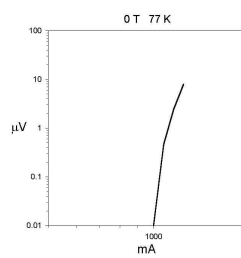
(e)

1.0 A
 $1.0 J_c$ 

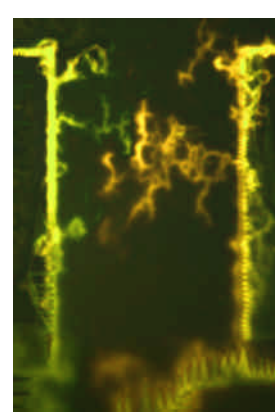
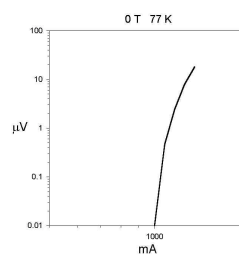
(f)

1.1 A
 $1.1 J_c$ 

(g)

1.2 A
 $1.2 J_c$ 

(h)

1.3 A
 $1.3 J_c$ 

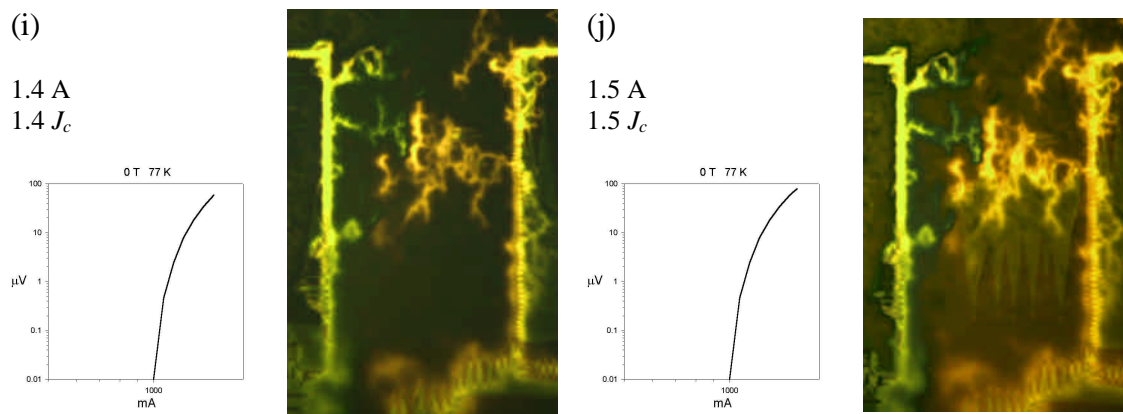


Figure 3.13. MO images of F197CN1 under an applied transport current coupled with V-I plots. For all MO images the sample was ZFC, a transport current was applied, and the voltage measured simultaneously. There was no externally applied magnetic field. The series of images (a)-(j) show the simultaneous evolution of the voltage drop across the link with change in self-field.

Extended voltage-current characteristics (up to 1 T) of the link are shown in Figure 3.14(a). Examples of pure inter and intra-grain V-I behavior from a \mathcal{P} YBCO bicrystal are shown in Figures 3.14(b) and (c) respectively, and are presented for comparison to the V-I traces of the laser-scribed link. The traces of the link are very curved, resembling neither single crystal nor GB behavior. Intra-grain traces are generally very straight, and while GB traces often have a pronounced “knee” at higher voltages, they generally have a steep initial rise. Of course, the V-I plot of the link is the result of dissipation occurring at several GBs and possibly isolated intra-grain regions, so it is not expected that its V-I behavior resemble pure inter or intra-grain. The V-I traces of this link are much more curved than the traces from the link of sample F159CN2 [Figure 3.5(a)]. This may be due to a smaller fraction of the dissipation occurring in the intra-grain, a greater number of high angle GBs, or simply a greater number of

boundaries. More work needs to be done to associate V-I *behavior* with GB geometries and MO imaging.

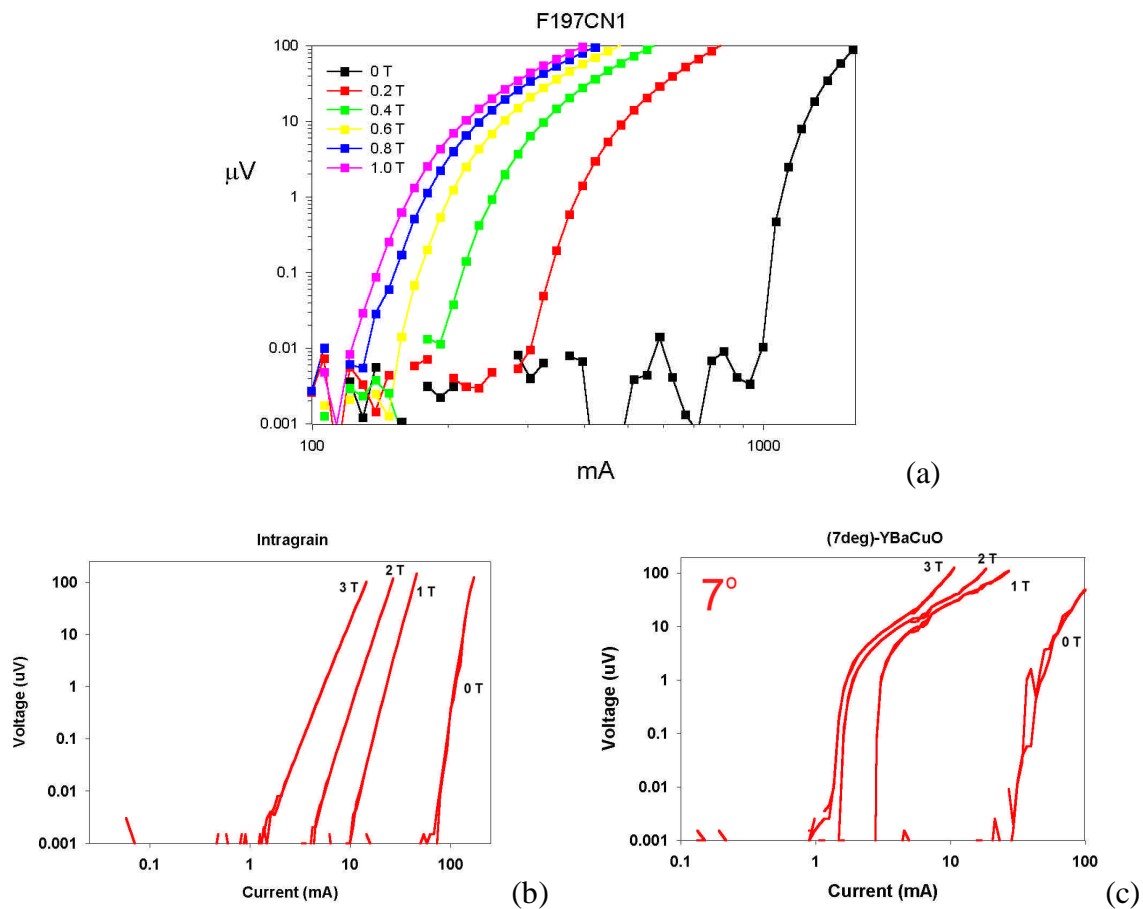
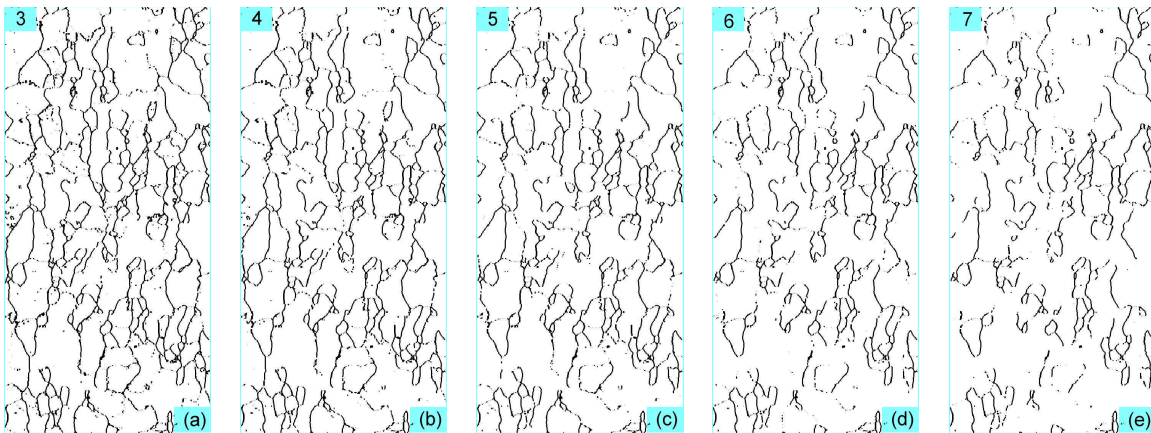


Figure 3.14. Voltage-current characteristics of the link of sample F197CN1 and inter and intra-grain plots taken from a 7° YBCO STO bicrystal. (a). V-I plot of the link of F197CN1. Traces are 0 to 1 T in steps of 0.2 T. (b) Example of typical intra-grain V-I behavior. Traces are very straight. 0, 1, 2, and 3 T traces plotted. (c) Example of typical GB behavior, in this case 7° . Traces rise steeply with a pronounced “knee” at higher voltages. 0, 1, 2, and 3 T traces plotted.

Orientation mapping was performed on the YBCO, the YSZ, and the Ni in the link area. Because of the difficulty in obtaining orientation data on the YBCO and YSZ, only about 25% of the link was mapped in these layers. Orientation mapping can be

performed much more easily on Ni, and orientation data over the entire area of the link was obtainable off of the Ni substrate. The orientation data from the YBCO and YSZ layers was used in the texture development analysis of Chapter Two. Figures 3.15 show the transport MO image, the magnetization image, and a series of GB maps all at the same scale. The poorer texture of the Ni is evident from the number of high angle GBs present in Figs 3.15(a)-(l), and is certainly consistent with number of visible GBs in Figure 3.15(m). As done previously, the GB maps [Figs. 3.15(a)-(l)] and the magnetization MO image [Fig. 3.15(m)] can be compared to determine a critical angle, q_c . The best fit between the GB maps and those GBs appearing in the magnetization MO image again appears to be $\sim 5^\circ$ [Fig. 3.15(c)]. However, there are so few GBs below 5° [See Figs 3.15 (a)-(c)] that it is difficult to determine q_c precisely.



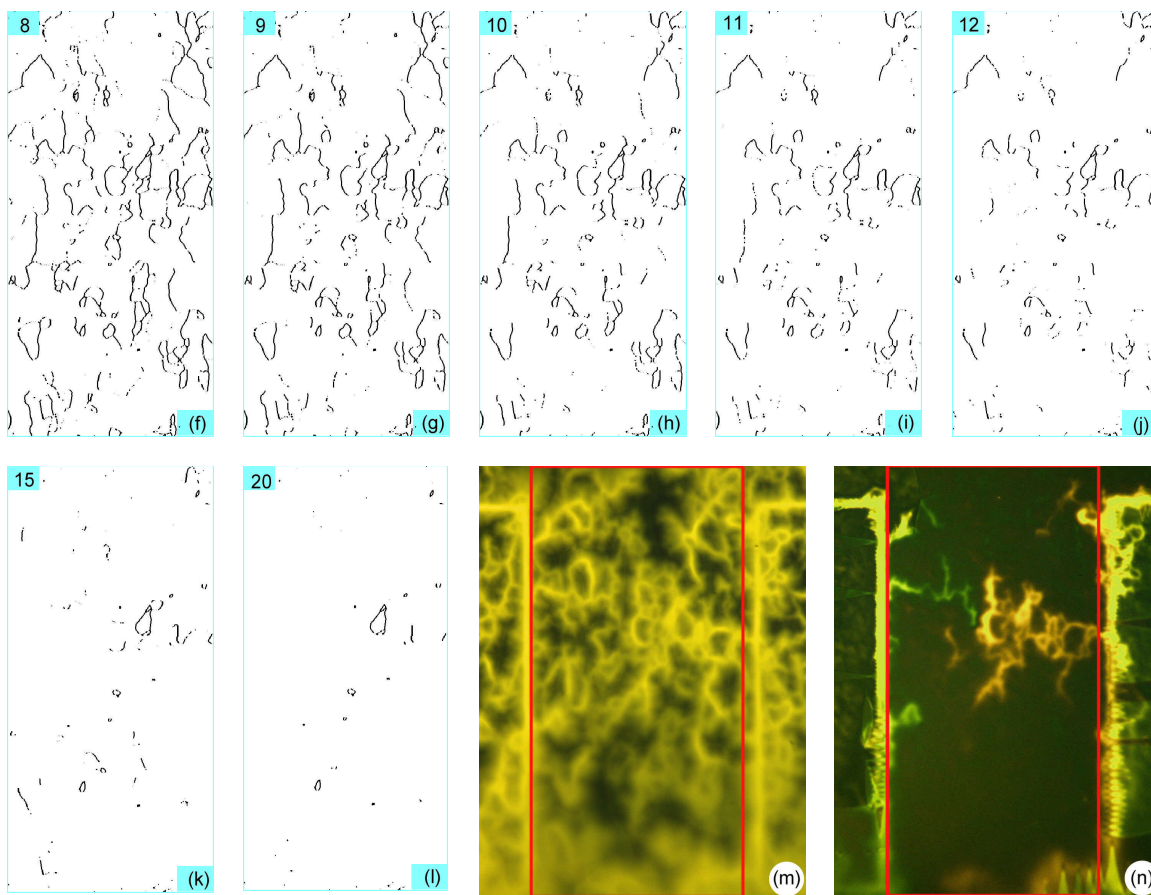


Figure 3.15. GB maps taken off the underlying Ni substrates for comparison to the magnetization and transport current MO images. (a)-(l) Maps of all GBs with misorientation angles greater than or equal to the number in the upper left hand corner. (m) MO image in the presence of magnetization currents. For this image, the sample was ZFC to 40K, and then a field of 60 mT was applied. The red rectangle marks the approximate location of the GB data in (a)-(l). (n) MO image of the self-field of the link at J_c (77 K, 0 T). The red rectangle marks the approximate location of the GB data in (a)-(l).

Upon comparing the GBs maps of Figure 3.15 to the MO image of self-field [Figure 3.15(n)], initial impressions may be that there is little correlation between misorientation angle and those GBs visible in Figure 3.15(n). A more detailed analysis is required to understand the correlation. Figure 3.16 presents a grain orientation map from the Ni substrate next to the MO image of self-field (at I_c) for comparison. The grain orientation map, or Euler angle map [Fig. 3.16(a)], colors the grains according to their

orientation relative to the sample reference frame. The exact orientation is not important here. The letter “A” in Figure 3.16(a) indicates one highly misoriented grain. This grain had its *c*-axis off by $\sim 55^\circ$ from normal. Consequently the grain is surrounded by very high angle GBs [see Fig. 3.15(l)] and the YBCO above this grain grew with a very low J_c , if superconducting at all. The grain in question can be seen in Figure 3.16(b), and is almost completely penetrated by magnetic flux. In Figure 3.10(a) the grain in question appears darker than the surrounding grains, and in the magnetization MO images of Figures 3.10(a) and (b) it can be seen to be completely penetrated with flux. The relevance of this observation to the self-field image is that grain “A” reduces the cross section of the link available to current flow. This has the effect of increasing the current density, J , in the area around the grain relative to the rest of the link. Also highlighted in Figure 3.16(a) are several high angle GBs ($\geq 12^\circ$) running roughly perpendicular to the general direction of current flow. GBs $\geq 12^\circ$ will usually have J_c values $< 0.1 \text{ MA/cm}^2$ and will act as effective current barriers. Considering both grain “A” and the high angle GBs, the effective cross section of the link in the vicinity of these objects is reduced to $\sim 66\%$ of the link width, and is indicated by the shaded area (gray) in Figure 3.16(a). This reduction in the cross section does not even consider GBs of angles lower than 12° , nor does it consider GBs that run mostly parallel to the link, which may also hinder current flow or reduce the opportunity for current to find a higher- J_c path. Since the cross section is reduced, J in this region will be higher and GBs of a given angle will be more likely to be visible in this region than in other areas of the link. This effectively explains why the GB maps of Figure 3.15 do not exhibit a stronger correlation with the self-field image,

and also demonstrates that the geometry of GBs in a CC can play just as large a role as misorientation angle.

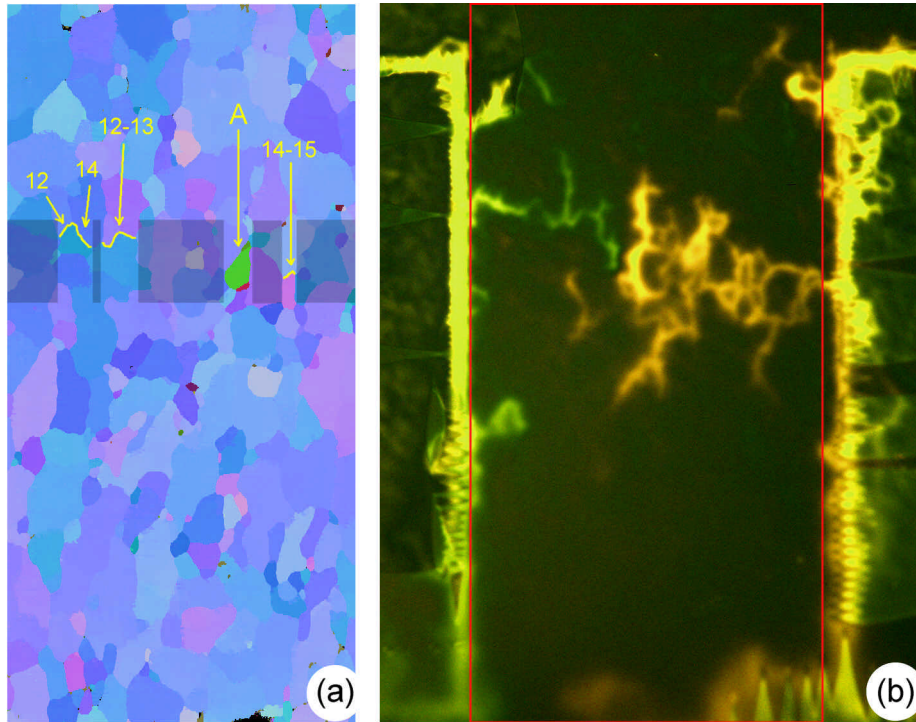


Figure 3.16. Orientation (Euler angle) map and self-field image of the link in sample F197CN1. (a) Orientation (Euler angle) map. The grains are colored according to their orientation. One grain, labeled with a letter “A”, has its c -axis off by 55° from normal. Several high angle GBs are identified in yellow. The shaded area (gray) shows the remaining cross section available to current. (b) MO image of the self field at I_c (1.0 A) and 77 K. No externally applied magnetic field. Same as Figs. 3.11(a), 3.12(e), and 3.13(n). The red rectangle marks the approximate location of the orientation map in (a).

In this sample the J_c of the link was again limited in a portion of the track, just as in the link of sample F159CN2. Figures 3.15(m) and (n) are MO images of link in the critical state (magnetization image) and at its critical current (self-field) respectively. Comparison of these images shows that the vast majority of the link is *not* in the critical state at I_c . Simultaneous measurement of voltage-current characteristics with MO

imaging demonstrated that current is percolating from well before the onset of dissipation to well after. Current flow is never a good approximation to single-crystal current flow.

3.3.3 Transport currents in TFA1455

Sample TFA1455 was from a different source, American Superconductor Corporation (AMSC). The buffer layer architecture was similar to that of the ORNL samples, but the Ni substrate was thicker and the grain size was larger on average. The YBCO layer was grown by the TFA process and was a little thicker at 380 nm. The size of the link cut in this sample was very close to the link of F197CN1 at 0.50 x 1.1 mm. A surface image of the sample with the MO indicator film in place is shown in Figure 3.17(a). Figure 3.17(b) is a schematic identifying the current and voltage pads, and the location of the laser cuts. The link had a J_c of 1.3 MA/cm², and J_c of the sample at full-width was 0.81 MA/cm².

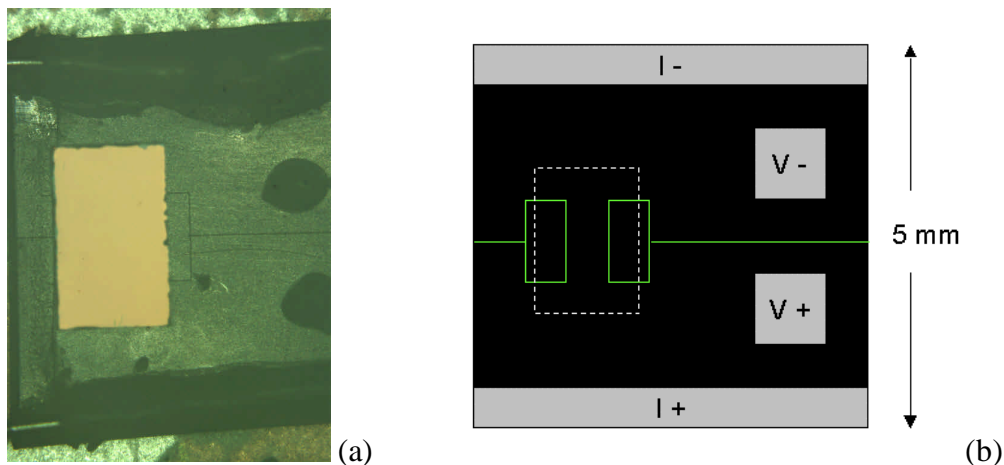


Figure 3.17. Surface image and diagram of TFA1455. (a) Surface image of TFA1455 showing a small piece of indicator film placed over the laser-defined track. (b). Schematic of the sample identifying voltage and current pads. Laser cuts are shown in green, and the dashed line indicates the approximate location of the indicator film.

Extended V-I data was taken on the link and is shown in Figure 3.18. For a link with roughly the same dimensions as that of F197CN1, the V-I traces look very different. The traces of Figure 3.14(a) are very curved, but the traces in Figure 3.18 are straighter, resembling intra-grain traces or traces of a low angle GB ($\sim 3^\circ$). This suggests that a greater fraction of the dissipation is occurring in the intra-grain (relative to the link of F197CN1) or the GBs that are dissipating are of smaller q , or both. The differences in the V-I behavior seen in Figures 3.14(a) and 3.18 do seem consistent with their respective J_c 's of 0.6 and 1.3 MA/cm².

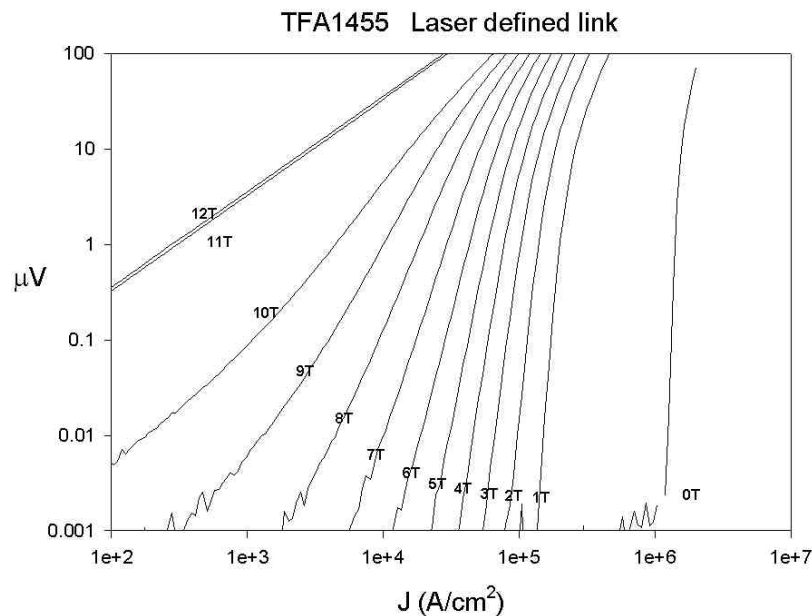


Figure 3.18. Extended voltage-current (V-I) data from the link scribed in TFA1455. The $1 \mu\text{V}/\text{cm}$ ($0.11 \mu\text{V}$ for this link) J_c criterion yields a J_c value of $1.3 \text{ MA}/\text{cm}^2$. The V-I traces fit well with those of a 0° (intra-grain) to 3° GB.

Magneto-optical images of the link are shown in Figures 3.19. Figure 3.19(a) shows the self-field of the link at I_c , which was $\sim 2.4 \text{ A}$. At I_c , the visible GBs are a little more spread out than in the previous two links, though the dissipation does appear to be isolated in the region indicated by the arrows. The larger grain size of the Ni is also evident. Figures 3.19(b) and (c) are ZFC magnetization images at 10 and 30 mT respectively. The 10 mT image looks very much like the image of self-field, with just a few additional GBs appearing. 30 mT was sufficient to put the sample in the critical state, and it can be seen again that most GBs have a J_c less than that of the intra-grain. There are many more GBs appearing in Figure 3.19(c) than in the self-field image of Figure 3.19(a), yet all the visible GBs in Figure 3.19(c) have a J_c less than that of the local intra-grain. This is a very important observation in understanding what limits J_c in these conductors. From Figure 3.19(a), the dissipation in the link is occurring at only a small subset of existing GBs. This observation puts a strong emphasis on maintaining good local, grain-to-grain alignment. Knowing that J_c in a deformation textured CC will always be limited by a subset of existing GBs means that global measures of grain alignment, such as x-ray diffraction measurements, are not sufficient means to gauge the performance of a tape. Recent experiments with IBAD YSZ and MgO tapes have shown that even when the FWHM values (as determined by x-ray pole figures) of the two types of tape are the same, the IBAD MgO tape has a reduced current density due to a poorer grain-to-grain alignment [48]

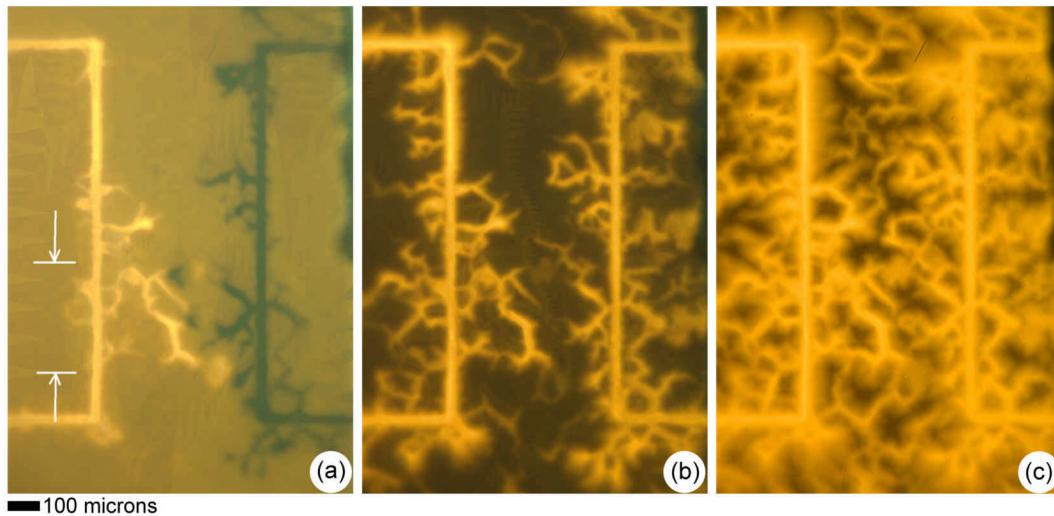
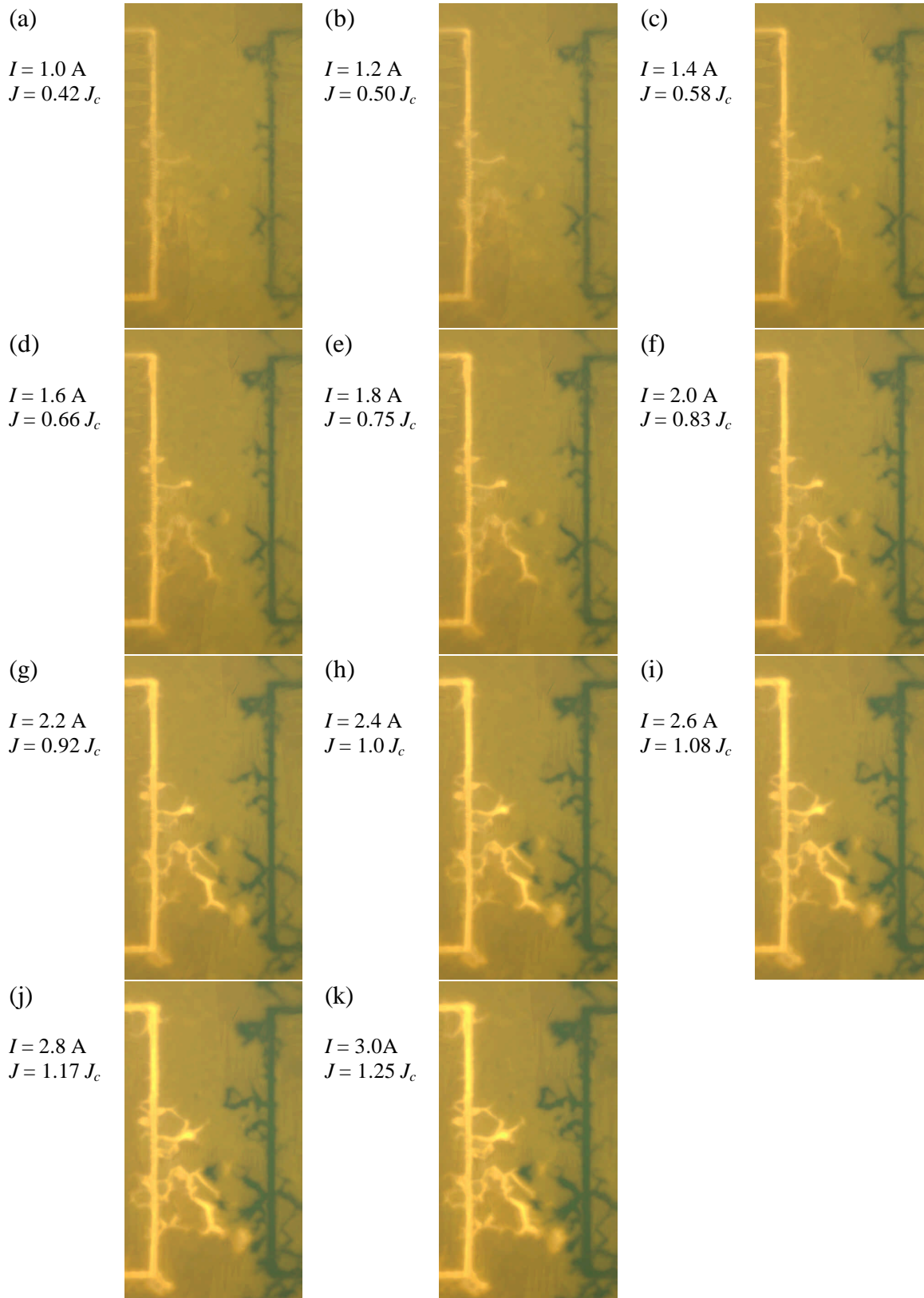


Figure 3.19. MO images of TFA1455 in the presence of magnetization and transport currents. All images are at 77K. (a) MO image of the the self-field of the link at an applied current of 2.4 A, which was roughly I_c . Here, yellow and dark green are field into and out of the page, and the natural light-brown color of the MO indicator film represents zero field. (b) For this image, the sample was ZFC to 77K and then a field of 10 mT was applied. (c) The sample was ZFC to 77 K and then a field of 30 mT was applied. At 77 K 30 mT was sufficient to put the sample in the critical state.

Figures 3.20 are a series of MO images of self-field at increasingly higher applied currents. The series only goes up to 3.0 A and I_c was ~ 2.4 A, so a larger fraction of “pre-dissipation” images are represented here than in the other links. Once again, percolation is occurring before and after the onset of dissipation, with a very gradual change in the self-field. This appears to be a general feature of transport current flow through systems of GBs. Orientation mapping was also done on the Ni substrate of this link, and a series of GB maps were produced (not shown). The results were similar to the previous two links, with a q_c (as measured on the Ni) of $\sim 5^\circ$, and no strong correlation between the GB maps and the MO images of self-field.



Figures 3.20. A series of MO images of the self-field of the link at increasingly higher applied currents. All images are at 77 K.

3.2 Conclusions

The results of the transport studies of this chapter should remove any lingering doubts about the influence of GBs on current flow. GBs are the most significant current limiting mechanism in deformation textured CCs, even in samples with the highest J_c values. In all three samples studied in this chapter, coupling the $J_c(0\text{ T}, 77\text{ K})$ measurement with MO imaging of the self-field has shown that the dissipation is localized at a small number of existing GBs, and the majority of the sample is carrying a current much less than its local J_c . The V-I traces of Figures 3.17, 3.13(a) and 3.5(a), when compared to the single crystal and pure GB traces of 3.13(b) and (c), also nicely demonstrate the varying degrees of GB influence in the links. The direct coupling of V-I behavior to self-field in Figure 3.12 demonstrated that the current flow is changing slowly from before the onset of dissipation to well after. This adds significantly to our understanding of percolation in CCs, and dispels many ‘myths’, such as GBs suddenly ‘lighting up’ in the MO images at the onset of dissipation, or current flowing uniformly until the onset of dissipation, and only percolating after (or vice versa).

This is the first work to magneto-optically image CCs under an applied transport current, and the first work to definitively demonstrate percolative (transport) current

flow. Chapter 2 demonstrated the percolative nature of *magnetization* currents in CCs, but that work was met with much resistance and criticism (especially by those who made the samples) because it opposed the idea uniform current flow. However, the demonstration of percolation provided by the coupling of voltage-current behavior with MO imaging of the self-field is inarguable. The similarity between magnetization and transport MO images also validates *magnetization* MO imaging as a method of identifying *transport* current limiting regions. This work also places a strong emphasis on good *local* texture in obtaining high J_c values. Emphasis on the local texture is important because as recent studies of IBAD MgO tapes demonstrate x-ray diffraction measurements (a *global* measure of grain alignment) may not correlate well with grain-to-grain alignment [48].

One shortcoming of the work in this chapter is that it only provides a qualitative analysis of current flow. While the J_c and the voltage-current characteristics of the laser-scribed links have been well quantified, the MO imaging provides only a qualitative look at the current flow within the link. One method of taking a quantitative look at the local current flow is the method of *current reconstruction* [49]. If the magnetic field above the link is measured quantitatively, the Biot-Savart law can be ‘inverted’ to determine the local current flow. Considerable effort was expended in developing an algorithm for this task, and this is discussed in Appendix C. However, a current reconstruction could not be performed with any of the samples in this chapter because of the magnetic substrates. With a Ni substrate, the field measured above the CC sample is not a result of the current alone but of the current and the response from the Ni, and a current reconstruction could not be performed accurately. Samples with non-magnetic substrates had been obtained

for the purpose of current reconstruction, but they were of very poor quality. Another way to investigate the inter and intra-grain J_c in CCs is with direct transport measurements. In the next chapter, results are presented from a series of links placed across individual Ni GBs and within individual Ni grains in several CC samples. This does not provide a direct view of the percolative nature of current flow, as the studies of this chapter or a current reconstruction would. However, it does provide a very accurate measure of the inter and intra-grain J_c , and these results add further validity and insight to results already discussed.

4 Inter and intra-grain transport measurements

Magneto-optical imaging permits a qualitative analysis of current flow and statements about the ratio of J_{cb}/J_{cg} . It is not possible to use MO imaging to quantitatively determine either J_{cb} or J_{cg} alone. In interpreting the MO images in this thesis, the $J_c(\mathbf{q})$ dependence derived from STO bicrystal studies (Figure 1.2) was often referenced. However, the $J_c(\mathbf{q})$ dependence of CC GBs was not previously known nor was it immediately obvious that it should be the same as that found for STO bicrystals. Also, the intra-grain J_c in CCs was unknown, and it was not clear that YBCO could be grown on a metal substrate with a complex buffer layer architecture and attain the same quality as YBCO grown on single crystal substrates. The intra-grain J_c has important consequences for \mathbf{q}_c in these conductors and also sets the upper limit to full-width J_c values. Typical inter and intra-grain V-I traces from STO bicrystals were used for comparison with the V-I traces of the magneto-optically imaged links in the last Chapter as well. This too assumed certain similarities between CC and bicrystal GBs. In this Chapter, the intra-grain J_c , the $J_c(\mathbf{q})$ dependence, and the V-I behavior of inter and intra-grain regions in CCs is investigated.

4.1 Experimental

Optical photolithography and dry etching were used to place links across individual Ni GBs and within individual Ni grains in several CC samples. Most CC samples that were patterned were first measured for J_c at full width (3-5 mm) and had voltage taps ~4 mm apart. In order to characterize the same portion of the tape that was measured at full-width, a structure was patterned to fit these dimensions. This structure is shown in Figure 4.1, with five contact pads (two for current, three for voltage) and two links ~10 μm wide and 30 μm long. An optical mask was made with this structure, and photolithography was performed as described in Figure 4.2. The size of the link was chosen to easily fit inside the Ni grains, whose average size was ~50 μm . The GBs in a CC sample can be very difficult to see with a light microscope, and at first the mask was placed ‘blindly’ on the sample, resulting in some pure inter and intra-grain links, but many links had multiple GBs or complicated GB geometries. Eventually a technique was developed that allowed for much more accurate placement of the links in the CC, but this advancement came late in the experiment. After patterning, Au was sputtered for electrical contacts. An example of a finished product is shown in Figure 4.3.

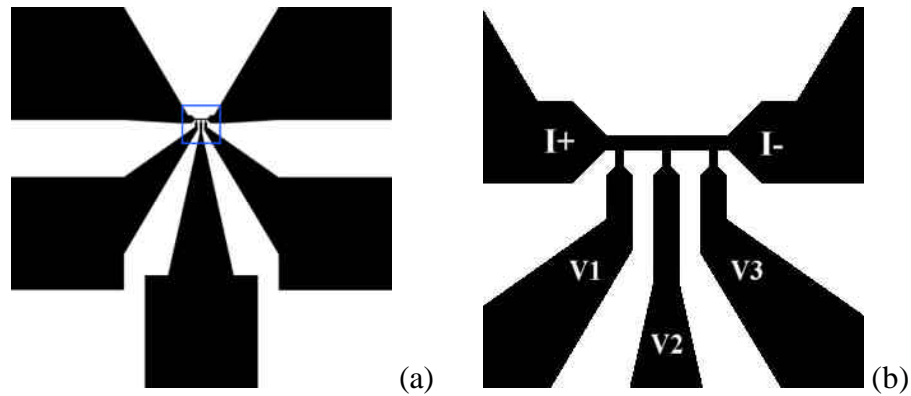


Figure 4.1. Images of the structure that was placed on several samples for the inter and intra-grain study. An optical mask was created with this structure in order to perform patterning as described in Figure 4.2. (a) Entire pattern showing five pads for electrical contact, and the measurement area in the center. Pattern is 3 x 3 mm. (b) Close-up of the measurement region, indicated by the blue box in (a). Each link is 30 μm long and 10 μm wide. Current and voltage taps are highlighted.

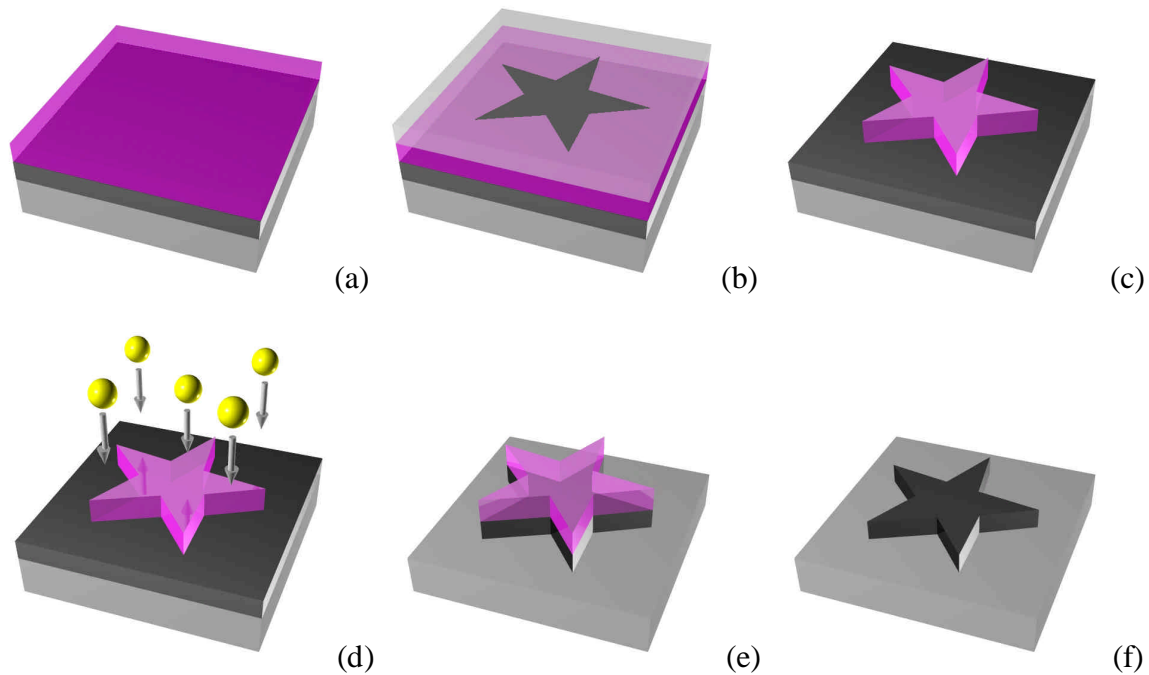


Figure 4.2. Steps taken to pattern a sample. (a) A layer of photoresist (pink) is deposited on top of the YBCO (black) and the substrate (gray). (b) An optical mask (a glass slide with the desired structure) is placed on top of the photoresist and the photoresist is exposed with ultra-violet light. (c) After developer and a rinse, the desired structure is left. (d) Dry etching is performed. The photoresist protects the YBCO from ion milling (Ar ions). (e) The unwanted YBCO is milled away, effectively transferring the pattern to the YBCO. (f) The remaining photoresist is removed with acetone.

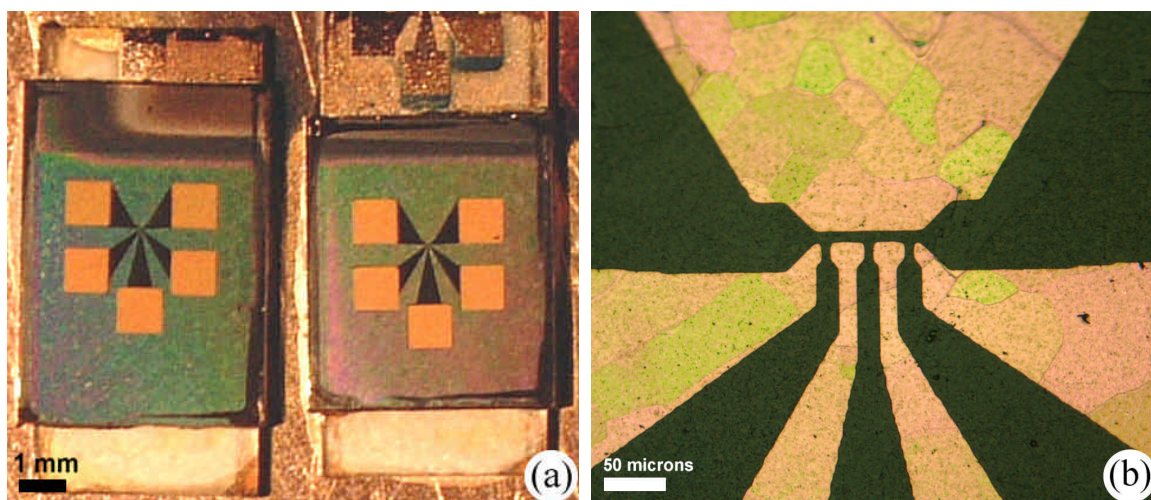


Figure 4.3. Image of some final products, after patterning and Au deposition. (a) The CC samples were mounted to sapphire chip carriers for handling purposes. The red-green-blue colored regions are the exposed buffer layers where the YBCO has been removed. (b) Higher magnification image of the link region. This image shows both links in the same Ni grain.

Extended V-I characteristics and $J_c(H)$ dependencies were measured for all links. Transport current was applied using a Kiethley 2420 3A source-meter. LabVIEW programs were written for data collection, and also allowed for remote control and observation. Early in the experiment, measurements were carried out in an electromagnet and voltage measurements were made with a HP 34410A nano-voltmeter. The electromagnet did not permit fields greater than 1 T, and the nano-voltmeter had a typical measurement noise of just under 10 nV. Later the experiment was moved to an OXFORD cryostat with a superconducting 13/15 T magnet. Voltage measurements were then performed with a Keithley 1801 nano-volt pre-amp, and a new rig was constructed. The new rig used gold plated pogo-pins to make contact with the sample, and allowed for bare Cu on Cu connections all the way from the pre-amp to the pogo pins. This vastly

improved voltage noise from ~ 10 nV to 0.3-0.5 nV. Images of a sample mounted in the later rig are shown in Figure 4.4. All J_c values were determined using an electric field criterion of $1 \mu\text{V}/\text{cm}$. For a link $30 \mu\text{m}$ long, this yields a voltage criterion of 3 nV, well above the later measurement noise. For all measurements, the sample was immersed in liquid nitrogen (77.25 K).

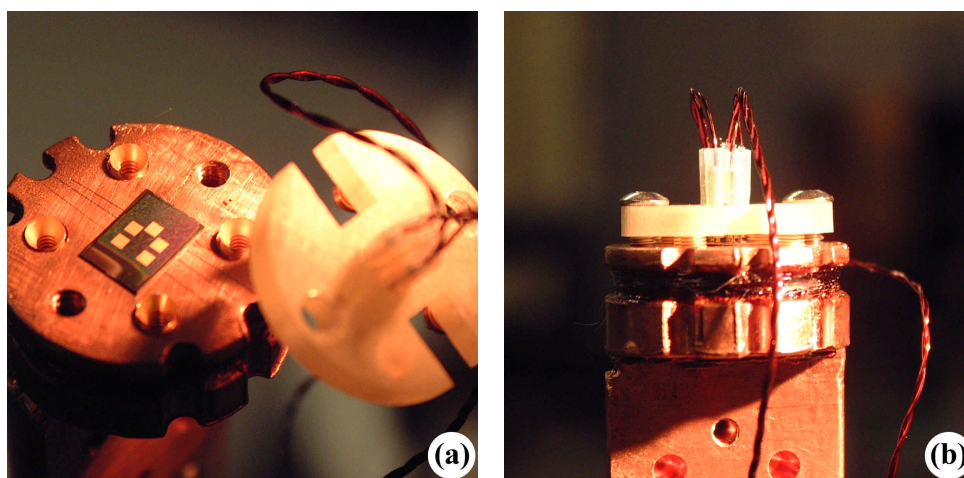


Figure 4.4. Images of the measurement rig. (a) Sample mounted in the rig, before the pogo-pin head is put into position. (b) Rig, with pogo-pin head in place, and pogo-pins in contact with the Au pads of the sample seen in (a). After the sample is mounted, the rig is inverted and placed in liquid nitrogen in the cryostat/magnet.

In order to determine the $J_c(\mathbf{q})$ dependence for CCs, it is necessary to measure the \mathbf{q} of the inter-grain links. For this EBKP analysis was used. As discussed in Chapter Two, it is difficult to obtain EBKP data directly on YBCO. In this study, it was only possible to obtain orientation data from the YBCO for one inter-grain link. For the remaining inter-grain links, the angles were measured as close to the link as possible in the YSZ buffer layer, which had been exposed during patterning. As the plot of Figure

2.8(a) suggests, \mathbf{q} in the YBCO may be lower by 0.5 - 2.0 degrees. The error introduced by measuring the misorientation in the YSZ is unfortunate, but it will be seen that it does not prevent a good determination of the $J_c(\mathbf{q})$ dependence.

4.2. Results and discussion

Table I lists properties of some of the samples and patterned links in this study. Those links with multiple GBs or complex GB geometries are excluded from the list. These samples came from two different sources, with YBCO deposited by either the BaF₂ [38] or TFA [39] methods. All samples had a Ni/CeO₂ or Y₂O₃/YSZ/CeO₂/YBCO architecture. Figure 4.5 is a scanning electron microscope (SEM) image of the pair of links patterned in sample #3. In this case both links are within the same Ni grain. Figures 4.6(a) and (b) are V-I traces of the left and right link of Figure 4.5 respectively. Despite both links being in the same Ni grain, the J_c value of the left link was 1.3 MA/cm², and the J_c of the right link exceeded 3.5 MA/cm². The J_c of the left link was limited by a large *a-axis* grain, highlighted in Figure 4.7, which extends more than half way across the link. Such *a-axis* grains are rare, but do detrimentally effect J_c . The two intra-grain links of sample #4 were also within the same Ni grain. There is a 20% difference in the J_c of these two links, but an SEM investigation revealed no reason for the difference. These are two demonstrations of J_c varying within a single Ni grain, but such variations exist in YBCO grown on single crystal substrates as well. All the intra-grain links (excluding the one limited by the *a-axis* grain) had a very high J_c .

Sample #	YBCO thickness (nm)	Full-width (mm)	Full-width J_c 10^6 A/cm ²	θ /intra-grain	Link $J_c(0$ T) 10^6 A/cm ²	Link $J_c(1$ T) 10^6 A/cm ²
1	310	3.3	1.26	intra	5.1	0.62
2	300	3.3	0.85	2.8°	3.0	0.39
3	380	5	N/A	intra	>3.5	0.41
				intra(<i>a-axis grain</i>)	1.3	0.97
4	380	5	N/A	intra	3.8	0.20
				intra	3.1	0.22
5	380	5	0.9	7.1°	0.7	0.06
				intra	N/A	0.23
				5.5°	0.8	0.07
6	380	5	0.8	9.8°	0.4	N/A
				2.9°	2.6	N/A

TABLE I. Comparison of some of the inter and intra-grain links pattern in several different coated conductor samples. Links with multiple GBs or complex GB geometries are excluded from the table. All J_c values are at 77 K and were determined using a 1 μ V/cm electric field criterion. Samples #1-2 came from Oak Ridge National Laboratory and the YBCO was grown by the BaF2 method. Samples #3-6 came from American Superconductor and the YBCO was grown by the TFA method.

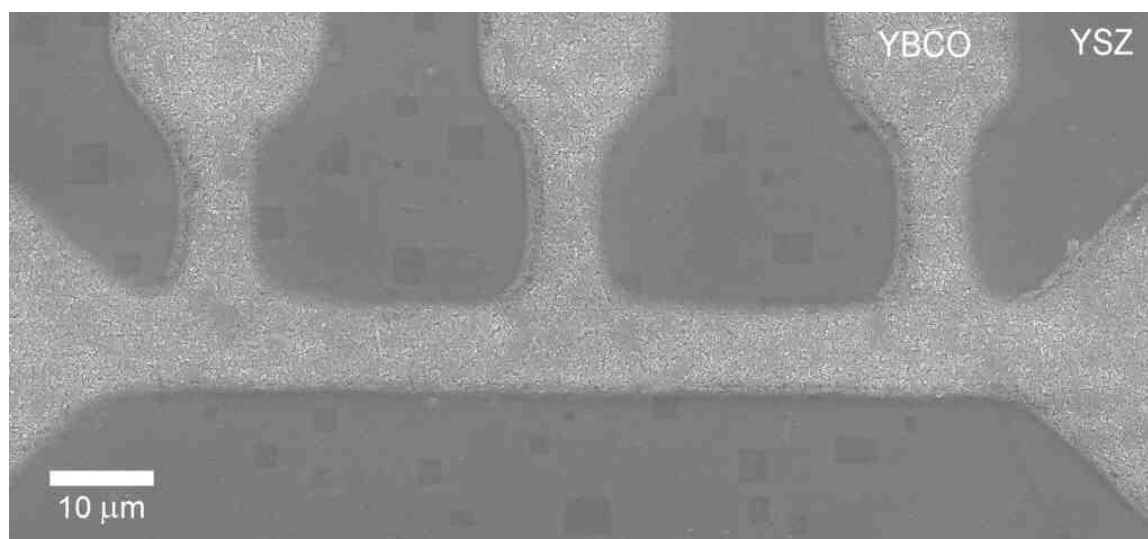


Figure 4.5. SEM image of the two links patterned in sample #3 of Table I. The GBs can be difficult to see in plan-view SEM, but both links are within the same Ni grain. The links are horizontal with three voltage taps across the top allowing for true four point measurements of both links.

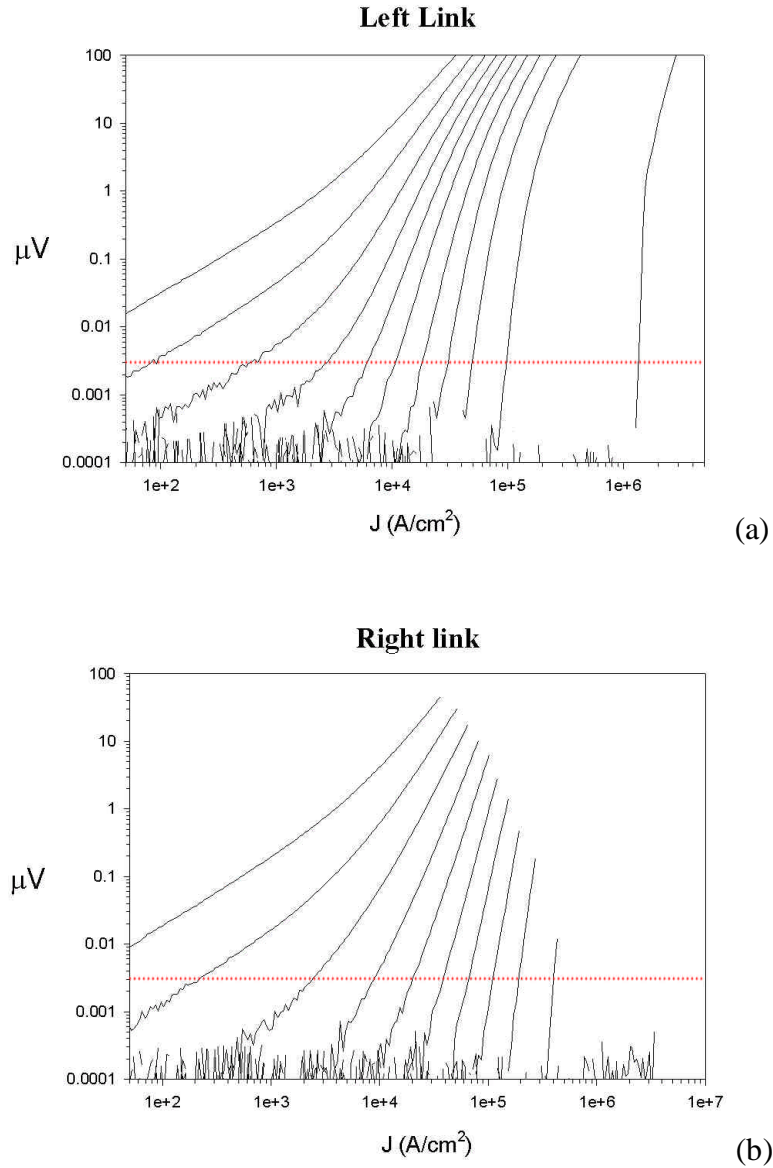


Figure 4.6. V-I traces of the two links in Figure 4.5. The traces are from 0 to 10 T in increments of 1 T. Six decades of voltage are shown, from 0.1 nV to 100 μV . The dashed red line indicates the 1 $\mu\text{V}/\text{cm}$ J_c criterion (3 nV). (a) Left link of Figure 4.5. (b) Right link. This current in this link was limited by the left link, and the zero field trace does not reach the 1 $\mu\text{V}/\text{cm}$ J_c criterion.

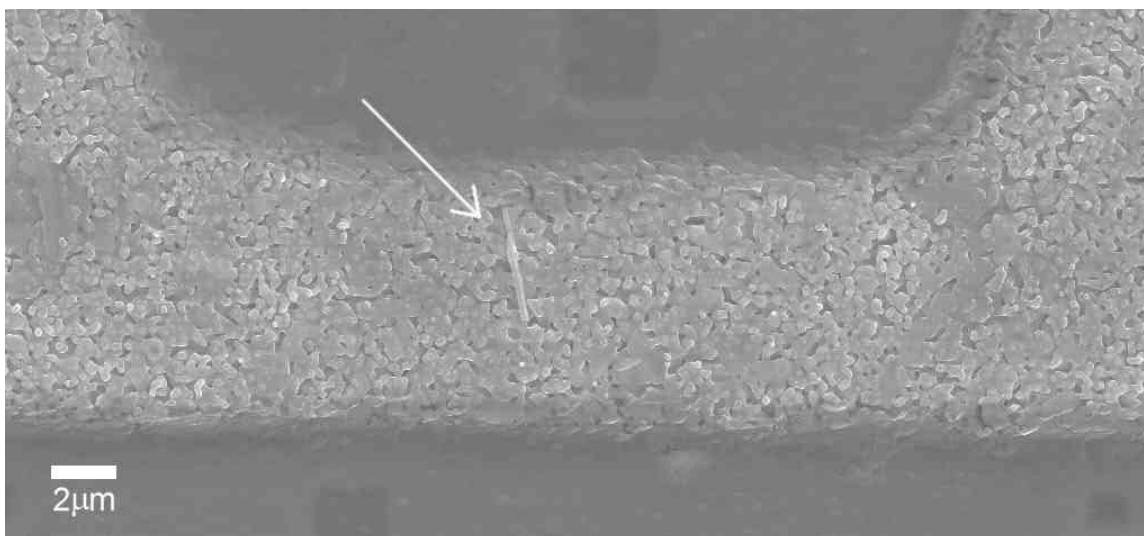


Figure 4.7. An SEM image providing a closer look at the left link of Figure 4.5. A white arrow indicates a large *a-axis* grain that extends more than half way across the link. The *a-axis* grain is responsible for the reduced J_c relative to the right link.

Figure 4.8(a) shows an SEM image of the 7.1° inter-grain link of sample #5, and an adjacent intra-grain link. The GBs in the SEM image can be difficult to see, but the EBKP map of Figure 4.8(b) clearly shows the locations of the Ni grains. This orientation data was taken off the YSZ buffer layer, and was used to determine the \mathbf{q} of 7.1° for the inter-grain link. V-I traces of the inter and intra-grain link are shown in Figures 4.9(b) and (a) respectively. The current of the intra-grain link was limited by the inter-grain link, and a zero-field J_c could not be determined. Inter and intra-grain V-I traces from a 7° STO bicrystal are shown in Figures 4.9(c) and (d) for comparison. The general V-I behavior of the inter and intra-grain links from sample #5 is not unlike those obtained from the STO bicrystal. While the intra-grain traces of Figure 4.9(a) are incomplete, they are straight and relatively evenly spaced with applied field, just as the traces of Figures

4.9(c) and 4.6(b). For the 7.1° link [Figure 4.9(b)], the traces exhibit a ‘knee’ at higher voltages, and the in-field traces are clumped together. This is the typical inter-grain V-I behavior found in STO bicrystals, as Figure 4.9(d) demonstrates. Due to the different applied fields in the CC and bicrystal links, the V-I plots of Figure 4.9 are not an even comparison, but they still successfully demonstrate the similar V-I behavior between STO bicrystals and CCs. Similar behavior was found in other inter and intra-grain links. This observation validates comparisons made in the last Chapter between STO bicrystal V-I plots and the V-I plots obtained from laser-scribed tracks in various CCs.

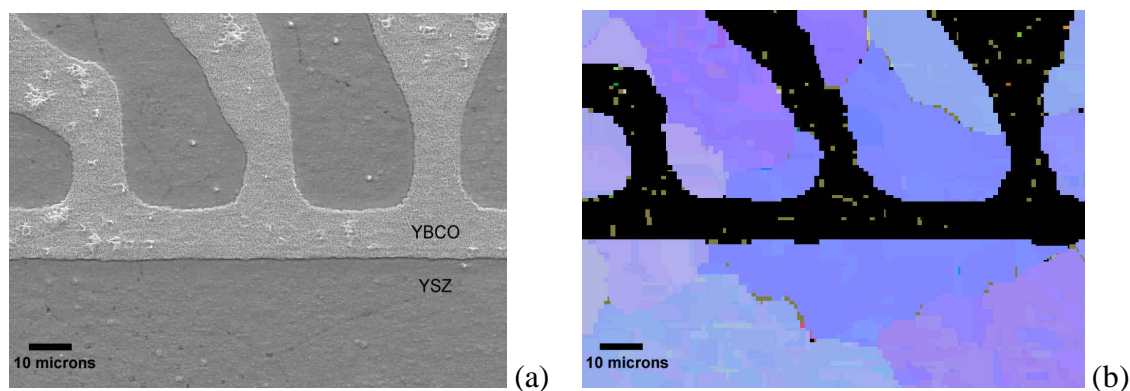


Figure 4.8. SEM and EBKP from sample #5 of Table I. (a) SEM image of a link across a 7.1° GB and an adjacent intra-grain link. (b) EBKP map of the same region as (a), clearly showing the location of the Ni grains. The orientation data was taken off the exposed YSZ layer. Data could not be obtained from the YBCO, indicated by the black pixels in the map.

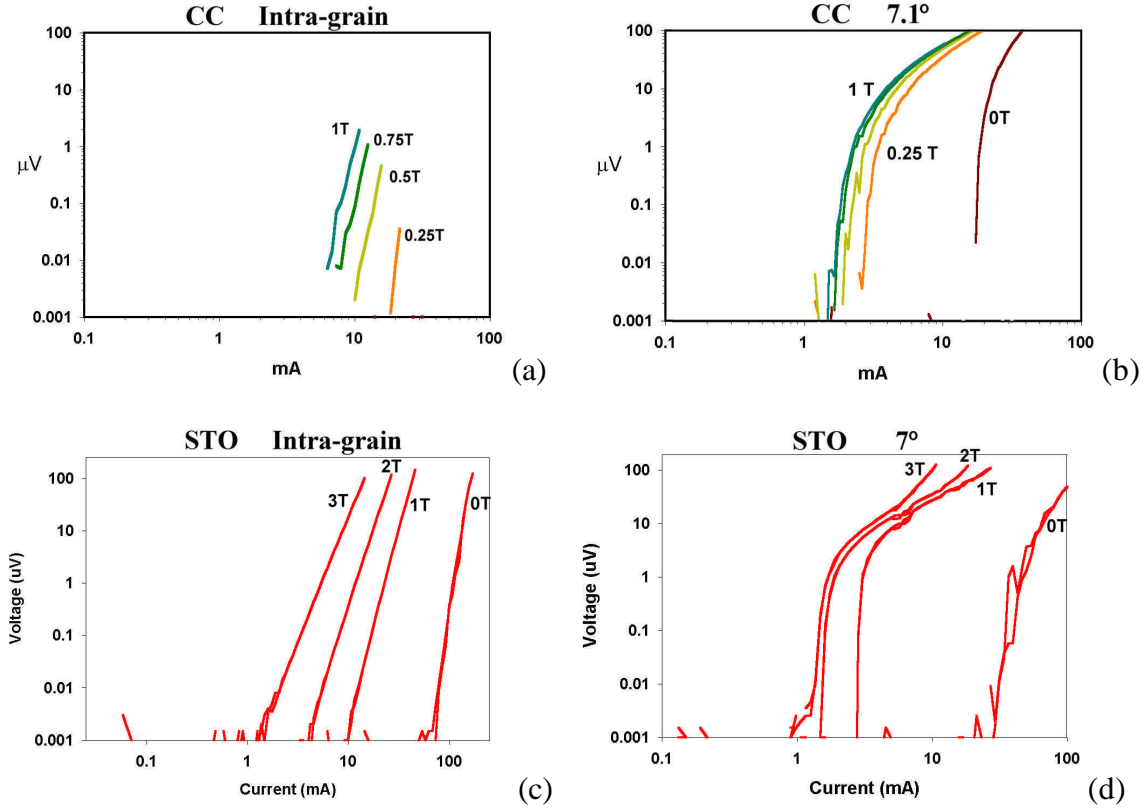


Figure 4.9. V-I traces of the links in Figure 4.8 and from STO bicrystals for comparison. (a). V-I traces of the intra-grain link of Figure 4.8. Visible traces are 0.25, 0.5, 0.75 and 1 T. The current of this link was limited by the inter-grain link, and there was no transition at zero field. (b) V-I traces of the inter-grain link of Figure 4.8. Traces are 0 to 1 T in steps of 0.25 T. θ was measured in the YSZ and found to be 7.1° . (c) V-I traces of an intra-grain link from a 7° STO bicrystal. Visible traces are 0, 1, 2 and 3 T. (d) V-I traces of an inter-grain link in a 7° STO bicrystal. Visible traces are 0, 1, 2 and 3 T.

The links in Table I yield a large spread in $J_c(77\text{ K}, 0\text{ T})$ of 0.4 to 5.1 MA/cm^2 . This is in contrast to the full-width $J_c(77\text{ K}, 0\text{ T})$ values (where available), which were all $\sim 1\text{ MA/cm}^2$. Thus the links range from one-half to more than four times full-width J_c values. This demonstrates that full-width values must be the result of multiple current paths of both higher and lower J_c , resulting from variations in the inter and intra-grain J_c . This is quantitative proof of current percolation on the scale of the substrate grains. The very high intra-grain J_c values strongly suggest that the full-width J_c values of Table I are

not being limited by the intra-grain J_c , but rather by the GBs. The full-width J_c values of the best samples, though rare, are in the range 2.0-2.5 MA/cm². As all the intra-grain links in this study had a J_c that exceeds these values, even the best short length samples that have been made to date are not being limited by the intra-grain. This clearly identifies GBs as the most significant current limiting mechanism in deformation textured CCs, a result that is fully consistent with the transport MO imaging of the last Chapter.

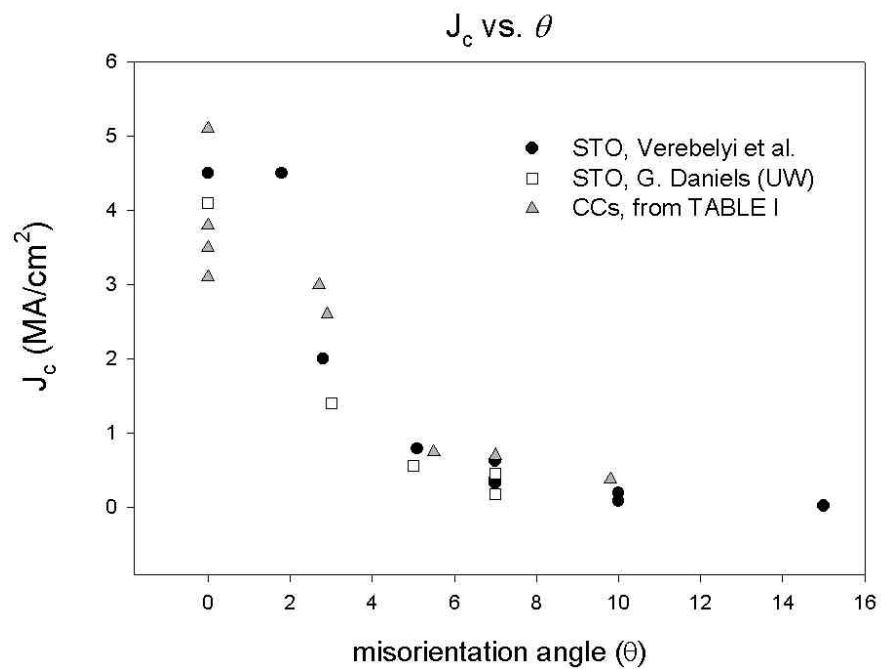


Figure 4.10. Plot of the $J_c(\theta)$ dependence for STO bicrystal GBs and CCs. The bicrystal data is the same data plotted in Figure 1.2. The CC data points are from Table I. All three data sets fit well to the same exponential fall-off, with a q_c of 2-3°.

Figure 4.10 plots the \mathbf{q} dependence of the J_c data from Table I with data from studies using [001] tilt SrTiO₃ (STO) bicrystals (same data as Figure 1.2). The $J_c(\mathbf{q})$ dependence of the GBs in this study and those using (STO) bicrystal substrates all fit very well to an exponential decay with a critical angle (\mathbf{q}_c) of 2-3°. The inter-grain J_c values from Table I are slightly higher (for a given \mathbf{q}) than those of the STO bicrystals. This is likely due to the fact that \mathbf{q} was (largely) measured in the YSZ buffer layer, and \mathbf{q} in the YBCO may be less by 0.5-2.0°. If the inter-grain data from this study were shifted to the left $\sim 1^\circ$ in the plot of Figure 2, they would coincide even better with the data from STO bicrystals. The plot of Figure 2.8(a) suggests that the error introduced by measuring \mathbf{q} in the YSZ layer will be greatest for the largest \mathbf{q} and least for the smallest \mathbf{q} . Because of the shape of the $J_c(\mathbf{q})$ curve, where the error in \mathbf{q} is largest $J_c(\mathbf{q})$ is least sensitive to changes in \mathbf{q} , and an accurate determination of the $J_c(\mathbf{q})$ dependence can still be made. While the excellent fit between the bicrystal and CC data of Figure 4.10 may not be surprising, it is interesting to consider that all of the bicrystals were [001] tilt boundaries and their \mathbf{q} represents purely in-plane misalignment. In CCs, even though there is a high degree of *c*-axis alignment in the substrate grains, the misorientation axes of the GBs are generally distributed with equal numbers near the [001], [110], and [111] directions. Also, \mathbf{q} represents the total misorientation between two grains, which is usually not just an in-plane misalignment. Additionally, the STO bicrystals are manufactured by fusing two single crystals together under heat and pressure, and the GBs in a deformation textured substrate are ‘naturally’ occurring. Despite these and other potential differences between the CC and bicrystal GBs, the most significant factor in determining J_c appears to be \mathbf{q} . This is consistent with studies of YBCO on tilt and twist bicrystal substrates

[21]. There is a moderate variation of the intra-grain data in Figure 4.10, but not significantly more than is generally seen in YBCO films grown on single crystal substrates [5]. It should be noted that the intra-grain data represents films of different thickness and deposition method. Also, each Ni grain acts as its own single crystal template with varying vicinal angle and surface quality, so some variation of the intra-grain J_c is not unexpected. All intra-grain J_c values are high, comparable to the best reproducible values obtained on single crystal substrates demonstrating that there is no reduction in quality of YBCO grown on a metal substrate.

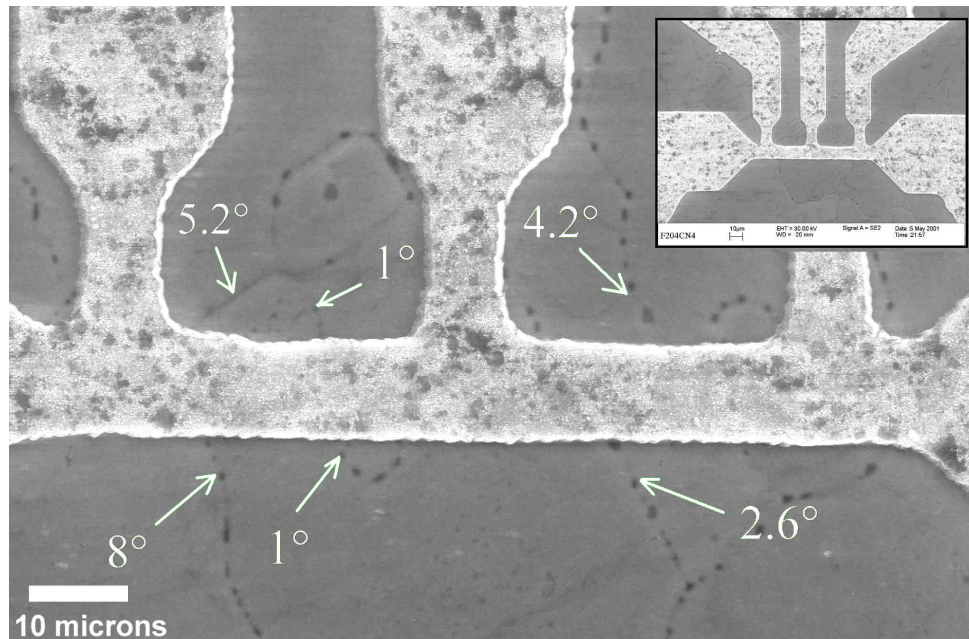


Figure 4.11. SEM image of two links patterned in a CC sample with $0.93 \text{ MA/cm}^2 J_c$. Both links had multiple GBs per link. Some of the GBs were measured in the YSZ layer and are labeled. The GBs are difficult to see in the YBCO layer, and their exact location in the links is not clear. The inset is a lower magnification image of the links.

Figure 4.11 is an SEM image of a pair of links that was excluded from Table I, as each link consists of multiple GBs. These links cannot be used to investigate intra or individual inter-grain behavior, but did provide an opportunity to investigate a very small system of GBs. As most of the samples were patterned blindly, there were many instances like the sample in Figure 4.11. This sample is chosen as an example of such links because it exhibited some remarkable behavior. The GBs in the exposed YSZ layer can be easily seen, but where these GBs are located in the YBCO is less clear. EBKP analysis was used to measure the q of several of the GBs, and these boundaries are labeled in the figure. Figure 4.12(a) is a V-I trace of the left link of Figure 4.11. Examination of the plot legend reveals that the 1 T trace crosses both the 0.6 and 0.8 T traces, and the link has a *higher* J_c value at 1 T than at either 0.6 or 0.8 T. This can also be seen in the $J_c(H)$ dependence of the link shown in Figure 4.13; there is a local maximum in the plot at 1 T. The sample was removed from the rig and re-measured on two separate occasions with identical results. This behavior may be due to matching field effects [50]. The current of the right link was limited by the left link, and traces below 1 T were not attainable. For this reason it is not certain if this link exhibits similar behavior.

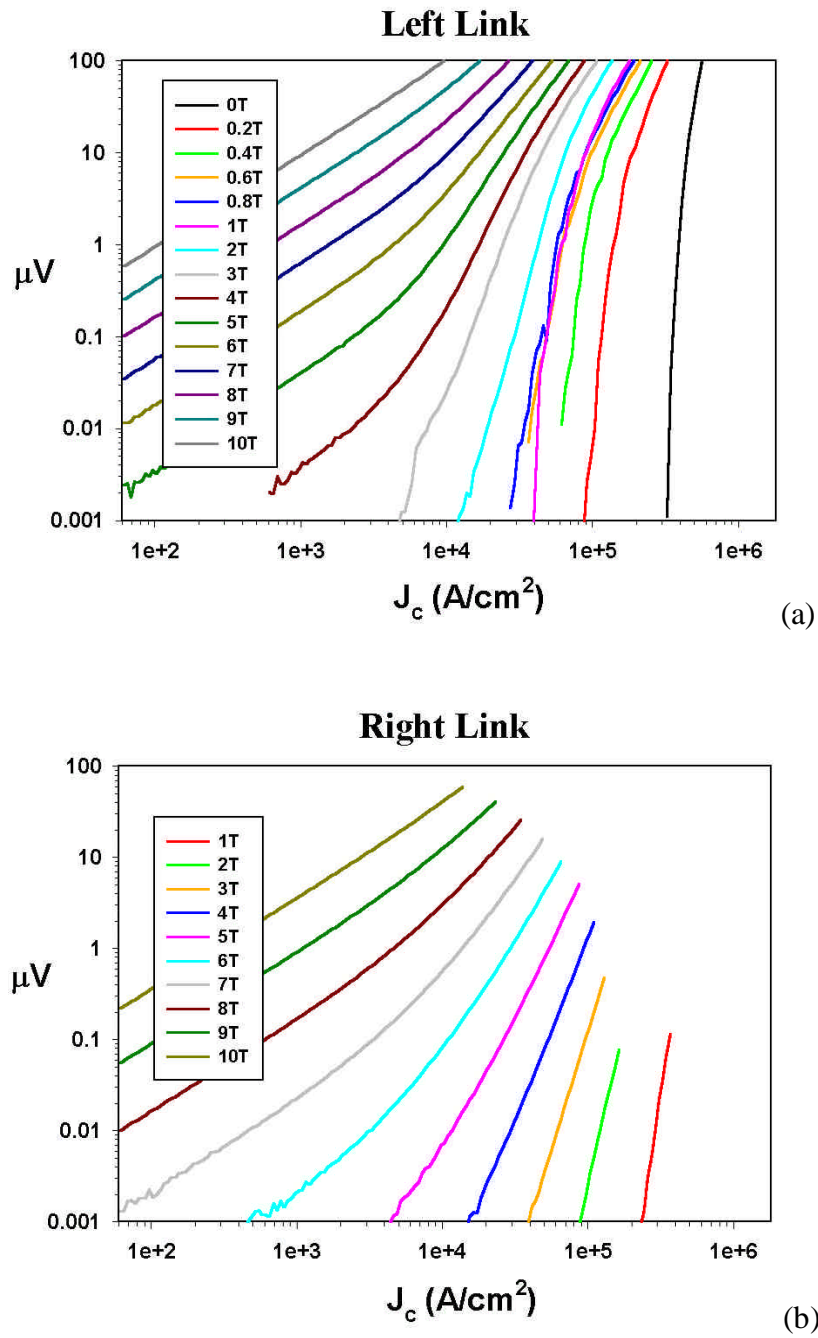


Figure 4.12. V-I plots of the left and right link of Figure 4.11. (a) V-I plot of left link. The 1 T trace has a higher J_c than either the 0.6 or 0.8 T traces. (b) V-I plot of the right link. The current was limited by the left link, and there were no transitions below 1T.

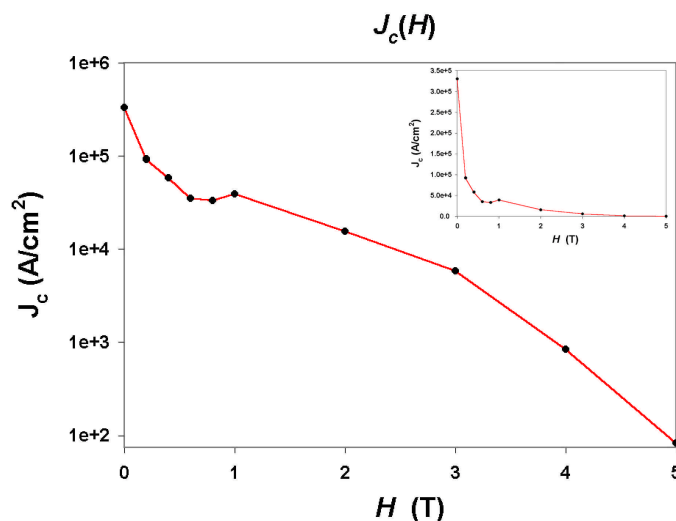


Figure 4.13. $J_c(H)$ dependence of the left link of Figure 4.11. The $J_c(H)$ plot exhibits a local maximum at 1T. The inset is the same data on a linear-linear plot.

An additional sample, shown in Figure 4.3(b), also exhibited remarkable behavior. The center voltage tap of this sample was damaged, so measurements were done using the outer pair. From the image, this now ~60 μm long link is clearly inside a single Ni grain, and it exhibited typical intra-grain V-I behavior. The $J_c(0\text{ T}, 77\text{ K})$ of this link was 12 MA/cm², an abnormally high value. This value was extensively checked. The sample was re-measured on several occasions with consistent I_c values. There were no detectable current paths in parallel with the link, such as a short to the Ni substrate. The width and length of the links were measured with LM and plan-view SEM, and the thickness of the sample was confirmed with cross-sectional SEM. It has been suggested that the intra-grain J_c of CCs may be higher than single-crystal substrates, perhaps due to an increased defect density [51,52]. No values near this one were found in the other samples, and the validity of the J_c value remains in question if for no other reason than it

is exceptionally high. If true, it has interesting implications for the upper limit to J_c in deformation textured CCs.

4.3 Summary and conclusions

This Chapter expanded on the MO imaging results of the previous Chapters by providing a true quantitative demonstration of percolative current flow on the scale of the Ni grain size. This was the first work to successfully quantify both inter and intra-grain regions in CCs. The high intra-grain J_c values found here (3-5 MA/cm²) prove that there is no degradation in YBCO grown on a metal substrate, and that the intra-grain film quality in CCs is comparable to YBCO grown on single crystal substrates (such as STO). This is an important result, because it very clearly shows that the full-width J_c values of CCs are not being limited by the intra-grain J_c . That an intra-grain J_c value of 5.1 MA/cm² can be found in a CC of modest full-width J_c (1.26 MA/cm²) implies that local texture is the single greatest factor separating ‘typical’ samples from the ‘best’ samples.

The derived $J_c(\mathbf{q})$ dependence was found to fit well with previous bicrystal studies and the patterned links of Table 4.1 had J_c values both above and below full-width measured values, proving that current must percolate through these inter and intra-grain regions. V-I behavior of CC GBs was similar to bicrystal GBs, validating comparisons made in the last Chapter. These results again identify GBs as the major current limiting mechanism in these conductors and demonstrate that current flow must be percolative, two points which well corroborate the MO imaging studies of the previous two Chapters.

5

Summary

The purpose of this thesis work was to provide a detailed understanding of the current flow in deformation textured coated conductors. More than three dozen samples were investigated from multiple sources so as to determine the global behavior of these conductors. The samples were studied using multiple characterization techniques, including LM, SEM, MO imaging and detailed transport measurements. In this Chapter, the work is summarized, and implications for the technology are discussed.

5.1 Summary of Results

It is hoped that this work was presented in a logical progression, from MO images of global electromagnetic granularity to detailed transport measurements of the inter and intra-grain. The theme of this thesis has been the percolative nature of current flow in deformation textured CCs, and each of Chapters Two, Three and Four demonstrated this in a unique way. In all cases, GBs were found to be the most significant factor limiting J_c , a point of view not previously accepted.

The electromagnetic granularity of deformation textured CCs was demonstrated in Chapter Two. This was done through MO imaging under an applied magnetic field. The granularity was found to be uniform throughout the samples, and was found in all samples investigated. Flux profiles showed that the conductors were carrying a macroscopic magnetization current convoluted with local, smaller current loops that gave rise to the electromagnetic granularity. By combining LM and MO images, the electromagnetic granularity was shown to be the result of the substrate grain structure. From previous bicrystal studies it is known that GBs appear in MO images when J_{cb}/J_{cg} is less than unity, and orientation mapping found this ratio to be highly dependent on the GB misorientation angle. Analysis of the texture development from the Ni through the oxide layers showed that the YBCO was not growing epitaxially on the buffer layers, but rather exhibited an improvement in *c-axis* alignment that produced an improvement in q . Besides establishing the granular nature of deformation textured CCs, these results strongly focused attention on the substrate as the source of the ‘problem’.

In Chapter three, MO imaging the self-field produced from an applied transport current clearly demonstrated that transport current flow in deformation textured CCs is percolative as well. This was the expected result after the experiments of Chapter Two, and while both transport and magnetization MO images can be very similar, a lot of new information was gained by the transport MO studies. Coupling the transport MO images with V-I measurements demonstrated that current flow is percolative from before the onset of dissipation to well after, and current flow is never uniform or single-crystal-like throughout the entire link. At I_c (or J_c) dissipation was not spread out over all the GBs, but rather was isolated at a small subset of existing GBs, and much of the link was

carrying a current less than its local J_c . This emphasized the importance of good *local, grain-to-grain* texture in producing high- J_c tapes.

In Chapter Four, the transport measurements of inter and intra-grain regions of several different CCs showed that the $J_c(\mathbf{q})$ dependence and VI behavior of CC GBs was extremely similar to that of previous bicrystal studies. All intra-grain J_c values were high, comparable to films grown on single-crystal substrates. This demonstrated that excellent quality YBCO could be grown on a metal substrate, and quantitatively demonstrated the full-width J_c of CCs was not being limited by the intra-grain. Inter and intra-grain J_c values were found to vary from one half to more than four times full width measured values, demonstrating in yet another way that current flow must be percolative and clearly identifying the GBs as the source of the percolation.

5.2 Implications for the technology and conclusions

The consequence of the percolative nature of current flow in CCs and the fact that GBs and not the intra-grain will nearly always limit J_c means that a sharp substrate texture is paramount to obtaining high J_c tapes. One question such emphasis on texture raises is what is the upper limit to J_c in a CC? From the plot of Fig. 4.10, a J_c value of 2.5 MA/cm² is roughly equivalent to that of a 3° GB. While many GBs greater than 3° certainly exist in the ‘best’ samples, such J_c values indicate an extremely high degree of substrate texture. It is uncertain that substrate textures can be sharpened to a significantly greater degree than those that already produce samples in the range of 2.0-2.5 MA/cm².

If there is a limit to the degree of texture that can be obtained in a substrate, further I_c improvements may need to come from thicker films, not greater J_c values. An important goal of much of the present scale-up is to achieve high J_c values in CCs with $> 1\text{-}2\ \mu\text{m}$ thick films [53-55]. Another means of increasing CC J_c values is to improve GB properties. Ca doping of YBCO has demonstrated this possibility in high angle GBs [56] and in low angle GBs at low temperatures [57], but it has yet to be shown in low angle GBs at 77 K. It should also be observed that most full-width J_c values, including all of those in Table I, are the result of voltage taps ~ 4 mm apart on a sample that is 3-5 mm wide. From the point of view of current percolation, this is a generous aspect ratio. Keeping the grain size and width of the tape fixed, modeling has shown that J_c decreases with increasing tape length [32], and it has yet to be demonstrated that good local texture can be maintained over commercially useful lengths.

Maintaining good texture over long lengths will be critical to producing commercial tapes, but as pointed out by Verebelyi *et al.* [58], the influence of GBs in a CC is reduced at very high fields, and the application may dictate the degree of texture required. The characterizations of this thesis provide a vital insight for the technology as it matures towards longer lengths, non-magnetic substrates, thicker YBCO layers, and more automated processes. The percolative nature of current flow seen in all samples and the discovery of intra-grain J_c values in excess of $5\ \text{MA}/\text{cm}^2$ is direct proof of the untapped potential of coated conductors.

A

Magneto-Optical Imaging

Magneto-optical imaging is a method of visualization of magnetic flux. The technique is an old one, and was first applied to superconductivity in 1957 by P.B. Alers [59]. It is quick and, if your sample fits in the cryostat, non-destructive. MO imaging has been an invaluable tool in discovering and identifying inhomogeneities in many types of superconducting samples and especially YBCO thin films. In fact, it is so good at this, that it has often *not* been a popular characterization tool with many of our collaborators. The purpose of this Appendix is to familiarize the reader with MO imaging and address many commonly asked questions about the technique.

A.1 The indicator film

Magneto-optical (MO) imaging is based on the Faraday effect, which is the rotation of the plane of polarization of a beam of light by a magnetic field. The *indicator film* contains a thin layer of material that exhibits the Faraday effect. A diagram of the cross section of an indicator film is shown in Figure A.1. The substrate is made from

Gadolinium Gallium Garnet (GGG). The magneto-optically active layer (exhibiting the Faraday effect) is deposited on top using liquid phase epitaxy [60]. The layer is a garnet material and may have one of several different compositions, but most of our films are $(\text{Bi,Lu})_3(\text{Fe,Ga})_5\text{O}_{12}$. The layer may vary in thickness from 1-6 μm . On top of the garnet material a reflective layer of Al is deposited (~ 150 nm) and a hard protective layer of Ti_3N_4 (~ 150 nm).

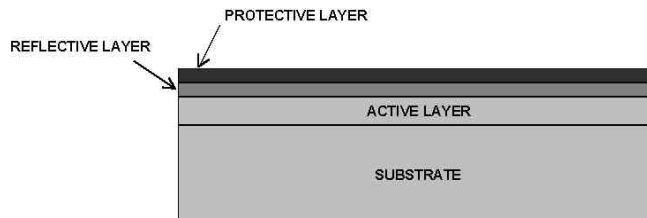


Figure A.1. Cross-section of a typical indicator film.

In practice the indicator film is used “upside-down”, as shown in Figure A.2. This allows the magneto-optically active layer to be closest to the superconducting sample. This is important, as the distance this layer is from the surface of the sample determines the limit of spatial resolution. Light incident on the indicator film travels through the GGG and the garnet layer, and is reflected back by the layer of Al. Both the GGG and the garnet layer are transparent. The purpose of the Ti_3N_4 is to prevent the Al and garnet layers from excessive scratching.

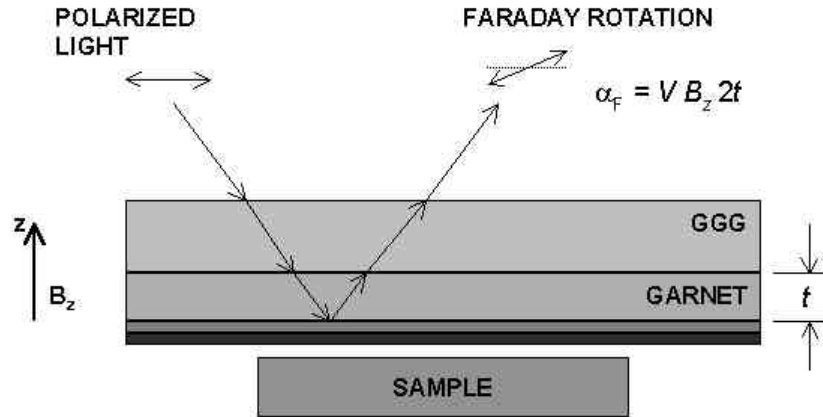


Figure A.2. Diagram of the use of an indicator film in the investigation of a superconducting sample.

In the geometry of Figure A.2, polarized light incident on the indicator film will undergo a Faraday rotation, α_F . The magnitude of the rotation, α_F , is given by

$$\alpha_F = V B_z 2t \quad \text{A.1}$$

where V is the material dependent *Verdet* constant, B_z is the magnitude of the perpendicular applied field, and t is the thickness of the magneto-optically active layer. Polarized light reflected off the indicator film will carry with it information about the local magnetic field according to Equation (A.1). When this reflected light is viewed through a polarizer, this information will appear as spatial variations in intensity. This is diagrammed in Figure A.3. The indicator film will only rotate the plane of polarization of incident *polarized* light – it is not itself a polarizer. It should also be emphasized that MO imaging is only sensitive to the z component of the magnetic field, B_z .

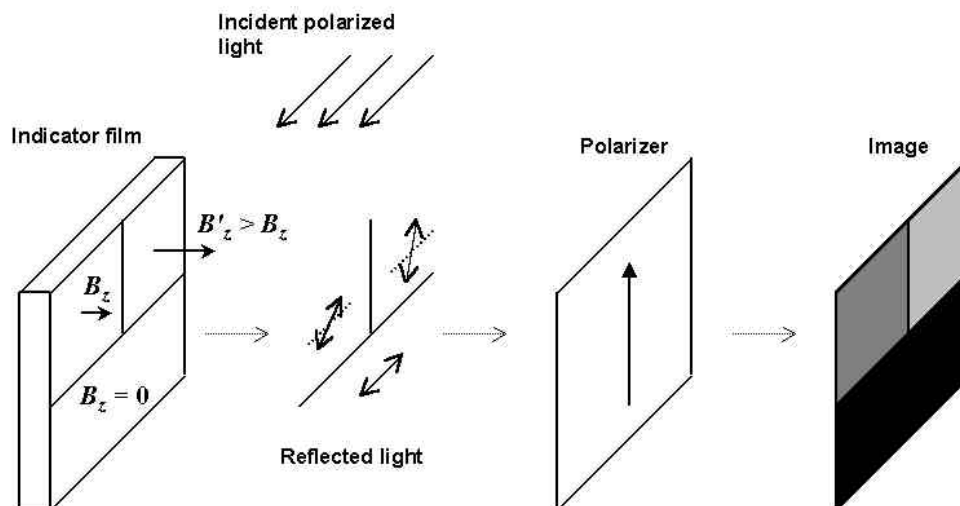


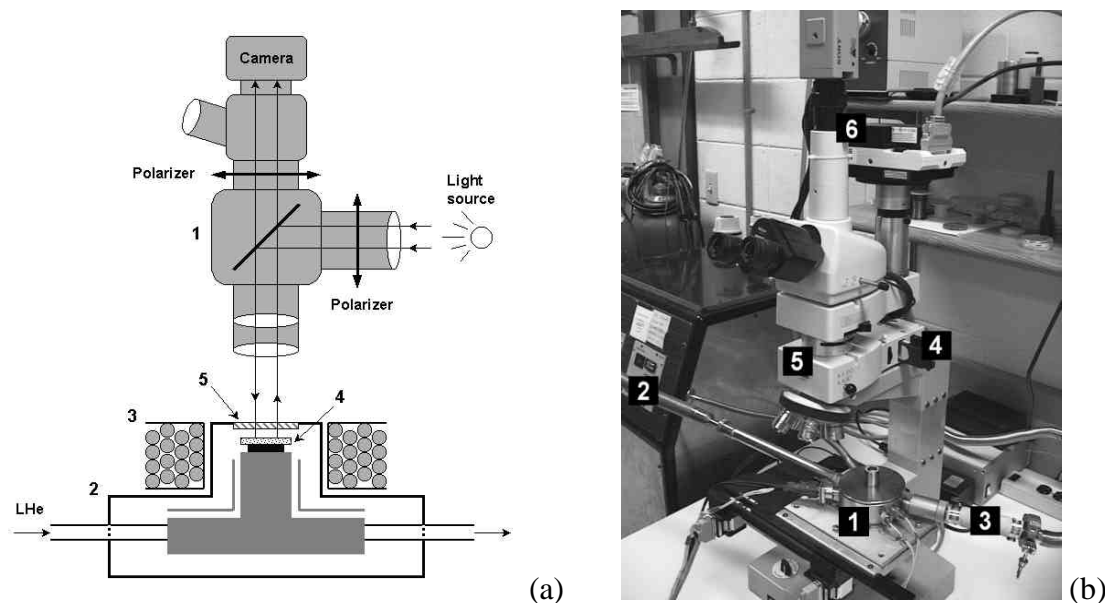
Figure A.3. Incident light undergoes varying degrees of Faraday rotation depending on the local magnetic field. When the reflected light is viewed through a polarizer, the information about the local magnetic field in the indicator film appears as variations in intensity.

For more details about the MO indicator film please see Polyanskii et al [61].

A.2 Equipment and Imaging Geometry

The equipment setup for MO imaging is relatively simple. The major components are a small cryostat with an optical window, a microscope, and a digital camera with a computer for image collection. A schematic is shown in Figure A.4a, and a picture of our present setup in Figure A.4b. The microscope is a standard light microscope that has been modified to contain two polarizers, one for polarizing the incident light, and the other for viewing the light reflected off the indicator film. The latter polarizer can be rotated to produce different contrasts and colors in the final image.

The cryostat is a small continuous flow LHe cryostat capable of operating from 10K to above room temperature. An optical window allows viewing of the sample and indicator film. The cryostat moves via a motorized XY-stage. A small electromagnet provides magnetic fields up to 1200 Gauss. A digital camera is attached to the microscope for live previewing and image collection.



Figures A.4. a) Diagram of a MO imaging setup. 1. Microscope, 2. Cryostat, 3. Solenoid, 4. Sample and indicator film, 5. Optical window. b) Picture of our present MO imaging setup. 1. Cryostat, 2. LHe transfer tube, 3. Vacuum line, 4. Polarizer (incident light), 5. Polarizer (reflected light), 6. Digital cameras.

An example of MO imaging is shown in Figure A.5. An indicator film has been placed on the magnetic strip on the back of a credit card, Figure A.5(a). The resulting image, taken with a digital camera attached to the microscope, is shown in Figure A.5(b). The alternating light and dark lines are produced from components of B_z into and out of the plane of the indicator film. Permanent magnets in the credit card are placed with

north poles facing north poles and south poles facing south poles [Figure A.5(c)]. This results in significant B_z components only where poles meet.

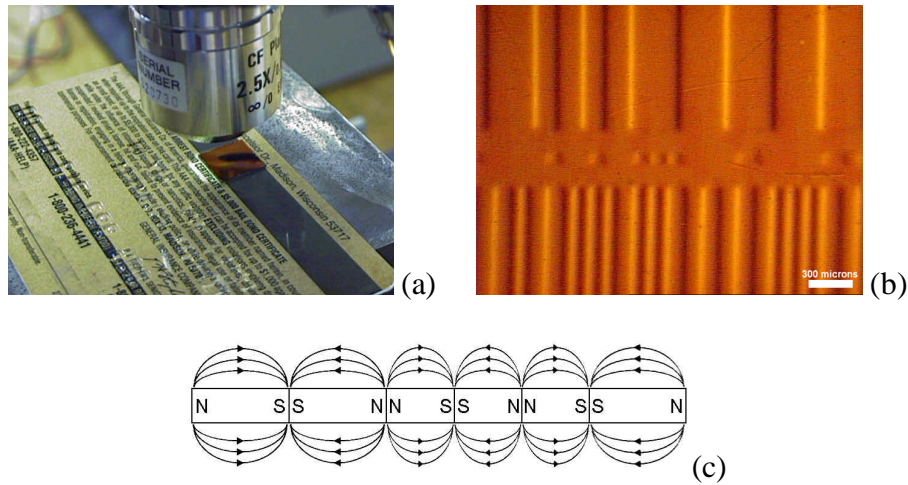


Figure A.5. a) Image of a credit card and indicator film underneath a microscope. b) MO image of the credit card and indicator film of shown in a). c) An arrangement of permanent magnets in the credit card (viewed on edge) that would result in alternating light and dark lines, as shown in b).

A.3 Imaging modes

For a superconducting sample, there are several possible imaging modes. The two most used in this thesis are zero field cooled (ZFC) and field cooled (FC) imaging modes. For the ZFC mode, the superconducting sample is cooled from above T_c in the absence of an applied magnetic field, and then a magnetic field is applied. In this mode, the sample is resisting the entry of magnetic flux and B_z will have the same direction everywhere, either into or out of the page. For FC MO images, the sample is cooled from above T_c in the presence of an applied field, and then the field is removed. In the FC

mode, the sample is trapping magnetic flux and there will be both positive and negative values of B_z . These different directions of B_z manifest themselves as different colors in the MO image, and FC images will often be more colorful than ZFC images. Examples of ZFC and FC regimes are shown in Figures A.6(a) and (b) respectively. Another imaging mode is *transport* MO imaging, but this mode is described in detail in Chapter Three.

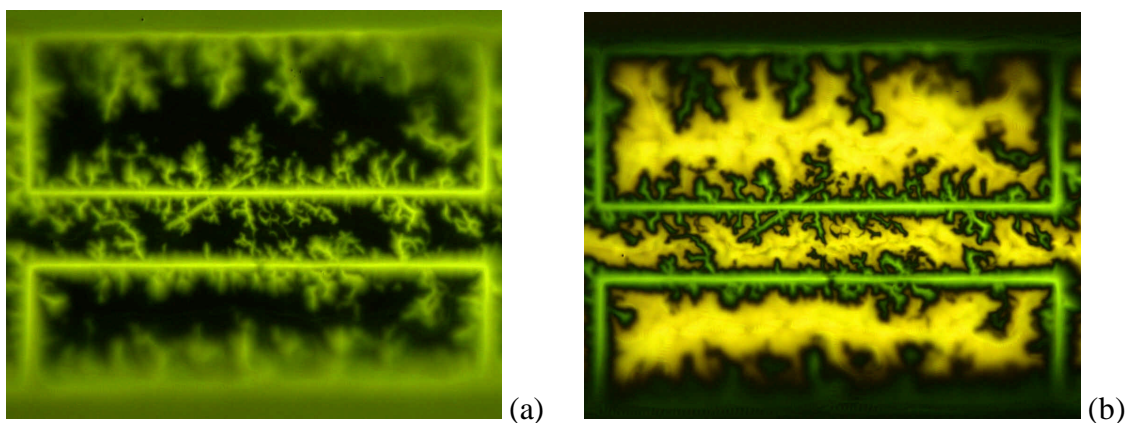


Figure A.6. Examples of the ZFC and FC MO imaging modes. (a) Sample was ZFC to 40 K, and then a field of 40 mT was applied. (b) Sample was FC in a field of 40 mT to 40 K, and then the field was removed.

A.4 Interpretation of magneto-optical images

In interpreting and understanding MO images, it may be helpful to remember several points. First, the pixel intensity of a MO image scales roughly linearly with magnetic field strength. Figure A.7 plots the image intensity against applied magnetic

field for a fixed angle of the two polarizers. Because of the (approximately) linear relationship between image intensity and magnetic field strength, MO images can often be thought of as density maps of the local magnetic field.

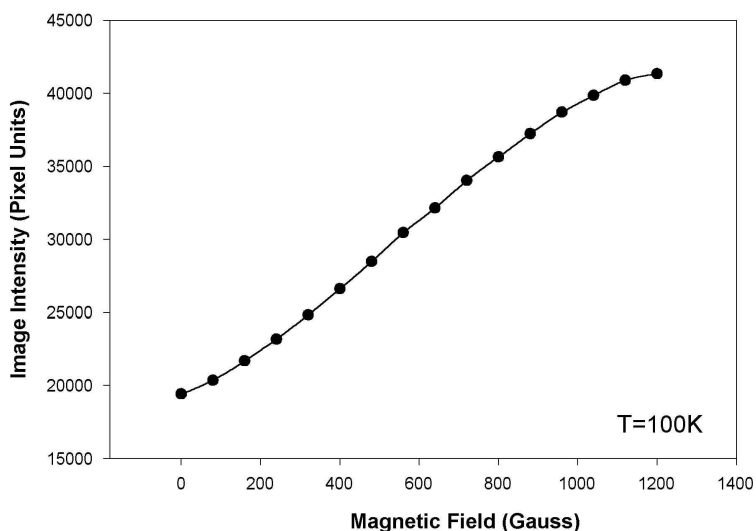


Figure A.7. Plot of image intensity (arbitrary units) as a function of applied magnetic field for a given angle between the polarizers.

Another point to remember is that the colors in MO images are *relative*. The colors and contrast of MO images may be changed by changing the angle between the two polarizers. This is shown in Figure A.8. The *only* difference between Figures A.8(a) and (b) is the angle between the two polarizers of the microscope. No other imaging or sample conditions were changed. Very often in MO images, ‘black’ will represent the zero level of magnetic flux and ‘yellow’ and ‘green’ will represent magnetic field either into or out of the page, but this need not be the case.

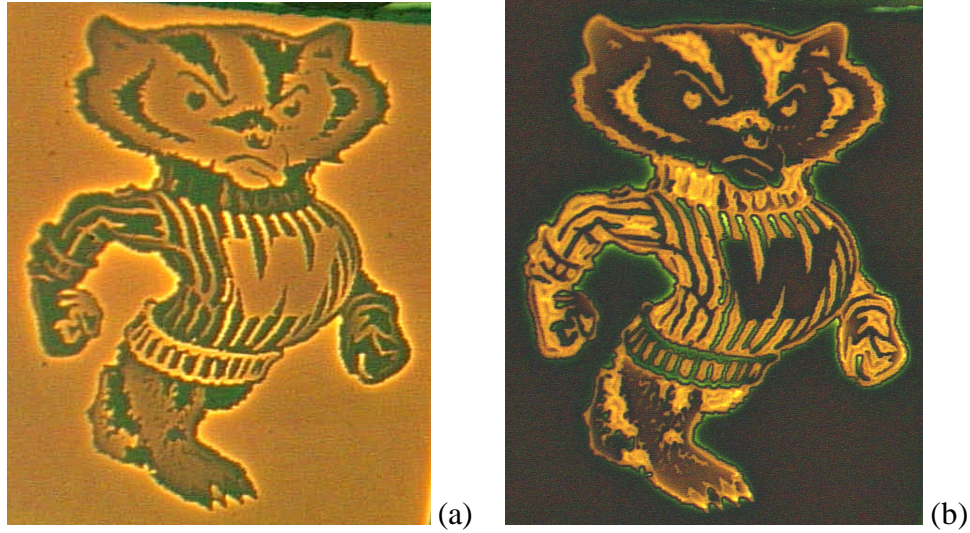


Figure A.8. Two MO images of Bucky Badger, demonstrating that the colors in a MO image are relative and can be changed by changing the angle between the two polarizers of the microscope. For both images, the sample was FC at 60 mT to 12 K. Bucky Badger is YBCO on single crystal STO, grown by George Daniels. It was patterned using a custom optical mask as described in Figure 4.2. Actual size of Bucky is about 3 mm x 4 mm.

Finally, as all of the samples imaged in this thesis are thin films, some examples of the calculated B_z distribution above perfectly uniform thin films are presented. Figures A.9(b), (d) and (f) are density plots of magnetic strength, and represent what MO images of each example would look like. Figures A.9(a) and (b) represent magnetization currents flowing in a square film, Figures A.8(c) and (d) represent magnetization currents flowing in a thin strip, and Figures A.8(e) and (f) represent transport currents flowing in a thin strip. In all cases the sample is assumed to be in the critical state, meaning that $|\vec{J}| = |J_c| = \text{const.}$ everywhere. The “X” pattern of the magnetic field in Figure A.9(b) is commonly referred to as a ‘rooftop’ pattern.

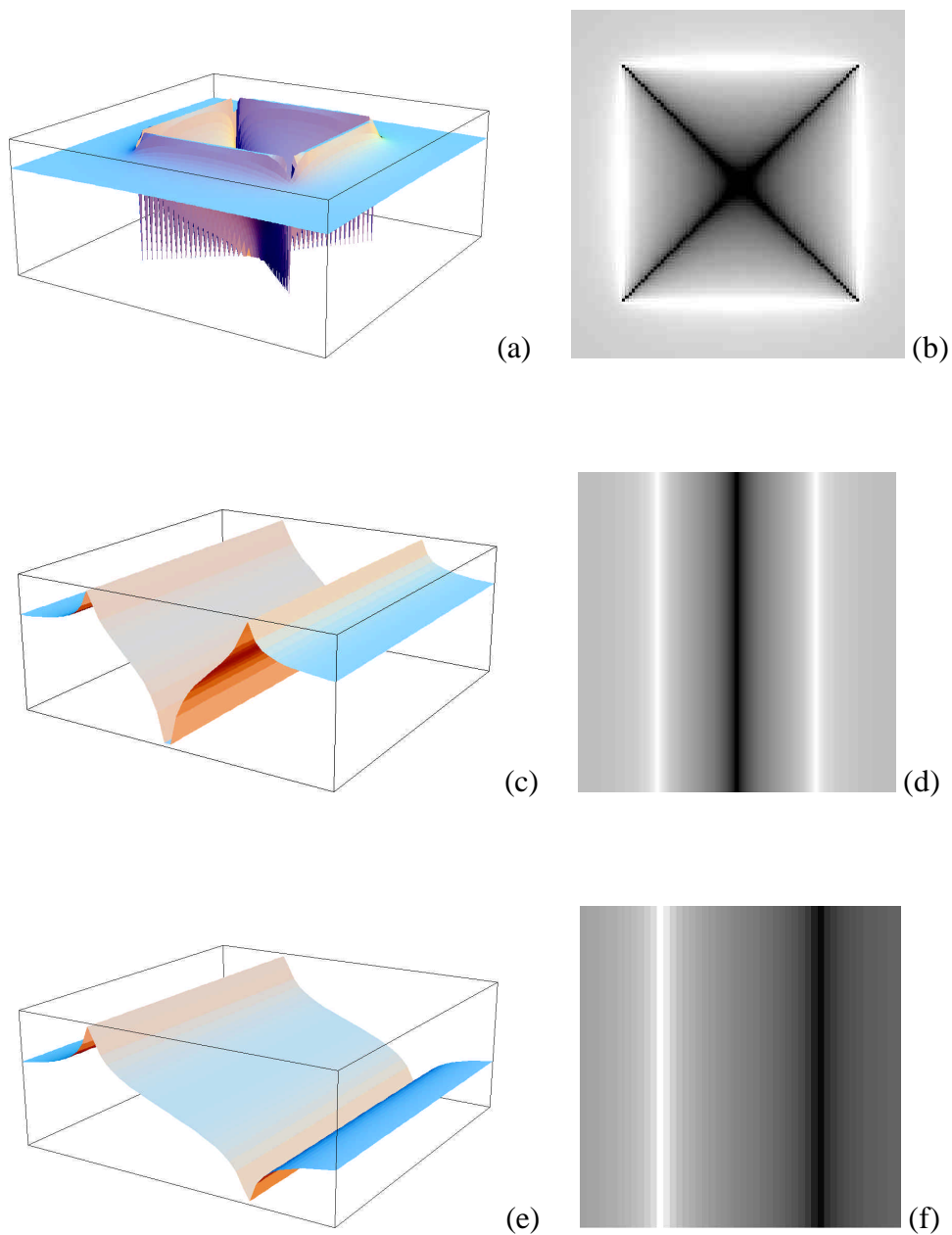


Figure A.9. Calculated B_z distributions for various thin film geometries. In all cases, current flows parallel to the sample edges with $|J|$ equal to a constant everywhere. (a) 3D plot of the B_z distribution above a thin superconducting square. (b) Density plot of the same data in (a). (c) 3D plot of the B_z distribution above a thin superconducting strip. This image models magnetization currents, with currents flowing in opposite directions on either side of the link. (d) Density plot of the same data as in (c). (e) 3D plot of the B_z distribution above a thin superconducting strip. This image models transport currents, with current flowing in one direction everywhere in the link. (f) Density plot of the same data as in (e).

B

Orientation mapping

Electron back-scatter diffraction (EBSD) is a popular technique for measuring grain orientations in an SEM. EBSD is used to produce Kikuchi patterns, which are in turn used to determine crystal orientation. This process can be automated to produce orientation maps of a sample. Detailed information on orientation mapping and analysis of Kikuchi patterns can be found in references [60-62]. A brief overview of the technique is presented here.

B.1 Electron back-scatter diffraction equipment

Figure B.1 identifies all the major components of an EBSD system. A specimen is placed in the SEM, generally at a 70° tilt. An electron beam is incident with the sample and the EBSD patterns are captured by the phosphor screen, which is also inside the SEM chamber. These EBSD patterns are called *Kikuchi* patterns, and are a projection of the lattice plane geometry in a crystal. A leaded glass window separates the specimen and the phosphor screen from the camera, which is on the outside of the chamber.

Cameras may vary from real-time imaging to long-term exposure systems depending on the application and required signal-to-noise ratio.

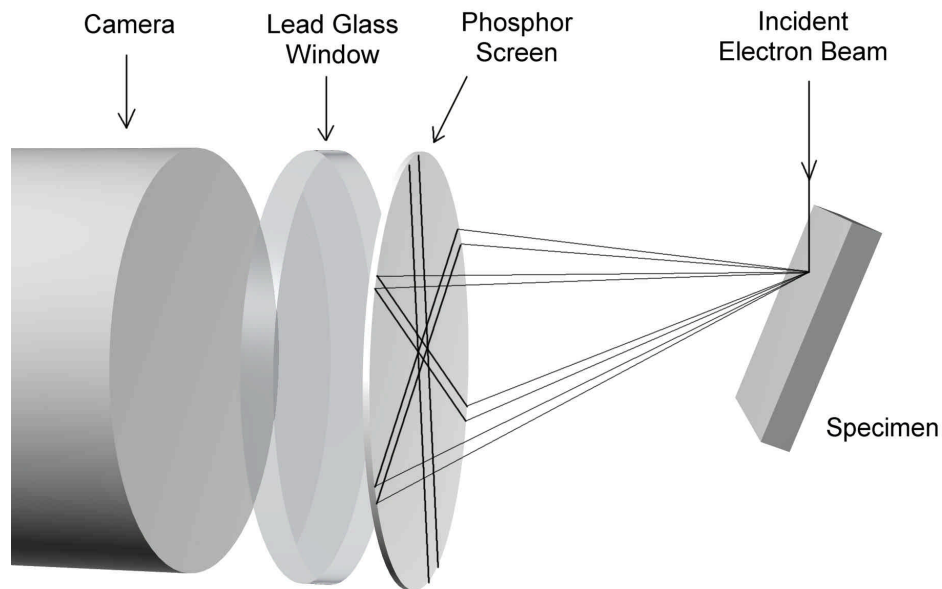


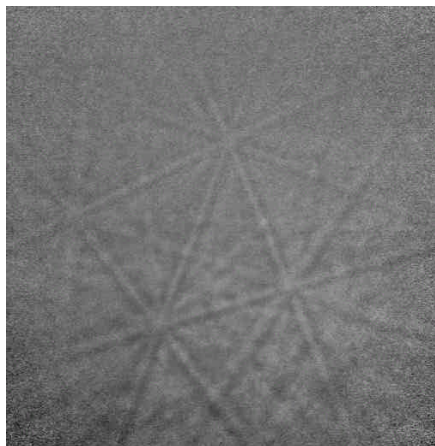
Figure B.1. The major components of an EBSD system. The phosphor screen and the specimen reside inside the SEM chamber, and the camera is outside the chamber. The phosphor screen captures the Kikuchi patterns produced by back-scattered electrons from the specimen surface.

B.2 Orientation mapping

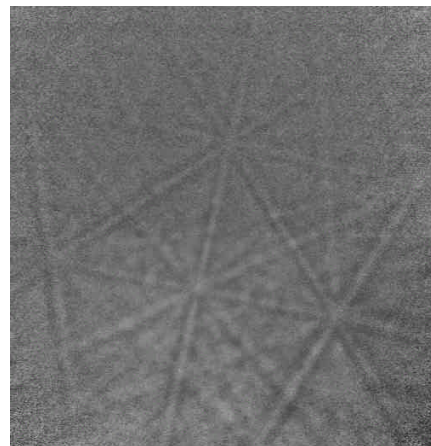
Orientation mapping of a sample in an SEM is performed using the equipment arrangement of Figure B.1 and a computer with the appropriate software. Using the software, the user defines the area of the sample to be mapped and the point density of the scan. The software controls the electron beam of the SEM, stepping it over the

sample in an x - y grid, capturing and indexing a Kikuchi pattern at each point. First, this Kikuchi pattern is indexed by identifying the poles and bands in the pattern [partially indexed patterns are shown in Figures B.2(c) and (d)]. This information is then used to determine a set of Euler angles for the Kikuchi pattern, which define the orientation of the crystal producing the pattern relative to an external reference frame. For each point of the x - y scan, a set of Euler angles is determined. These Euler angles can later be used to determine grain-to-grain misorientations and plot grain boundary maps.

If only the relative orientation of two grains is desired, Kikuchi patterns from each grain may be compared directly. Figures B.2(a) and (b) are patterns taken from two sides of a 36° [001] tilt STO bicrystal. In Figures B.2(c) and (d), several poles and bands are highlighted. The location of the [001] pole (located at the intersection of the bands) is the same in each image. The positions of the [011] and [111] poles has changed, but are related to each other through a rotation around the [001] pole as shown in Figure B.2(e). Measuring the degree of the rotation reveals that the two crystals are misoriented by a 35° rotation around the [001] pole, very close to the bicrystal manufacturer's specification of 36° .



(a)



(b)

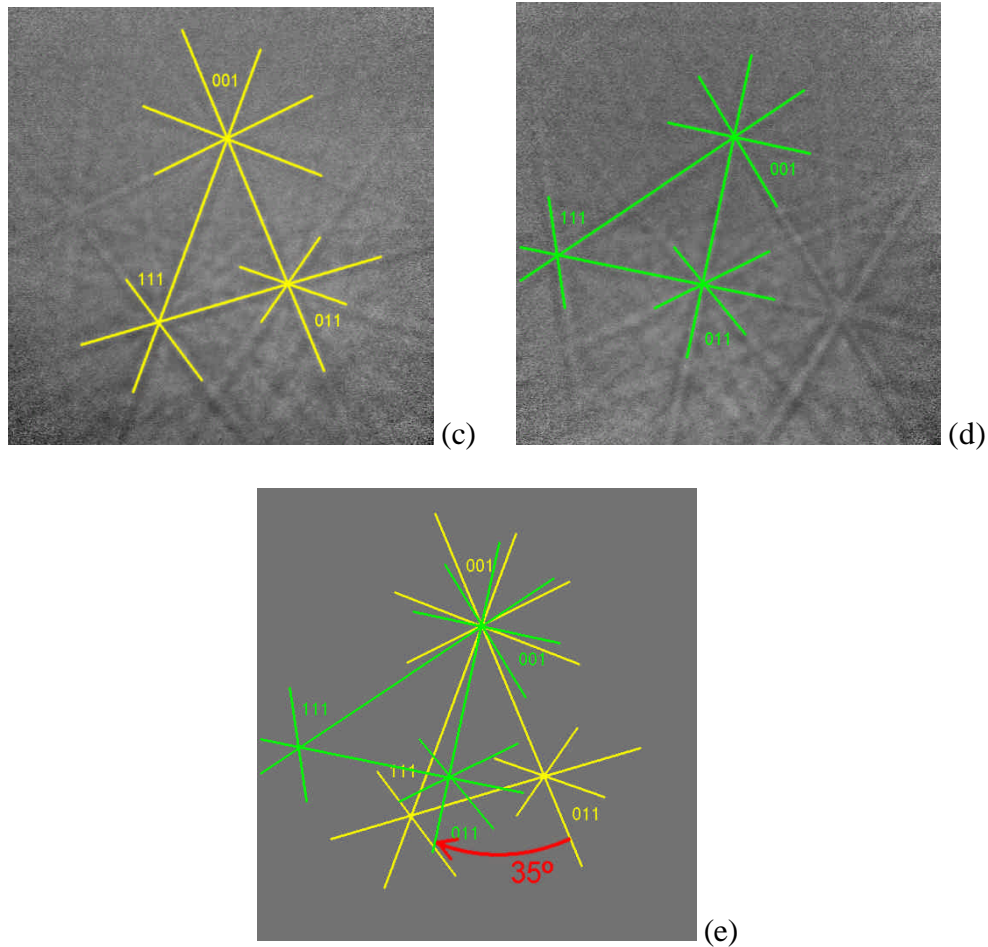


Figure B.2. Kikuchi patterns from opposite sides of an $[001]$ tilt 36° bicrystal. (a) Left side. (b) Right side. (c) Left side, with $[001]$, $[011]$, and $[111]$ poles labeled. (d) Right side, with $[001]$, $[011]$, and $[111]$ poles labeled. (e) Overlay of the highlighted regions of (c) and (d) showing that the Kikuchi patterns from the two different side of the bicrystal are rotated $\sim 35^\circ$ around the $[001]$ pole with respect to each other.

Figure B.3 shows a similar example for a 7° $[001]$ tilt STO bicrystal. The Kikuchi patterns from each side of the bicrystal differ by a 7° rotation around the $[001]$ pole. For Figure B.3(c), electron beam was placed directly on the grain boundary of the bicrystal, and the resulting pattern is a convolution of the patterns from each grain.

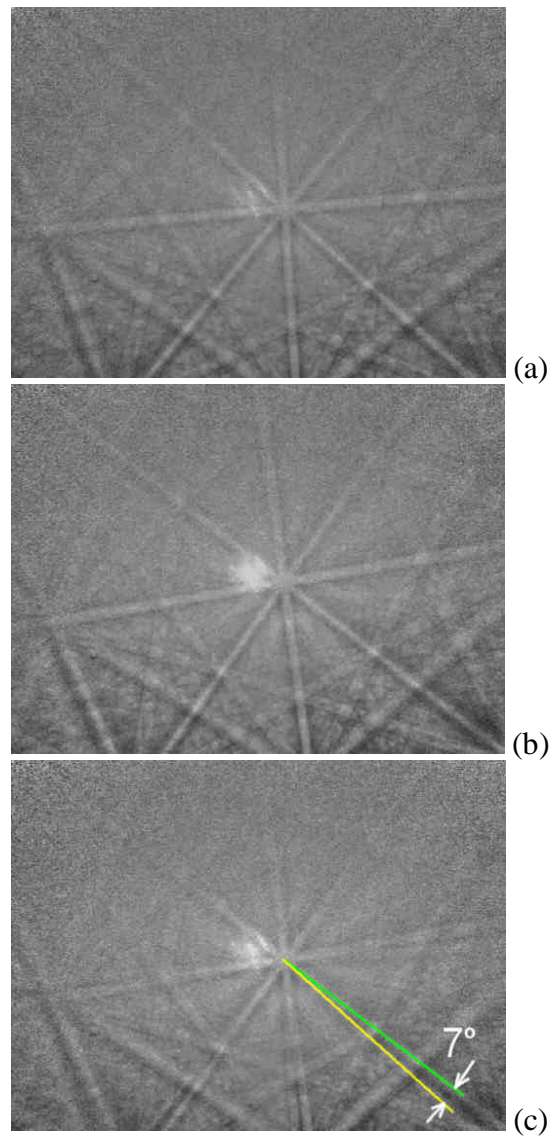


Figure B.3. Kikuchi patterns from both sides of a 7° [001] tilt bicrystal. (a) Kikuchi pattern from the left side centered on the [001] pole. (b) Right side. (c) The electron beam was placed directly on the grain boundary, showing a convolution of the patterns from each side. The patterns differ by a 7° rotation about the [001] pole.

C

Current Reconstruction

The problem of reconstructing a two-dimensional (2D) current distribution from a magnetic field measurement can be reduced to the solution of an integral equation. This equation is characterized by an inherent instability for non-exact (noisy) data. In this Appendix, an approximate solution is found using the method of Regularization. Regularization has long been the most popular means of resolving such equations, and it directly addresses the instability of the problem for noisy data. The convolution form of the integral equation allows the use of the computational efficiency of the Fast Fourier Transform (FFT), but emphasis is placed on accuracy, not speed.

C.1 Introduction

In deformation textured YBCO CCs it has been demonstrated that current percolates on the scale of the underlying Ni grain structure (~20-100 μm). Current reconstruction combined with orientation mapping would be a powerful tool in

determining how current percolates through the GB networks in such conductors. As already mentioned, good samples with non-magnetic substrates have not yet been available.

Under certain conditions it is possible to reconstruct the current flow in a superconductor from a magnetic field measurement. If the current flow can be adequately approximated as two-dimensional (2D) and the sample is in a magneto-static [65] state, then the current flow can be determined. The condition of magneto-statics is easily satisfied, and approximations to 2D current flow are generally valid in thin film geometries [49]. If these conditions are met, the relationship between pixel intensity in a MO image and magnetic field strength (discussed in Appendix A) can be used to produce a quantitative, spatially resolved map of the z -component of the magnetic field above a superconductor. The geometry of such a measurement is shown in Figure C.1. With knowledge of $B_z(x,y)$ above a thin superconducting sample, the current reconstruction problem for thin film geometry reduces to an integral equation of the form

$$\int K(x, x', y, y') f(x', y') dx' dy' = g(x, y), \quad \text{C.1}$$

where the functions K and g are known and f is to be determined. Equation C.1 is known as a *Fredholm integral equation of the First Kind*. Here K is known exactly and g is known at only a discrete number of points, and with errors. This equation is also characterized by an inherent instability for non-exact data, a trait common to most First Kind integral equations. Small changes in the measured quantity g can produce large changes in f , and the solution does not depend continuously on the data. As a

consequence, the function f that best satisfies Equation C.1 for a given (non-exact) data set g may deviate greatly from the true solution. First kind integral equations have been well studied in the literature and several methods exist for their evaluation [66-68]. The most popular (and most successful) of these methods is the method of Regularization [68]. Regularization replaces Equation C.1 with a similar, but better-behaved, problem. An excellent primer on First Kind integral equations and various solution methods is given by Wing [69].

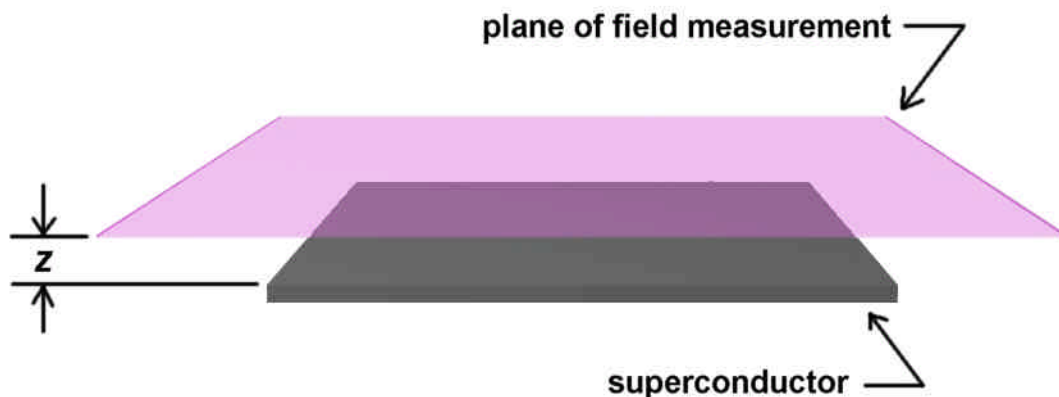


Figure C.1. Experimental geometry for performing a current reconstruction in a thin superconductor. A $B_z(x,y)$ distribution is measured by MO imaging, in a plane a distance z above the surface of the sample. With the map of $B_z(x,y)$, the currents in the superconductor can be determined.

C.2 Resolution of the magnetic inverse problem

To derive the current flow in a superconductor from a measured $B_z(x,y)$ distribution it is necessary for the current to be adequately approximated as 2D, i.e. that

the z dependence of the current is negligible. It is also required that the superconductor be in a magneto-static state so that

$$\nabla \cdot \mathbf{J} = 0 \quad \text{C.2}$$

This condition is strictly violated by thermal flux creep, but since this occurs over time scales much greater than the typical $B_z(x, y)$ measurement, the effect of flux creep can generally be neglected. Equation C.2 is automatically satisfied if the current is written in terms of a stream function [49]:

$$J_x(x, y) = \frac{\partial F(x, y)}{\partial y} \quad \text{and} \quad J_y(x, y) = -\frac{\partial F(x, y)}{\partial x} \quad \text{C.3}$$

The contours of the function $F(x, y)$ are the current streamlines. The magnetic field is related to the current by the Biot-Savart law:

$$\mathbf{B}(\mathbf{x}) = \frac{\mu_0}{4\pi} \int \mathbf{J}(\mathbf{x}') \times \frac{(\mathbf{x} - \mathbf{x}')}{|\mathbf{x} - \mathbf{x}'|^3} d\mathbf{x}' \quad \text{C.4}$$

Substituting Equation C.3 into the z component of Equation C.4 gives

$$B_z(x, y) = \frac{\mu_0}{4\pi} \int K(x - x', y - y') F(x', y') dx' dy' \quad \text{C.5}$$

where \mathbf{m}_0 is the permittivity of free space and the kernel $K(x, y)$ is given by

$$K(x, y) = \frac{2z^2 - x^2 - y^2}{(x^2 + y^2 + z^2)^{5/2}} \quad \text{C.6}$$

The z dependence of $K(x, y)$ has been suppressed. For thin film geometry, the finite thickness of the sample has been neglected. Numerical examples have shown that it is not necessary to take the finite thickness of the sample into account for the vast majority of thin samples encountered, and doing so unnecessarily complicates the reconstruction procedure.

In order to determine the current flow, Equation C.5 must be solved for $F(x, y)$. Equation C.5 is a First Kind integral equation, and it is resolved using the method of regularization. Regularization replaces the problem of inverting Equation C.5 with the problem of minimizing the functional

$$C(F, \mathbf{a}) = \left\| \frac{\mathbf{m}_0}{4\mathbf{p}} \int F(x', y') K(x - x', y - y') dx' dy' - B_z(x, y) \right\|_2^2 + \mathbf{a} \Omega[F] \quad \text{C.7}$$

with respect to F . The operator Ω is a user-defined measure of the smoothness of F , and \mathbf{a} is the *regularization parameter* that controls the trade-off between smoothness and the degree to which Equation C.5 is satisfied. If Ω is given by

$$\Omega[F] = \left\| \frac{\partial^2 F}{\partial x^2} + \frac{\partial^2 F}{\partial y^2} \right\|_2^2 \quad \text{C.8}$$

then the minimizer of Equation C.7, F_a , is given by [70]

$$F_a(x, y) = \frac{4\mathbf{p}}{\mathbf{m}_0} \iint_{-\infty-\infty}^{\infty\infty} \frac{|\hat{K}(u, v)|^2}{|\hat{K}(u, v)|^2 + \mathbf{a}(2\mathbf{p})^4(u^2 + v^2)^2} \left(\frac{\hat{B}_z(u, v)}{\hat{K}(u, v)} \right) e^{i2\mathbf{p}(ux+vy)} dudv \quad \text{C.9}$$

The problem of minimizing $C(F, \mathbf{a})$ with respect to F has been reduced to a simple Fourier transform with a filter function. However, the filter in Equation C.9 can be directly related back to the imposed smoothness condition on F .

Before Equation C.9 can be used, it is necessary to choose a value for \mathbf{a} . Too large value of \mathbf{a} will place a large emphasis on $\Omega[F]$ and will result in F_a being quite smooth, with an unnecessary loss of detail. Too small value of \mathbf{a} will result in the norm

$$\left\| \frac{\mathbf{m}_0}{4\mathbf{p}} \int KF_a - B_z \right\|_2^2$$

being small, but the regularized solution F_a may deviate considerably

from the true solution. In other words, the norm $\|F_a - F\|_2^2$ (where F is the exact solution)

may be quite large. It needs to be emphasized that a small value for $\left\| \frac{\mathbf{m}_0}{4\mathbf{p}} \int KF_a - B_z \right\|_2^2$

does not necessarily mean that F_a will be close to the true solution since the data B_z is

inexact. The “best” choice for \mathbf{a} is one that minimizes the difference between F_a and

the true solution as measured in some way. Whaba [71] and Davies [70] both present methods of determining \mathbf{a} that attempt to minimize the norm $\|F_{\mathbf{a}} - F\|_2^2$.

Once the function $F_{\mathbf{a}}$ has been found, Equation C.3 needs to be applied to determine J_x and J_y . Since B_z is noisy $F_{\mathbf{a}}$ will contain noise, and differentiating a noisy function is a First Kind problem in and of itself. The required differentiation can also be carried out by the means of Savitsky-Golay smoothing coefficients [72]. These coefficients provide a very computationally efficient means of fitting M data points to an N degree polynomial ($N \leq M$), and returning the value of the derivative found by differentiating the polynomial. Equation C.3 thus represents the resolved current distribution.

References

- [1] J.G. Bednorz and K.A. Müller, *Z. Phys. B* **64**, 189 (1986)
- [2] M.K. Wu, J.R. Asburn, C.J. Torng, P.H. Hor, R.L. Meng, L.Gao, Z.J. Huang, Y.Q. Wang, and C.W. Chu, *Phys. Rev. Lett.* **58**, 908 (1987)
- [3] M. Maeda, Y. Tanaka, M. Fukutomi, and T. Asano, *Jpn. J. Appl. Phys.* **27**, L209 (1988)
- [4] N Kelley, C. Wakefield, M Nassi, P. Corsaro, P. Ladié, S. Spreafico, D.W. Von Dollen, J. Jipping, and L. Masur, *IEEE Trans. on Appl. Supercon.* **11**, 2461 (2001)
- [5] G.A. Daniels and D.C. Larbalestier, unpublished work.
- [6] D. T. Verebelyi, D. K. Christen, R. Feenstra, C. Cantoni, A. Goyal, D. F. Lee, M. Paranthaman, P. N. Arendt, R. F. DePaula, J. R. Groves and C. Prouteau, *Appl. Phys. Lett.* **76**, 1755 (2000)
- [7] G. Villard, F. Legendre, S. Poissonnet, P. Régnier, C. Bifulco and G. Giunchi, *Physica C* **341**, 2007 (2000)
- [8] H. Miao, H. Kitaguchi, H. Kumakura, K. Togano, T. Hasegawa and T. Koizumi, *Physica C* **303**, 81 (1998)
- [9] A.K. Pradhan, S.B. Roy, P. Chaddah, C. Chen, and B.M. Wanklyn, *Phys. Rev. B* **49**, 12 984 (1994)
- [10] L. A. Schwartzkopf, J. Jiang, X. Y. Cai, D. Apodaca, and D. C. Larbalestier, *Appl. Phys. Lett.* **75**, 3168 (1999)
- [11] D.M. Feldmann and D.C. Larbalestier, unpublished work.
- [12] S.H. Yun and J.Z. Wu, *Appl. Phys. Lett.* **68**, 862 (1996)
- [13] K. Fujinami, H. Suematsu, M. Karppinen and H. Yamauchi, *Physica C* **307**, 202 (1998)
- [14] S. L. Yan, Y. Y. Xie, J. Z. Wu, T. Aytug, A. A. Gapud, B. W. Kang, L. Fang, M. He, S. C. Tidrow, K. W. Kirchner, S. C. Tidrow and K. W. Kirchner, *Appl. Phys. Lett.* **30**, 2989 (1998)

- [15] T. Akao, S.R. Lee, K. Mizogami, H. Suematsu and H. Yamauchi, *Physica C* **338**, 76 (2000)
- [16] Y. Yu, H.M. Shao, Z.Y. Zheng, A.M. Sun, M.J. Qin, X.N. Xu, S.Y. Ding, X. Jin, X.X. Yao, J. Zhou, Z.M. Ji, S.Z. Yang and W.L. Zhang, *Physica C* **289**, 199 (1997)
- [17] Y.Y. Xie, T. Aytug, J.Z. Wu, D.T. Verebelyi, M. Paranthaman, A. Goyal, and D.K. Christen, *Appl. Phys. Lett.* **77**, 4193 (2000)
- [18] A.H. Cardona, H. Suzuki, T. Yamashita, K.H. Young and L.C. Bourne, *Appl. Phys. Lett.* **62**, 411 (1993)
- [19] J. Y. Juang, J. H. Horng, S. P. Chen, C. M. Fu, K. H. Wu, T. M. Uen, and Y. S. Gou, *Appl. Phys. Lett.* **66**, 885 (1995)
- [20] A.A. Gapud, J.Z. Wu, L. Fang, S.L. Yan, Y.Y. Xie, M.P. Siegel and D.L. Overmyer, *APL* **74**, 3878 (1999)
- [21] D. Dimos, P. Chaudhari and J. Mannhart, *Phys. Rev. B* **41**, 4038 (1990); D. Dimos, P. Chaudhari, J. Mannhart and F.K. LeGoues, *Phys. Rev. Lett.* **61**, 219 (1998)
- [22] N.F. Heinig, R.D. Redwing, J.E. Nordman and D.C. Larbalestier, *Phys. Rev. B* **60**, 1409 (1999)
- [23] T. Nabatame, S. Koike, O.B. Hyun, I. Hirabayashi, H. Suhara and K. Nakamura, *Appl. Phys. Lett.* **65**, 776 (1994)
- [24] H. Suhara, T. Nabatame, Ok-Bae Hyun, S. Koike, I. Hirabayashi, *Supercond. Sci. Technol.* **8**, 443 (1995)
- [25] D.M. Feldmann and D.C. Larbalestier, unpublished work. Magneto-optical imaging of $\text{HgBa}_2\text{CaCu}_2\text{O}_x$, $\text{Tl}_2\text{Ba}_2\text{CaCu}_2\text{O}_x$ and $\text{YBa}_2\text{Cu}_3\text{O}_7$ thin films grown on polycrystalline substrates (RABiTS™) have all shown similar electro-magnetic granularity.
- [26] Y. Iijima, N Tanabe, Y. Ikeno and O. Kohno, *Physica C* **185**, 1959 (1991)
- [27] X.D. Wu, S.R. Foltyn, P.N. Arendt, W.R. Blumenthal, I.H. Campbell, J.D. Cotton, J.Y. Coulter, W.L. Hults, M.P. Maley, H.F. Safar and J.L. Smith, *Appl. Phys. Lett.* **67**, 2397 (1995)

- [28] A. Goyal, D.P. Norton, J.D. Budai, M. Paranthaman, E.D. Specht, D.M. Kroeger, D.K. Christen, Q. He, B. Saffian, F.A. List, D.F. Lee, P.M. Martin, C.E. Klabunde, B. Hatfield, and V.K. Sikka, *Appl. Phys. Lett.* **69**, 1795 (1996).
- [29] J.R. Groves, P.N. Arendt, S.R. Foltyn, Q. Jia, T.G. Holesinger, H. Kung, R.F. DePaula, P.C. Dowden, E.J. Peterson, L. Stan and L.A. Emmert, *Proc. of The 2001 International Workshop on Superconductivity* (2001)
- [30] J.R. Groves, P.N. Arendt, H. Kung, S.R. Foltyn, R.F. DePaula, L.A. Emmert, and J.G. Storer, *IEEE Trans. Appl. Supercond.* **11**, 2822 (2001)
- [31] J. Wiesmann, J. Dzick, J. Hoffmannm K. Keinemann and H.C. Freyhardt, *J. Mater. Res.* **13**, 3149 (1998)
- [32] N.A. Rutter and B.A. Glowacki, *IEEE Trans. Appl. Supercond.* **11**, 2730 (2001)
- [33] M. Paranthaman, S. Sathyamurthy, T. Aytug, D.B. Beach, A. Goyal, B.W. Kang, R. Feentra, D.K. Christen, D.F. Lee, P.M. Martin, L. Heatherly Jr., and D.M. Kroeger, *Proc. 2001 International Workshop on Superconductivity, Hawaii* (2001)
- [34] A. Goyal, E.D. Specht, D.M. Kroeger, R. Feenstra, D. Norton, M. Paranthaman, D.F. Lee, and D.K. Christen, *Micron* **30**, 463 (1999)
- [35] J.M. Phillips, K. Kugimiya, S. Tanaka, and Y. Shiohara, *J. Mater. Res.* **12**, 2823 (1997)
- [36] M. Paranthaman, R. Feentra, D.F. Lee, D.B. Beash, J.S.Morrell, T.G. Chirayil, A. Goyal, X. Cui, D.T. Verebelyi, J.E. Mathis, P.M. Martin, D.P. Norton, E.D. Specht, D.K. Christen and D.M. Kroeger, *Adv. Cryog. Eng.* (in press).
- [37] D.M. Feldmann, J.L. Reeves, A.A. Polyanskii, G. Kozlowski, R.R. Biggers, R.M. Nekkanti, I. Maartense, M. Tomsic, P. Barnes, C.E. Oberly, T.L. Peterson, S.E. Babcock, and D.C. Larbalestier, *Appl. Phys. Lett.* **77**, 2906 (2000)
- [38] R. Feenstra, T.B. Lindemer, J.D. Budai, and M.D. Galloway, *J. Appl. Phys. Lett.* **69**, 6569 (1991)
- [39] A. Gupta, R. Jagannathan, E.I. Cooper, E.A. Giess, J.L. Landman and B.W. Hussey, *Appl. Phys. Lett.* **52**, 2077 (1988)
- [40] A. Gurevich and E.A. Pashitski, *Phys. Rev. B* **57**, 13878 (1998)
- [41] J. Mannhart and H. Hilgenkamp, *Appl. Phys. Lett.* **73**, 265 (1998)

- [42] A. Ichinose, C.Y. Yang, D.C. Larbalestier, S.E. Babcock, A. Kikuchi, K. Tachikawa, and S. Akita, *Physica C* **324**, 113 (1999)
- [43] A.A. Polyanskii, A. Gurevich, A.E Pashitski, N.F. Heinig, R.D. Redwing, J.E. Nordman, and D.C. Larbalestier, *Phys. Rev. B* **53**, 8687 (1996)
- [44] R. Feenstra, private communication.
- [45] J. Reeves, Ph.D. Thesis, University of Wisconsin – Madison (2001)
- [46] E.H. Brandt and M. Indenbom, *Phys. Rev. B* **48**, 12893 (1993)
- [47] E. Zeldov, J.R. Clem, M. McElfresh, and M. Darwin, *Phys. Rev. B* **49**, 9802 (1994)
- [48] H. Kung, S.R. Foltyn, P.N. Arendt, J.R. Groves, T.G. Holesinger, Q.X. Jia, and M.P. Maley, *Proc. of the 2001 International Workshop of Superconductivity, Hawaii* (2001)
- [49] A.E. Pashitski, A. Gurevich, A.A. Polyanskii, D.C. Larbalestier, A. Goyal, E.D. Specht, D.M. Kroeger, J.A. DeLuca, and J.E. Tkaczyk, *Science* **275**, 367 (1997)
- [50] X.Y. Cai, A. Gurevich, I.F. Tsu, D.L. Kaiser, S.E. Babcock, and D.C. Larbalestier, *Phys. Rev. B* **57**, 10951 (1998)
- [51] D. Verebelyi, C. Prouteau, R. Feenstra, and D. Christen, *IEEE Trans. Appl. Supercond.* **9**, 2655 (1999)
- [52] A. Diaz, L. Mechin, P. Berghuis, and J.E. Evetts, *Phys. Rev. Lett.* **80**, 3855 (1998)
- [53] B. Dam, J.M. Huijbregtse, F.C. Klaassen, R.C.F. van der Geest, G. Doornbos, J.H. Rector, A.M. Testa, S. Freisem, J.C. Martinez, B. Stauble-Pumpin, and R. Griessen, *Nature (London)* **399**, 439 (1999)
- [54] S.R. Foltyn, Q.X. Jia, P.N. Arendt, L. Kinder, Y. Fan, and J.F. Smith, *Appl. Phys. Lett.* **75**, 3692 (1999)
- [55] R. Feenstra, A. Goyal, M. Paranthaman, D.F. Lee, P.M. Martin, D.K. Chrsiten, and D.M. Kroeger, *Proc. of the 2001 International Workshop on Superconductivity, Hawaii* (2001)
- [56] G. Hammerl, A. Schmehl, RR. Schulz, B. Goetz, H. Bielefeldt, C.W. Schneider, H. Hilgenkamp, and J. Mannhart, *Nature (London)* **407**, 162 (2000)
- [57] G.A. Daniels, A. Gurevich, and D.C. Larbalestier, *Appl. Phys. Lett.* **77**, 3251 (2000)

- [58] D.T. Verebelyi, C. Cantoni, J.D. Budai, D.K. Christen, H.J. Kim and J.R. Thompson, *Appl. Phys. Lett.* **78**, 2031 (2001)
- [59] P.B. Alers, *Phys. Rev. B* **105**, 104 (1957)
- [60] R.M. Grechishkin, M. Yu Goosev, S.E. Ilyashenko and N.S. Neustroev, *J. Magn. Magn. Mater.* **157/158**, 305 (1996)
- [61] A.A. Polyanskii, D.M. Feldmann, and D.C. Larbalestier, "Magneto-Optical Characterization Techniques," submitted to D. Cardwell and D. Ginley, editors, "Handbook of Superconducting Materials," Institute of Physics Publishing, to be published.
- [62] V. Randle and O. Engler, *Introduction to Texture Analysis: Macrotecture, Microtexture, and Orientation Mapping*, Gordon and Breach Science Publishers, 2000
- [63] V. Randle, *The Measurement of Grain Boundary Geometry*, Electron Microscopy in Materials Science Series, Institute of Physics Publishing, 1993
- [64] D.J. dingley, K.Z. Baba-Kishi, and V. Randle, *Atlas of Backscattering Kikuchi Diffraction Patterns*, Microscopy in Materials Science Series, Institute of Physics Publishing, 1995
- [65] J.D. Jackson, *Classical Electrodynamics*, John Wiley & Sons, 1975.
- [66] R.G. Hohlfeld, J.I.F. King, T.W. Drueding and G.V.H. Sandri, *SIAM J. Appl. Math.* **53**, 154 (1993)
- [67] E. Micheli, N. Magnoli, G.A. Viano, *SIAM J. Math. Anal.* **29**, 855 (1998)
- [68] A.N. Tikhonov and V.Y. Arsenin, *Solutions of ill-posed problems*, V.H. Winston and Sons, 1977
- [69] G.M. Wing, *A Primer on Integral Equations of the First Kind*, Society for Industrial and Applied Mathematics, 1991
- [70] A.R. Davies, *Treatment of Integral Equations by Numerical Methods*, p.95, Edited by C.T.H. Baker and G.F. Miller, Academic Press, Inc.
- [71] G. Whaba, *SIAM J. Numer. Anal.* **14**, 651 (1977)
- [72] W.H. Press, S.A. Teukolsky, W.T. Vetterling, and B.P. Flannery, *Numerical Recipes in Fortran 77 Second Edition*, Cambridge University Press, 1992